Artificial Intelligence-Based Optimization of Structural Parameters to Simulate the Seismic Behavior of Buildings

（人工知能を用いた構造パラメータの最適化による建築構造物の地震時挙動シミュレーション）

July 2022

Doctor of Philosophy (Engineering)

Mekaoui Nabil

メカオウィ ナビル

Toyohashi University of Technology

DEDICATION

To my defunct Father who used to encourage me to pursue a PhD,

To my Mother for her unconditional love and support,

And to my Brothers Amine, Rida, Adam, and their nuclear families.

ACKNOWLEDGEMENTS

A PhD is a long journey beyond the limit of existing science. A journey to the unknown that requires not only personal skills, but also technical, financial, and emotional supports. I would like herein to acknowledge and to express my deepest gratitude to all those who contributed to the success of this research work in a very short time of three years. My supervisor, Prof. Dr. Saito Taiki, has undoubtedly the major contribution by believing first in my profile and for all his guidance and assistance on and off campus. The administrative staff of Toyohashi University of Technology (TUT) were always helpful and cooperative with my requests and could maintain a good working environment even during the challenging time of COVID-19 pandemic. My thanks go also to the Ministry of Education, Culture, Sports, Science and Technology of Japan, for providing me the MEXT Scholarship to pursue my PhD without any financial issues.

In my home country Morocco, I would like to thank the President of Mohammed V University of Rabat, Prof. Dr. Mohammed Rhachi, for granting me a long leave of absence to pursue my PhD in Japan, and Prof. Dr. Nouzha Lamdouar, the head of the Civil Engineering Department of the Mohammadia School of Engineers, for her limitless efforts to promote higher education and scientific research. A special gratitude goes to the defunct Prof. Dr. Mohamed Taoufik El Ouali, who first initiated me to the research field of Earthquake Engineering.

Finally, I am very grateful to specific students and former students of the TUT Department of Architecture and Civil Engineering, who contributed directly and/or indirectly to the buildup of this dissertation: Kawamura Miku, Miyachi Yuichi, Takahashi Shuhei, Horioka Tomoki, and Hada Shuhei. Thank you all for your help and kindness.

ABSTRACT

An Artificial Intelligence-based optimization of structural parameters is elaborated in this dissertation to perform a hybrid seismic analysis of building structures. This original problem-solving approach consists of combining advantageous of both Artificial Intelligence and conventional nonlinear time history analysis (NTHA), to increase further the accuracy of seismic response simulation. Two optimization domains are investigated: the first one targets specific physical parameters of the building model; the second one proposes new machine learning models simulating specific structural component or group of components, as surrogates to their analytical counterparts. Both optimization outputs are then deployed in hybrid seismic analyses of several building models to check their respective efficiencies in improving the accuracy of the seismic response simulation. To this end, synthetic, experimental, and field data are used as references.

In evaluation of seismic safety of buildings, system parameter identification is crucial. Although many mathematical models exist to evaluate the physical properties of building structures, the tremendous number of involved parameters maintains a certain degree of uncertainty. In this research, a system parameter optimization procedure is developed using Response Surface Method and Bayesian Optimization Technique. The developed program was successfully tested on real buildings in the Aichi prefecture at eastern Japan, with a view to incorporate it in the existing online seismic diagnosis system. The accuracy and the promptness of the optimization procedure make it efficient for a real-time system identification.

Simulating the structural behavior of typical seismic isolators under a wide spectrum of realistic loading conditions is still not accurately achieved by a single analytical model. Deep learning networks predicting the non-linear hysteretic behavior of specific triple pendulum bearing (TPB), lead rubber bearing (LRB), and a full seismic isolation layer, are developed, tested, and eventually deployed in the proposed hybrid seismic analysis. Experimental datasets were derived from a shake-table test program of an isolated five-story building specimen, performed at the Hyogo Engineering Research Center (E-Defense) of Miki, Japan. Data measured during 34 different table motions are processed to construct a TPB/LRB dataset of 158/55 samples. Conventional NTHAs were performed to generate synthetic data for the case study of full isolation layer. Comparisons with reference experimental/synthetic data showed that the proposed hybrid analysis could simulate accurately the seismic response of studied buildings. The generalization capability of developed surrogate machine learning models on the substantial datasets used in this study, revealed the benefit of applying machine learning to solve complex structural engineering problems.

TABLE OF CONTENTS

LIST OF TABLES

LIST OF FIGURES

LIST OF ABREVIATIONS

AI	Artificial Intelligence
ANN	Artificial Neural Network
BOT	Bayesian Optimization Technique
CLB	Cross Linear Bearing
CNN	Convolutional Neural Network
DIA	Diablo synthetic ground motion
DL	Deep Learning
E-Defense	The Hyogo Engineering Research Center of Miki, Japan
ELC	1940 Imperial Valley El Centro ground motion
FEM	Finite Element Method
GM	Ground motion
GP	Gaussian Process
GRU	Gated Recurrent Unit
IWA	2011 Tohoku Iwanuma ground motion
KJM	1995 Kobe JMA ground motion
LAN	Local Area Network
LGP	1989 Loma Prieta Los Gatos ground motion
LMM	Lumped Mass Model
LRB	Lead Rubber Bearing
LSTM	Long Short-Term Memory
MB	Model Building
MDOF	Multi Degree Of Freedom
ML	Machine Learning
MLM	Machine Learning Model
MLP	MultiLayer Perceptron
NRB	Natural Rubber Bearing
NTHA	Non-linear Time History Analysis
OpS	Operator Splitting
PGA	Peak Ground Acceleration
PTA	Peak Table Acceleration
RC	Reinforced Concrete
RNN	Recurrent Neural Network
RPP	Response Prediction Problem
RRS	1994 Northridge Rinaldi ground motion
RSM	Response Surface Method
SCT	1985 Mexico City SCT ground motion
SHM	Structural Health Monitoring
SRC	Steel Reinforced Concrete
STERA-3D	STructural Earthquake Response Analysis-3 Dimensional
SYL	1994 Northridge Sylmar ground motion
TAB	1978 Tabas ground motion
TAK	1995 Kobe Takatori ground motion
TCH-EB	Toyohashi City Hall-East Building
TCH-WB	Toyohashi City Hall-West Building
TCU	1999 Chichi TCU065 ground motion
TFSB	Toyohashi Fire Station Building
TPB	Triple Pendulum Bearing
TUT	Toyohashi University of Technology
VOG	Vogtle synthetic ground motion
WSW80	1987 Superstition Hills Westermorland ground motion

CHAPTER 1: INTRODUCTION

1.1. Background and problem statement

While the behavior of most conventional building structural components is well understood by physics, constitutive laws of nonconventional ones may still be not fully understood. This includes cases of new materials, new devices, unusual geometries, and all other circumstances where many assumptions and/or calibrations are necessary to validate non-generalized analytical models. Discrepancies between simulated and actual seismic responses of building structures with such components may be large and lead to over/underestimate the design, as highlighted recently for some cases of seismically isolated buildings [1]. Furthermore, some secondary structural elements (repartition/infill walls, false ceiling…), construction imperfections, aging of materials, and/or posterior structural damage…; may be disregarded in the structural model because of the inability to model them. Aforementioned anomalies are shortcomings of the conventional seismic analysis of building structures.

Artificial intelligence (AI) is all algorithms aiming to train machines to perform repetitive and/or difficult tasks that may induce some errors if handled by humans. It was initiated in the 1950's and has currently many subsets (Fig. 1) such as natural language processing (NLP), speech recognition, robotics, machine vision, and machine learning (ML).

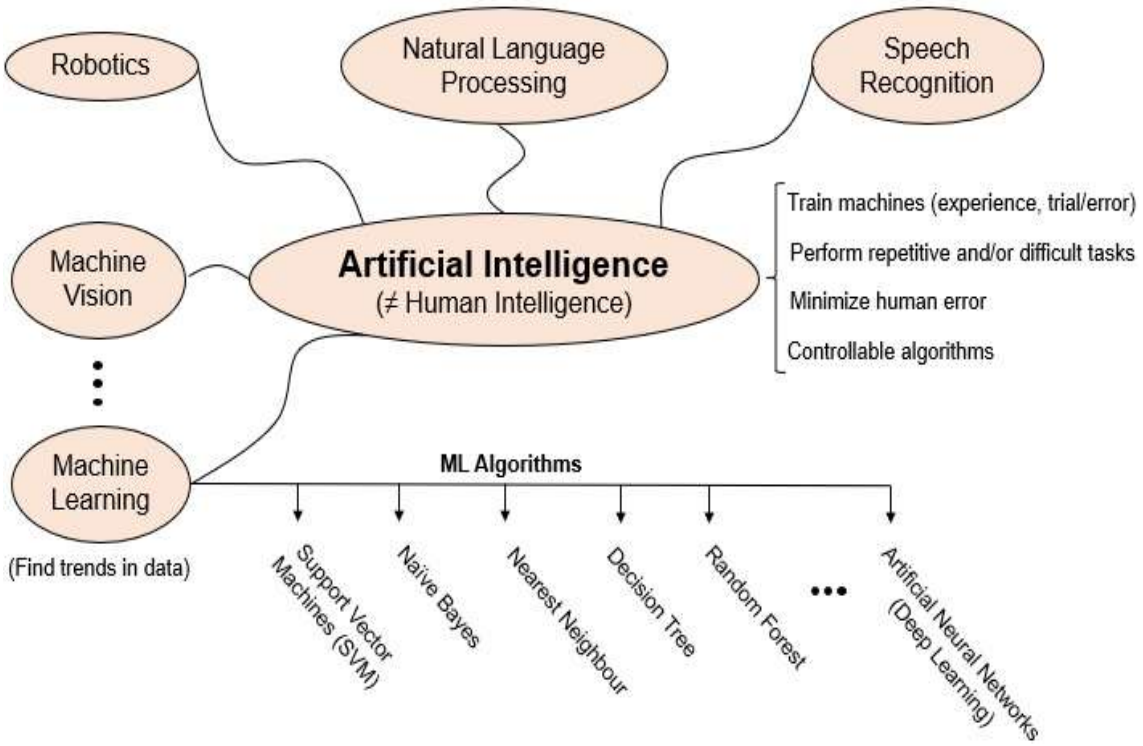

Figure 1: Overview of Artificial Intelligence branches.

The application of AI and ML in structural and earthquake engineering is flourishing within the research community in the past two decades [2, 3]. The availability of structural data, the continuous advances in computational resources and ML algorithms, and the complexity/difficulty of some engineering problems have contributed to its implementation in several fields such as structural response prediction [4, 5], system identification [6, 7], and damage assessment [8, 9]. While few applications aim to optimize specific structural parameters, most of the others tend to predict the damage state or the structural response of the building as a whole. These applications are therefore limited to the type of structures used during the training process, and disregard all well-established analytical models based on the laws of Physics. Reason why AI applications are still regarded as a "black box" by many researchers and practitioners.

As a consequence, worldwide seismic codes and current commercial structural softwares have not yet included any provisions regarding the use of data-driven methods in structural design; thus, limiting the application of AI in the structural engineering practice. Physics-based methods remain legitimately the most reliable and common approach for seismic design of structures. However, both Physics-based and data-driven approaches have their respective pros and cons. Physics is more reliable, but it has its limits. AI can solve very complex and difficult problems, but its "black box" image makes it untrustworthy. Is it better to stick to conventional analysis and limit our problem-solving capability, or use AI to go beyond the limits of the current Physics-based knowledge and provide solutions to more complex problems ?

1.2. Objective of the study and thesis outline

This study aims to tackle aforementioned limitations of conventional seismic analysis and AI applications in building response prediction problems, by combining simultaneously advantageous of both Physics-based and data-driven procedures. Both approaches are considered as complementary rather than dissociated. Physics is legitimately taken as a reference, and its limitations are surpassed by using AI algorithms. This original problem-solving approach is elaborated in this study to check its applicability and efficiency in the open research area of simulating the seismic time-history response of building structures. Such a hybrid approach would lead to more accurate analyses; thus, contributing to an efficient evaluation and/or mitigation of earthquake damage.

This dissertation consists of three main parts: i) AI-based optimization of structural parameters of existing buildings using field data, ii) design of ML models (MLMs) of some structural components as surrogates to their analytical counterpart, and iii) the incorporation of

elaborated MLMs into the proposed hybrid seismic analysis for a numerical and experimental validations.

Chapter II evaluates the performance of two optimization algorithms in tuning story stiffness parameters of pre-defined lumped mass models (LMMs) of three existing buildings in Aichi prefecture in Japan. This optimization aims to increase the reliability of the real-time seismic diagnostic system of target essential buildings. Response surface method (RSM) and Bayesian optimization technique (BOT) are investigated, and their respective efficiencies are analyzed and compared in term of accuracy and computation time. To this end, recorded acceleration data during the Osaka Earthquake of 18th June 2018, are used as a reference. The favorite optimization technique is selected for subsequent implementation in the internet cloud.

Chapter III elaborates and applies a comprehensive framework to design MLMs capable of predicting the structural behavior of target component or group of components. Seismic isolation devices are selected as case studies and recurrent neural networks (RNNs) are developed to simulate their complex hysteretic behavior. Synthetic data generated by nonlinear time history analyses (NTHAs) and experimental data of a well-designed test program, are processed, and deployed to train and test the surrogate MLMs. Their efficiency is evaluated in terms of accuracy, uncertainty, and elaboration time.

Chapter IV introduces and evaluates the original hybrid seismic analysis developed in this study, taking advantages of both analytical models and MLMs. Python scripts are elaborated to incorporate designed MLMs into the time integration method to perform hybrid analyses of many isolated buildings subjected to a wide spectrum of earthquake ground motions. The isolation layer response and the peak story displacements/accelerations are computed and compared with reference values of conventional analyses or experimental records. The capability of the hybrid analysis to outperform the conventional one is discussed based on the studied cases.

Chapter V recapitulates the major findings of this study and summarizes the conclusions. Limitations of the proposed hybrid approach are discussed, and further improvements and related studies are proposed for future research works.

Appendices presented at the end of this dissertation provide developed Python scripts for both conventional and hybrid seismic analyses of LMMs, followed by 34 graphs of two-dimensional force-displacement hystereses of specific isolation layers of the experimental test program performed at E-Defense in August 2011.

CHAPTER 2: LMM UPDATING USING LIMITED SENSORS DATA

2.1. Introduction

In the event of a major earthquake, one of the key issues for emergency management officials is to know whether or not the vital facilities, those that provide emergency assistance such as hospitals and fire stations and government buildings, are safe enough for a continuous and secure use immediately after a seismic event. To support emergency actions of Aichi prefecture in Japan , a real-time seismic diagnostic system has been established at TUT to provide designated officials with necessary safety information about target building structures [10, 11]. Fig. 2 summarizes the flowchart of this seismic diagnostic system. The acceleration data recorded during a seismic event at specific floors of the designated buildings, is uploaded in the internet cloud and processed immediately in predefined analysis models using the software STERA-3D [12]. The first seismic evaluation is carried out by analyzing the response of the building lumped mass model (LMM), whose properties are deducted beforehand from a non-linear push-over analysis of a frame model established based on structural drawings. The safety of the building is determined based on the response values and results of this first seismic evaluation is reported by email to designated officials withing few minutes. If the response of the first seismic evaluation exceeds the predefined threshold of structural and non-structural damage, the second stage seismic evaluation is performed using the frame model to estimate the amount of damage at the component level. The report of the second seismic analysis is sent by email within few hours. Similar remote structural health monitoring (SHM) has already been deployed in earthquake prone countries such as the United States [13], and Japan [14]. However, the seismic diagnosis procedures may differ based on system identification techniques, wavelet analyses, fragility curves and many others.

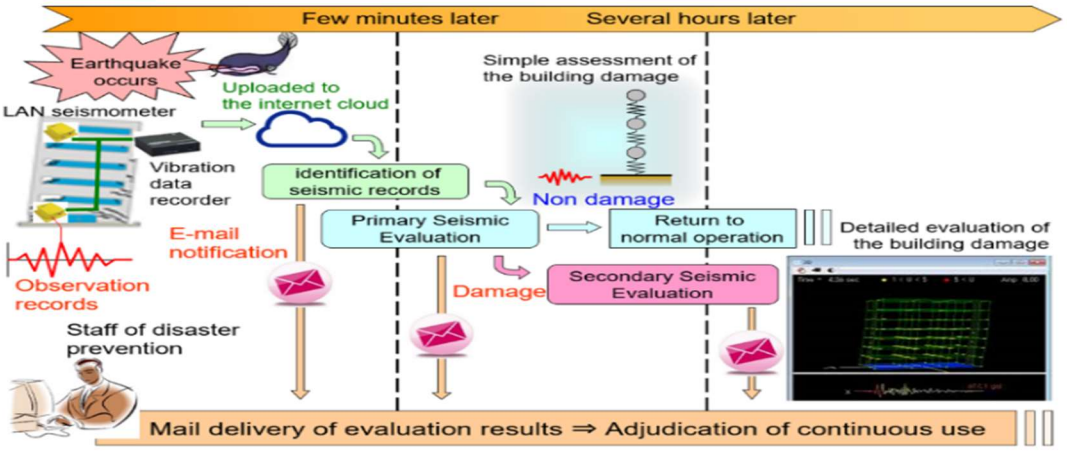

Figure 2: Flowchart of the real-time seismic diagnostic system of Aichi prefecture.

The accuracy of simulated response is affected by many sources of uncertainties (non-structural elements, evolution of material properties with time, soil-structure interaction…) which are extremely difficult to evaluate for integration into an analysis model; therefore, simulated acceleration response may differ significantly from observed acceleration records. To overcome this shortcoming, the identification of building physical parameters (mass, stiffness, and damping) is commonly used for model updating in SHM [15, 16]. To update the LMM for more accurate first stage seismic evaluation, this Chapter presents the procedure developed to optimize target structural parameters based only on two acceleration records at the level of the basement and an upper floor of the building. Two optimization procedures, the response surface method (RSM) and the Bayesian optimization techniques (BOT), are investigated and their respective performances are evaluated and compared through the analysis of target existing buildings subjected to real earthquake ground shaking events. The scope of this Chapter is to perform a quick and efficient optimization of system physical parameters using very limited number of available acceleration records.

2.2.Target building and earthquake events

Three buildings existing in Toyohashi City of Aichi prefecture in Japan, are considered in this study. The Toyohashi City Hall East Building (TCH-EB), the Toyohashi City Hall West building (TCH-WB), and the Toyohashi Fire Station Building (TFSB). Each of them is instrumented with two LAN seismometers: one at the basement level and the second at an upper story level. The acceleration waves recorded during the Osaka earthquake of June 18th, 2018 [17], are used in this study. The three buildings behaved mainly within the elastic range since recorded motions were of low intensity. A fourth Model Building (MB) has been considered to perform the optimization process in case of non-linear behavior. It is a fictive four-story LMM subjected to the N-S component of El Centro Earthquake of May 18th, 1940. The simulated acceleration wave at the 3rd floor is considered as the target acceleration wave. Table 1 recapitulates aforementioned information about all studied cases :

Table 1: Summary of studied buildings.

Designation	Nature	No. of stories	Lower sensor level	Upper sensor level
TCH-EB	Existing SRC buildings	15	1st basement (record of 18.06.18)	12th floor (record of 18.06.18)
TCH-WB		10	1st basement (record of 18.06.18)	7th floor (record of 18.06.18)
TFSB		7	1st basement (record of 18.06.18)	6th floor (record of 18.06.18)
MB	Model steel building	4	Ground floor (El Centro1940 NS)	3rd floor (simulated)

2.3.Target structural parameters

The frame models of studied buildings are made from the structural drawings provided by building officials. Non-linear pushover analyses are performed by STERA-3D to compute the capacity curve of each story in order to generate the equivalent LMM which has a tri-linear hysteresis model for story drift and shear force relationship. The damping matrix *[C]* is considered proportional to the initial stiffness matrix *[K]*, and thus assumed to be invariant during an analysis. Fig. 3 shows an example of a converted n-story building structure to its LMM having three main parameters at each level: the story mass *m*, the initial story stiffness *k*, and the story damping factor *c*. Complementary parameters are omitted in this figure for a simplified view. The LMM is considered fixed-base with no soil-structure interaction. The stars represent the positions of a typical installation of LAN seismometers; one at the lowest floor level and the second at an upper level (*n-1* floor in the figure).

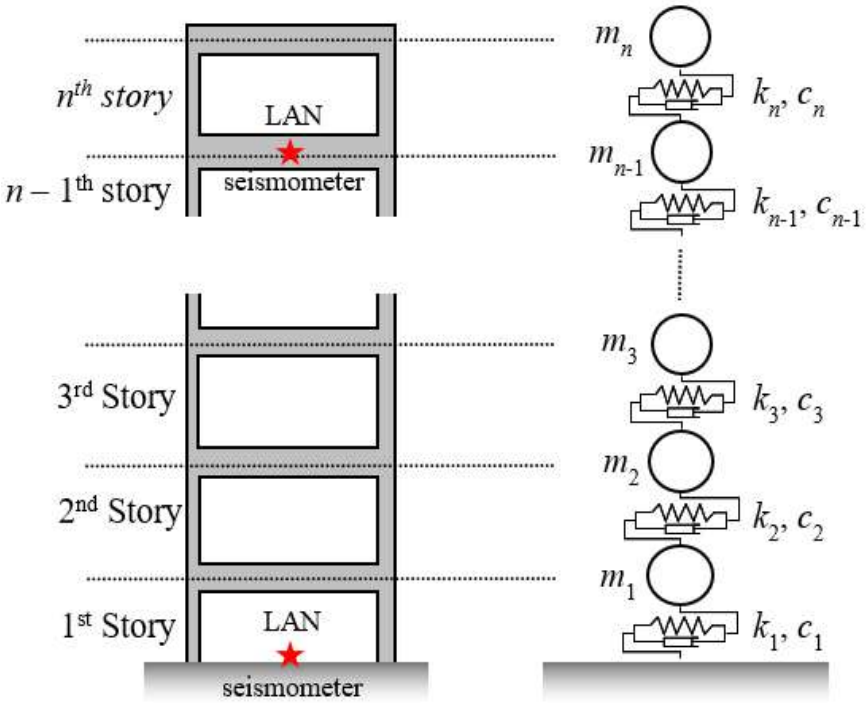

Figure 3: Lumped mass model of a n-story building.

Using the parameters of the L.M.M. and the recorded input acceleration at each building basement, the time history acceleration response at the target level can be computed and compared with the target (recorded or simulated) acceleration wave at the same level. Thus, we define the objective function as the acceleration error given by Eq. (1):

$$error = \frac{\sqrt{\sum_{data}\left(Acceleration_{target} - Acceleration_{simulated}\right)^2}}{Number\ of\ data} \quad (1)$$

The optimization problem consists of determining an optimal combination of the varying parameters that minimizes the objective function. The acceleration error is computed at only one level, therefore the uniqueness of the optimal combination of the LMM parameters may be compromised. Two optimization procedures are considered in this Chapter: the RSM as a traditional method, and the BOT as a newly developed technique examined in this study for its effectiveness.

System parameters with high uncertainty are selected, then their variation ranges are defined as a percentage of their corresponding LMM values. For the existing buildings (TCH-EB, TCH-WB, and TFSB), initial story stiffnesses of all stories are selected as the parameters to be optimized. Floors masses and the damping ratios are assumed to be fixed values. The optimization of damping is targeted in further studies. For the nonlinear model (MB), the story yield strength is also selected for optimization. Table 2 shows the nature of selected parameters and their initial variation range.

Table 2: Nature and variation range of selected parameters for optimization.

Designation	**Seismic behavior**	**Parameters to optimize**		**Variation range (% of initial LMM value)**
		Nature	**Number**	
TCH-EB	Linear	Initial story stiffnesses	15	[0.8, 2.0]
TCH-WB	Linear	Initial story stiffnesses	10	[0.8, 2.0]
TFSB	Linear	Initial story stiffnesses	7	[0.8, 2.0]
MB	Non-linear bilinear model	Initial story stiffnesses	4	[0.8, 2.0]
		Story yield strengths	4	[0.5, 1.5]

2.4.Optimization algorithms

2.4.1. Response surface method

In the response surface method [18, 19, 20], the response quantity Y is expressed as the 2nd order polynomial function of N design variables $R_1, R_2 \ldots, R_N$ where Y is the predicted response, X_i is the standardized variable, L_i is half of the range of the variable and M_i is the midpoint of the range of variable,

$$Y = b_0 + \sum_{i=1}^{N} b_i X_i + \sum_{1 \le i < j}^{N} b_{ij} X_i X_j + \sum_{i=1}^{N} b_{ii} X_i^2 \qquad (2)$$

$$X_i = \frac{R_i - M_i}{L_i} \tag{3}$$

$$L_i = \frac{R_{i,max} - R_{i,min}}{2} \tag{4}$$

$$M_i = \frac{R_{i,max} + R_{i,min}}{2} \tag{5}$$

The Central Composite Design is commonly used to decide the experimental variables. The variables are selected as 1) two levels of each variable, X_i=*-1,1*, 2) two points X_i=*-α,α* on each axis, and 3) the center point. In total *M=2N+2N+1* points. Fig. 4 shows the experimental variables in case of three design variables.

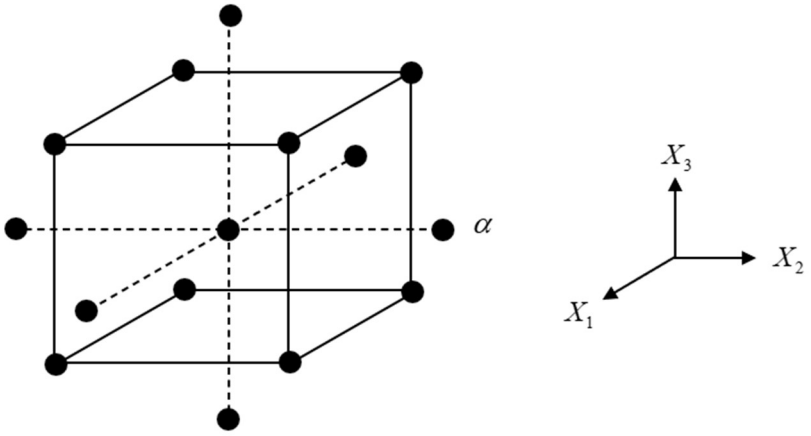

Figure 4: Experimental variables in case of Central Composite Design.

Eq. (2) can be written in a matrix form as,

$$\{Y\} = [X]\{b\} \tag{6}$$

$$\{Y\} = \{Y_1, Y_2, \ldots Y_M\}^T \tag{7}$$

$$[X] = \begin{bmatrix} 1 & {}_1X_1 & \cdots & {}_1X_N & {}_1X_1\,{}_1X_2 & \cdots & {}_1X_{N-1}\,{}_1X_N & {}_1X_1^{\,2} & \cdots & {}_1X_N^{\,2} \\ 1 & {}_2X_1 & \cdots & {}_2X_N & {}_2X_1\,{}_2X_2 & \cdots & {}_2X_{N-1}\,{}_2X_N & {}_2X_1^{\,2} & \cdots & {}_2X_N^{\,2} \\ \vdots & \vdots & \vdots & \vdots & \vdots & \vdots & \vdots & \vdots & \vdots & \vdots \\ 1 & {}_MX_1 & \cdots & {}_MX_N & {}_MX_1\,{}_MX_2 & \cdots & {}_MX_{N-1}\,{}_MX_N & {}_MX_1^{\,2} & \cdots & {}_MX_N^{\,2} \end{bmatrix} \tag{8}$$

$$\{b\} = \{b_0, b_1, \cdots, b_N, b_{1,2}, \cdots, b_{N-1,N}, b_{1,1}, \cdots, b_{N,N}\}^T \tag{9}$$

The parameter vector *{b}* is obtained by,

$$\{b\} = [X]^+\{Y\} \tag{10}$$

Where *[X]+* is the pseudo-inverse matrix of *[X]*.

If *[X]* is a rectangular matrix *(N×m)*, its singular value decomposition is,

$$[X] = [U][\Sigma][V]^T \tag{11}$$

Where, *[U] (N×N)* and *[V] (m×m)* are orthogonal matrices,

$$[U][U]^T = [U]^T[U] = [I] \tag{12}$$

$$[V][V]^T = [V]^T[V] = [I] \tag{13}$$

*[∑]*is a rectangular matrix *(N×m)* with singular values in diagonal elements,

$$[\Sigma] = \begin{bmatrix} \lambda_1 & \cdots & 0 \\ \vdots & \ddots & \vdots \\ 0 & \cdots & \lambda_m \\ \vdots & & \vdots \\ 0 & \cdots & 0 \end{bmatrix} \tag{14}$$

Its pseudo-inverse matrix is obtained as,

$$[X]^+ = [V][\Sigma]^+[U]^T \tag{15}$$

Where, *[∑]+* is a rectangular matrix *(m×N)* as,

$$[\Sigma]^+ = \begin{bmatrix} \frac{1}{\lambda_1} & \cdots & 0 & \cdots & 0 \\ \vdots & \ddots & \vdots & & \vdots \\ 0 & \cdots & \frac{1}{\lambda_m} & \cdots & 0 \end{bmatrix} \tag{16}$$

From the response surface, the variables $X_1, X_2 \ldots, X_N$ to minimize the response surface are obtained by,

$$\frac{\partial Y}{\partial X_i} = b_i + \sum_{1 \le i < j}^{N} b_{ij} X_j + 2\, b_{ii} X_i = 0, \quad i = 1,2,\cdots,N \tag{17}$$

In a matrix form,

$$\begin{Bmatrix} -b_1 \\ -b_2 \\ \vdots \\ -b_{N-1} \\ -b_N \end{Bmatrix} = \begin{bmatrix} 2b_{11} & b_{12} & \cdots & \cdots & b_{1N} \\ & 2b_{22} & \ddots & & b_{2N} \\ & & \ddots & \ddots & \vdots \\ & & & \ddots & b_{N-1,N} \\ sym. & & & & 2b_{NN} \end{bmatrix} \begin{Bmatrix} X_1 \\ X_2 \\ \vdots \\ X_{N-1} \\ X_N \end{Bmatrix}$$

or

$$\{-b\} = [B]\{X\} \tag{18}$$

Therefore, the optimum variables are obtained by using the pseudo-inverse matrix of *[B]*,

$$\{X\} = [B]^{+}\{-b\} \quad (19)$$

Fig. 5 shows the response surface and the optimum variables in case of two variables. In this study, the response quantity *Y* corresponds to the error in Eq. (1) and variables $R_1, R_2 \ldots, R_N$ correspond to structural parameters to be optimized.

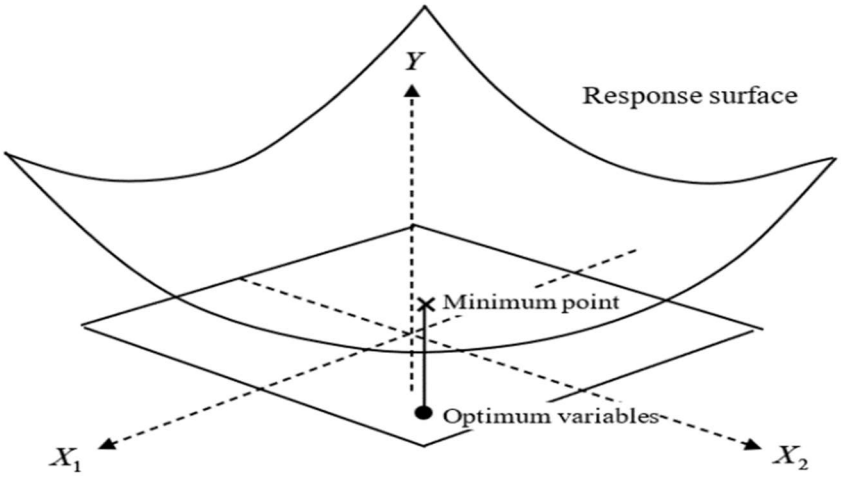

Figure 5: Response surface and optimum variables.

2.4.2. Bayesian optimization technique

The Bayesian optimization technique used in this study is provided in the free open-source GPyOpt Python module [21, 22], developed by the Machine Learning Group at the University of Sheffield. It can predict promptly and with high accuracy the optimal values that minimize the defined objective function.

For each building, a Python script is developed to predict the optimized values of the selected parameters, using only the input (lower sensor) and the target (higher sensor) acceleration waves. A first evaluation of the acceleration error (1st training data) is made for a given set of the varying parameters. A multivariate Gaussian Process (GP) [23] is then generated based on this prior knowledge and on an appropriate kernel or covariance matrix. This GP represents a first evaluation of the objective function throughout the domains of the parameters to optimize. The selection of the next evaluation point (the second set of varying parameters) is made by an appropriate acquisition function [24]. The evaluation of the acquisition function depends more often on both the distributed mean and variance of the prior GP. Its peak position defines the new set of varying parameters used to compute the next acceleration error (2nd training data). The posterior GP is then defined, and the same process is repeated as many times as specified in the program. Fig. 6 shows the flowchart of the Bayesian optimization process.

Fig. 7 presents a simple one-dimensional problem to evaluate the global minima of the function given in Eq. (20), within the range *x=[7,20]*. After only 10 evaluation points, the

parameter x that minimizes the true function (top of Fig. 7), is well estimated by the position of the acquisition function peak (bottom of Fig. 7) at a value neighboring 11. The mean distribution of the final GP fits quite well the true function with some high uncertainties where less points are selected. From this simple example, it is understood that the BOT is aimed to converge quickly to the global minima rather than to evaluate the objective function in the hole domain. The selection of the appropriate GP kernel and the acquisition function are optimized in the GPyOpt Python module.

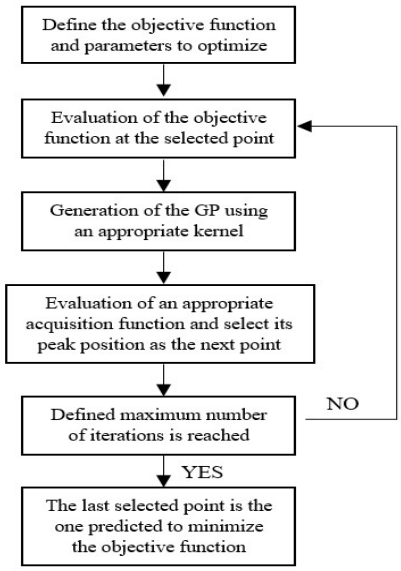

Figure 6: Bayesian optimization process.

$$f(x) = \frac{\sin(x)}{x} \tag{20}$$

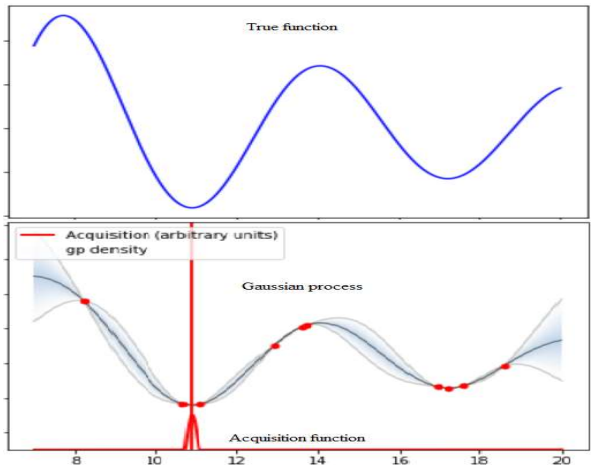

Figure 7: Bayesian optimization of 1-dimensional objective function.

Even though a higher number of iterations (about 50) was considered in the present study, the execution time of the Python script was no more than 2 minutes in all cases. This speed

of calculation represents the strength of this tool that can be adopted for a quick update of the LMM parameters; thus, to obtain a reliable seismic evaluation within a short duration after an event.

2.5. Toyohashi city hall buildings

2.5.1. Buildings overview

The Toyohashi City Hall is composed of two different buildings. The east (west) building was constructed in 1993 (1979) and contains 15 (10) stories above the ground level. Both structures consist of steel reinforced concrete (SRC) frames. Fig. 8 and Fig. 9 show an overview of these existing buildings. The 1st mode damping ratio of both structures is assumed to be equal to h=2.0%.

Figure 8: Toyohashi City Hall, East Building (TCH-EB)

Figure 9: Toyohashi City Hall, West Building (TCH-WB)

2.5.2. Input ground motion

A LAN seismometer is installed at the basement level of the west building. Recorded acceleration on June 18th, 2018, Osaka earthquake (Fig. 10) is considered as an input wave for both buildings.

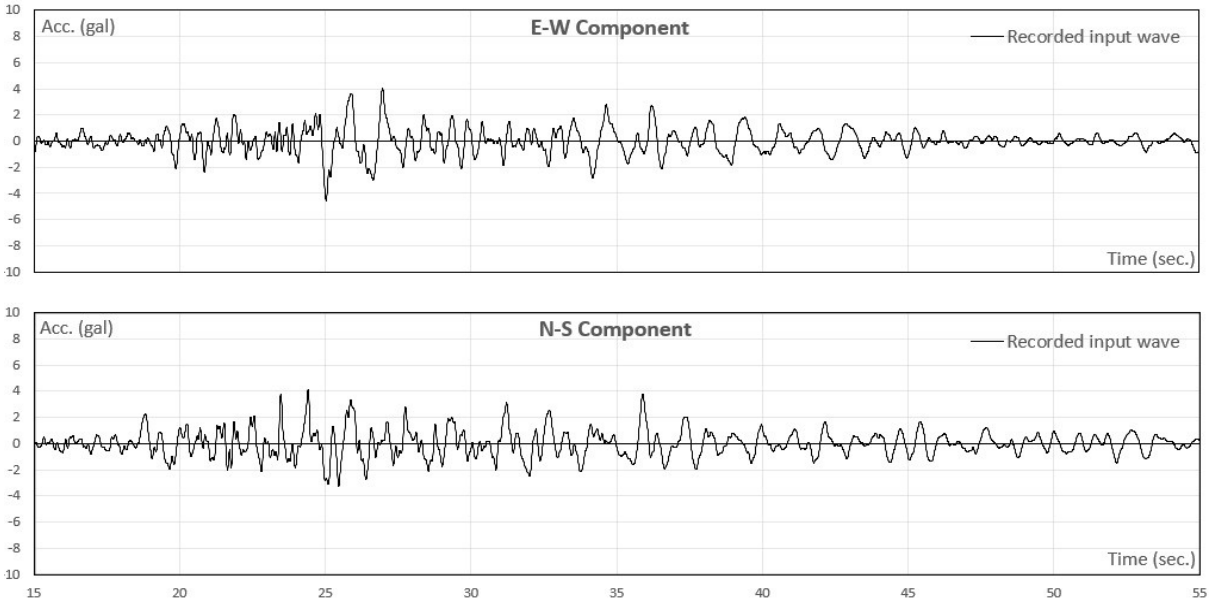

Figure 10: TCH, 1st basement floor, Recorded acceleration (2018.06.18).

2.5.3. Initial story stiffness optimization: East Building

E-W component:

Table 2.3 shows the results of optimized initial story stiffnesses by RSM and BOT and their ratio to the initial values of the LMM. Fig. 11 compares the recorded acceleration wave at the 12th floor with the simulated wave by the initial LMM, and with the optimized waves from RSM and BOT. The initial LMM fails to provide accurate results as aimed. The optimization process leads to more accurate response simulation, especially the BOT when comparing both acceleration errors (top left of Fig. 11) and wave shapes.

N-S component:

Table 4 shows the results of optimized initial story stiffnesses by RSM and BOT and their ratio to the initial values of the LMM. Most ratios are greater than 1.0, which appears to be due to the contribution of non-structural elements. Comparisons between the recorded acceleration wave, the simulated wave by the initial LMM, and the optimized waves at the 12th floor are shown in Fig. 12. The initial LMM fails to provide accurate results as aimed. The optimization process gives better results when comparing both acceleration errors, especially the BOT.

Table 3: TCH-EB, EW direction, Initial story stiffnesses optimization.

Toyohashi City Hall East Building – EW direction (*h=2%*)						
Story	Weight (kN)	Initial Story Stiffness (kN/mm)				
		Initial LMM	RSM		BOT	
			Optimized	Ratio	Optimized	Ratio
15th	2794	221	219	0.99	376	1.70
14th	10746	871	861	0.99	954	1.10
13th	15047	1501	1461	0.97	2123	1.41
12th	12040	1693	1734	1.02	2024	1.20
11th	12099	1953	1992	1.02	1353	0.69
10th	12103	2123	2155	1.02	2591	1.22
9th	12115	2410	2431	1.01	1606	0.67
8th	12804	2635	2089	0.79	1730	0.66
7th	16789	3301	3219	0.98	3836	1.16
6th	15092	3500	3068	0.88	4619	1.32
5th	15092	3811	3473	0.91	3354	0.88
4th	15144	4262	4098	0.96	4114	0.97
3rd	20617	6453	6571	1.02	5327	0.83
2nd	16752	16168	16257	1.01	19556	1.21
1st	14851	11286	11452	1.01	15762	1.40

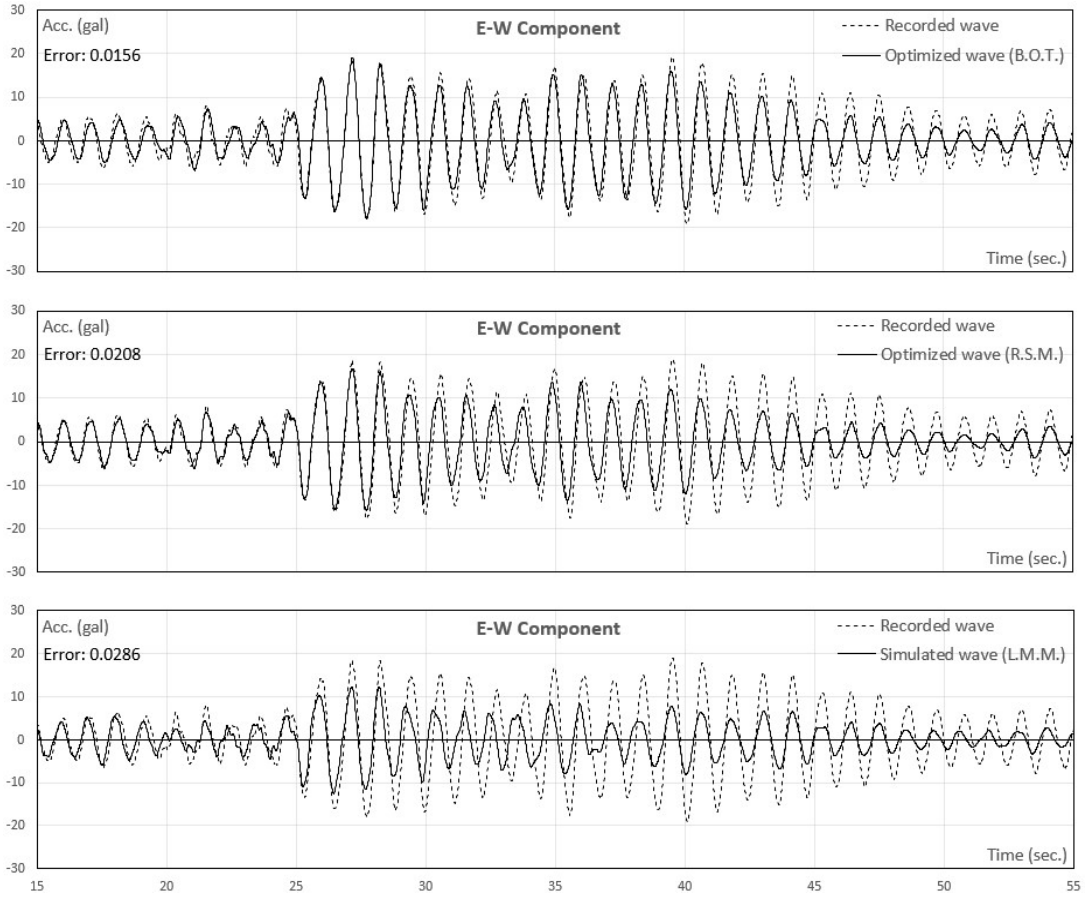

Figure 11: TCH-EB, 12th floor, Acceleration response, E-W component.

Table 4: TCH-EB, NS direction, Initial story stiffnesses optimization.

Toyohashi City Hall East Building – NS direction (*h=2%*)						
Story	Weight (kN)	Initial Story Stiffness (kN/mm)				
		Initial LMM	RSM		BOT	
			Optimized	Ratio	Optimized	Ratio
15th	2794	89	123	1.38	102	1.15
14th	10746	414	570	1.38	652	1.57
13th	15047	1466	2896	1.98	2479	1.69
12th	12040	1795	3589	2.00	3142	1.75
11th	12099	1988	3964	1.99	4569	2.30
10th	12103	2104	3031	1.44	3352	1.59
9th	12115	2283	4539	1.99	4388	1.92
8th	12804	2378	4729	1.99	4198	1.77
7th	16789	2722	4008	1.47	3594	1.32
6th	15092	2842	4234	1.49	4037	1.42
5th	15092	3020	6017	1.99	6545	2.17
4th	15144	2070	4140	2.00	3591	1.73
3rd	20617	1626	2783	1.71	2974	1.83
2nd	16752	1804	3054	1.69	2736	1.52
1st	14851	2162	3548	1.64	4088	1.89

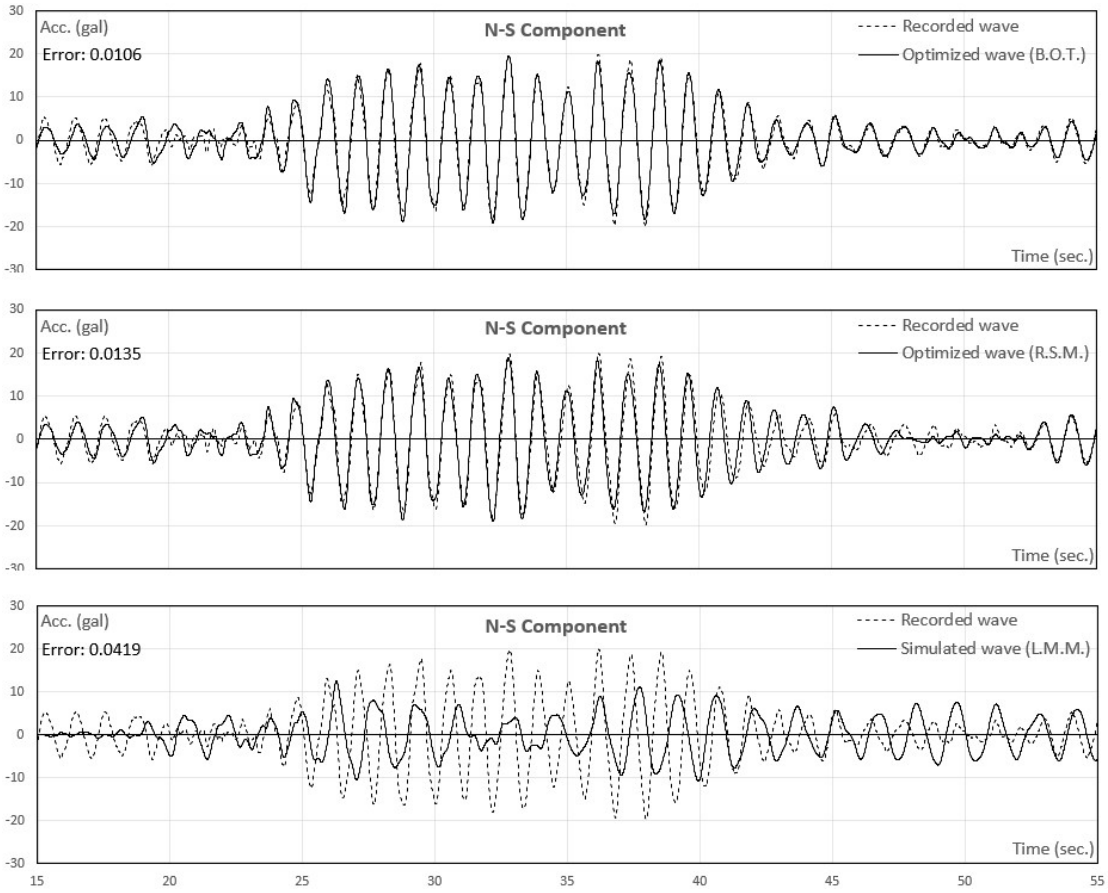

Figure 12: TCH-EB, 12th floor, Acceleration response, N-S component.

2.5.4. Initial story stiffness optimization: West Building

E-W component: Table 5 shows the results of optimized initial story stiffnesses by RSM and BOT and their ratio to the initial values of the LMM. Most ratios to initial LMM values are greater than 1.0, which appears to be due to the contribution of non-structural elements. Fig. 13 compares the recorded acceleration wave at the 7th floor with the simulated wave by the initial LMM, and with the optimized waves from RSM and BOT. The initial LMM values over-estimates the true response. Both optimization techniques give better and almost same acceleration wave although the optimized story stiffnesses are different.

N-S component: Table 6 shows the results of optimized initial story stiffnesses by RSM and BOT and their ratio to the initial values of the LMM. Fig. 14 compares the recorded acceleration wave at the 7th floor with the simulated wave by the initial LMM, and with the optimized waves from RSM and BOT. The initial LMM values over-estimates slightly the true response. Both optimization techniques gave better and almost same acceleration wave although the optimized story stiffnesses are different.

Table 5: TCH-WB, EW direction, Initial story stiffnesses optimization.

Toyohashi City Hall West Building – EW direction (*h*=2%)						
Story	Weight (kN)	Initial Story Stiffness (kN/mm)				
		Initial LMM	RSM		BOT	
			Optimized	Ratio	Optimized	Ratio
10th	4113	17560	21339	1.22	21956	1.25
9th	11767	92284	114573	1.24	121909	1.32
8th	11767	11323	13415	1.18	10835	0.96
7th	19144	9706	10759	1.11	11736	1.21
6th	19672	9297	14237	1.53	12916	1.39
5th	19156	9282	10162	1.09	10795	1.16
4th	19160	9695	12318	1.27	11571	1.19
3rd	21433	10740	13785	1.28	16197	1.51
2nd	21433	11783	14797	1.26	12588	1.07
1st	33567	13115	16493	1.26	18241	1.39

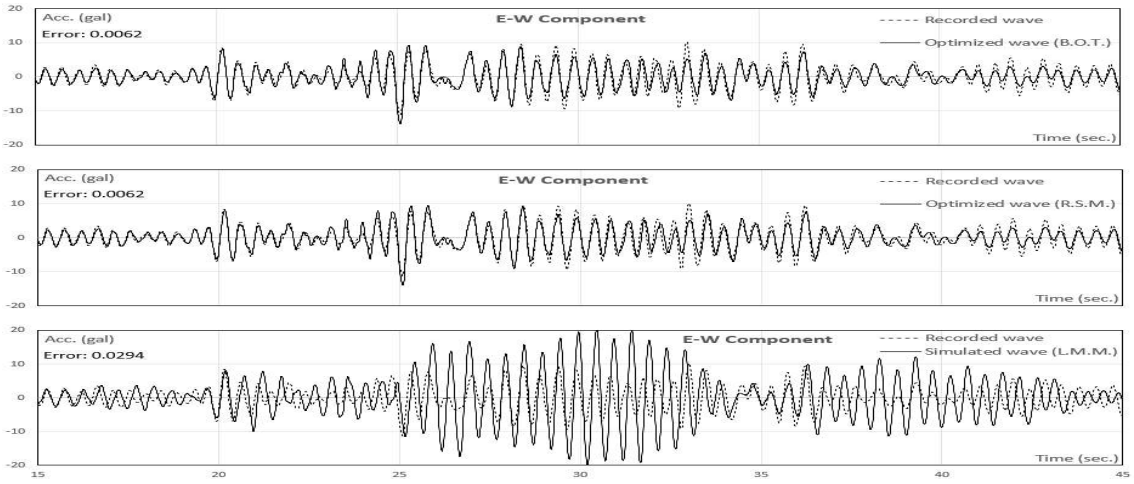

Figure 13: TCH-WB, 7th floor, Acceleration response, E-W component.

Table 6: TCH-WB, NS direction, Initial story stiffnesses optimization.

Toyohashi City Hall West Building – NS direction (*h=2%*)						
Story	Weight (kN)	Initial Story Stiffness (kN/mm)				
		Initial LMM	RSM		BOT	
			Optimized	Ratio	Optimized	Ratio
10th	4113	15034	15587	1.04	21478	1.43
9th	11767	55162	57196	1.04	53254	0.97
8th	11767	17769	18448	1.04	37918	2.13
7th	19144	13573	14139	1.04	16004	1.18
6th	19672	12129	12700	1.05	23721	1.96
5th	19156	11678	12302	1.05	10477	0.90
4th	19160	12501	13374	1.07	18563	1.48
3rd	21433	13221	14001	1.06	9317	0.70
2nd	21433	14597	15428	1.06	13243	0.91
1st	33567	15482	16304	1.05	22728	1.47

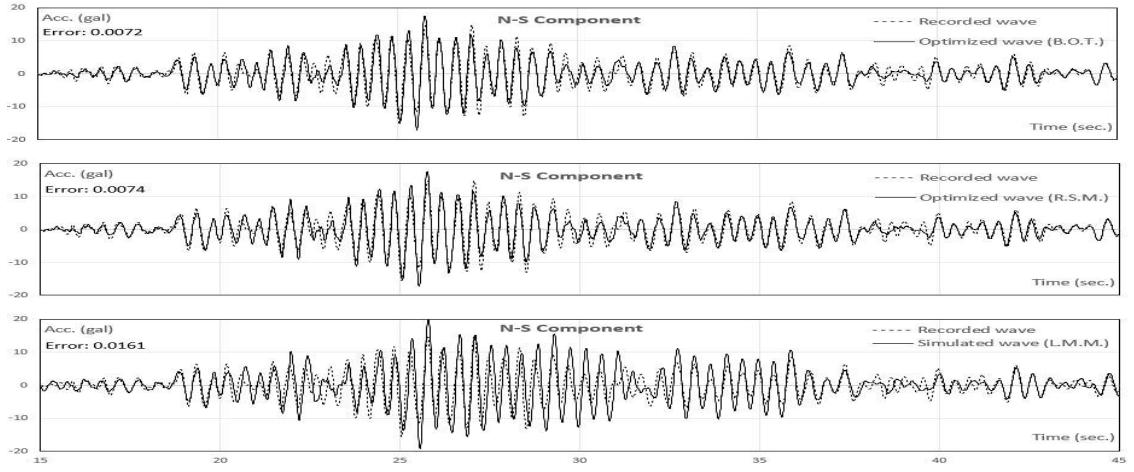

Figure 14: TCH-WB, 7th floor, Acceleration response, N-S component.

2.6. Toyohashi fire station building

2.6.1. Building overview

The Toyohashi Fire Station Building was constructed in 1993 and contains seven stories above the ground level. Its structure consists of steel reinforced concrete frames. Fig. 15 shows an overview of the buildings. The damping ratio of the first mode is assumed to be equal to *h=2.0%.*

Figure 15: Toyohashi Fire Station Building (TFSB).

2.6.2. Input ground motion

A LAN seismometer is installed at the 1st basement level of the TFSB. Recorded acceleration on June 18th, 2018, Osaka earthquake (Fig. 16) is considered as an input wave for the optimization process.

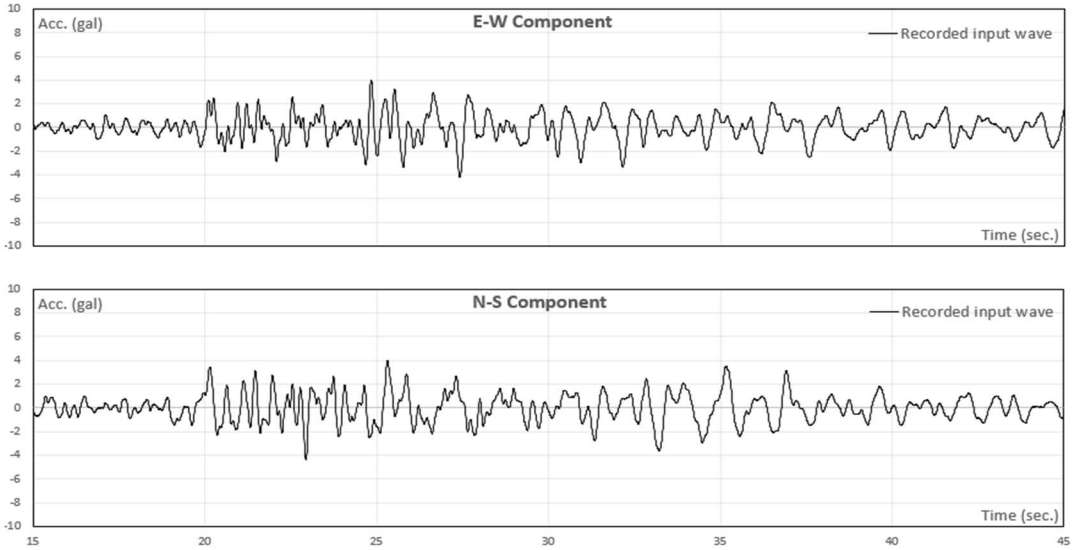

Figure 16: TFSB, 1st basement, Recorded acceleration (2018.06.18).

2.6.3. Initial story stiffness optimization

E-W component: Table 7 shows the results of optimized initial story stiffnesses by RSM and BOT and their ratio to the initial values of the LMM. All ratios to LMM are greater than 1.0, which appears to be due to the contribution of non-structural elements. Fig. 17 compares the recorded acceleration wave at the 6th floor with the simulated wave by the initial LMM, and with the optimized waves from RSM and BOT. The initial LMM fails to provide accurate results as aimed. The optimization processes provided better and quite similar results, with a preference for the BOT, when comparing both acceleration errors (top left of Fig. 17).

Table 7: TFSB, EW direction, Initial story stiffnesses optimization.

Toyohashi Fire Station Building – EW direction (*h=2.5%*)						
Story	Weight (kN)	Initial Story Stiffness (kN/mm)				
		Initial LMM	RSM		BOT	
			Optimized	Ratio	Optimized	Ratio
7th	10587	667	1165	1.75	975	1.46
6th	11833	1011	1585	1.57	1379	1.36
5th	12412	1370	2183	1.59	2121	1.55
4th	13043	1605	2716	1.69	2897	1.80
3rd	12470	1974	3395	1.72	3707	1.88
2nd	12482	2424	4063	1.68	3445	1.42
1st	14570	3988	6267	1.57	7856	1.97

N-S component: Table 8 shows the results of optimized initial story stiffnesses by RSM and BOT and their ratio to the initial values of the LMM. All ratios to LMM are greater than 2.0, which appears to be due to the contribution of non-structural elements. Fig. 18 compares the recorded acceleration wave at the 6th floor with the simulated wave by the initial LMM, and with the optimized waves from RSM and BOT. The initial LMM fails to provide accurate results as aimed. LMM update using initial story stiffnesses optimized by the BOT, could simulate more accurately the acceleration response at the 6th floor. The RSM provided similar results for this case study.

Table 8: TFSB, NS direction, Initial story stiffnesses optimization.

Toyohashi Fire Station Building – NS direction (*h=2.5%*)						
Story	Weight (kN)	Initial Story Stiffness (kN/mm)				
		Initial LMM	RSM		BOT	
			Optimized	Ratio	Optimized	Ratio
7th	10587	756	2156	2.85	1512	2.01
6th	11833	1077	3813	3.54	4706	4.37
5th	12412	1476	4490	3.04	3452	2.34
4th	13043	1751	5412	3.09	6471	3.70
3rd	12470	2128	6662	3.13	5422	2.55
2nd	12482	2497	7862	3.15	9582	3.84
1st	14570	3960	12579	3.18	14690	3.71

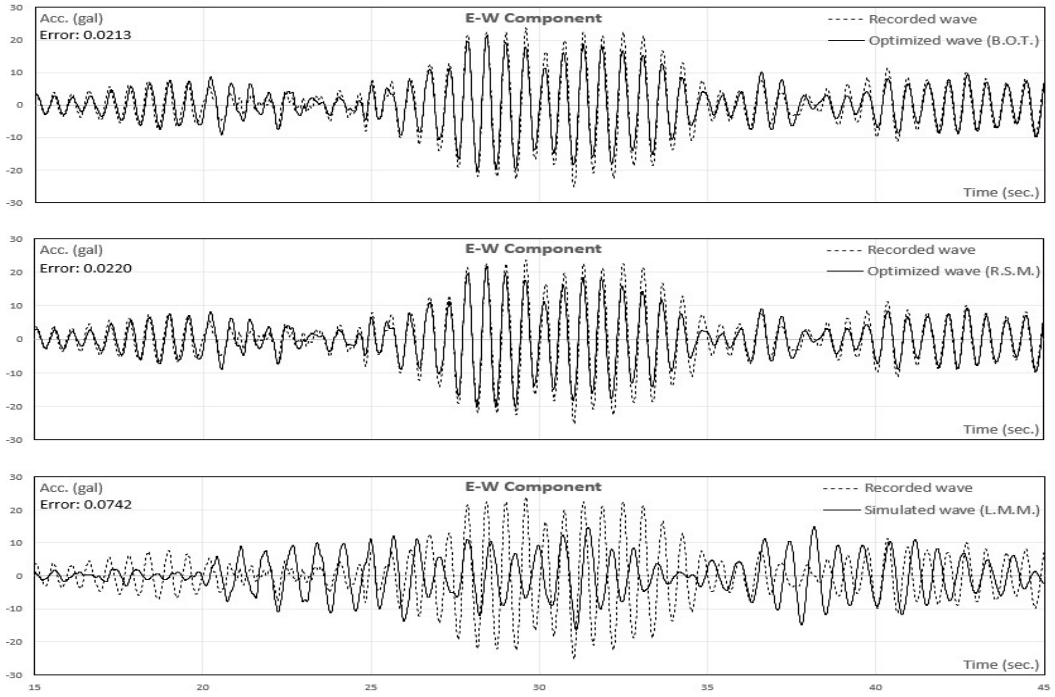

Figure 17: TFSB, 6th floor, Acceleration response, E-W component.

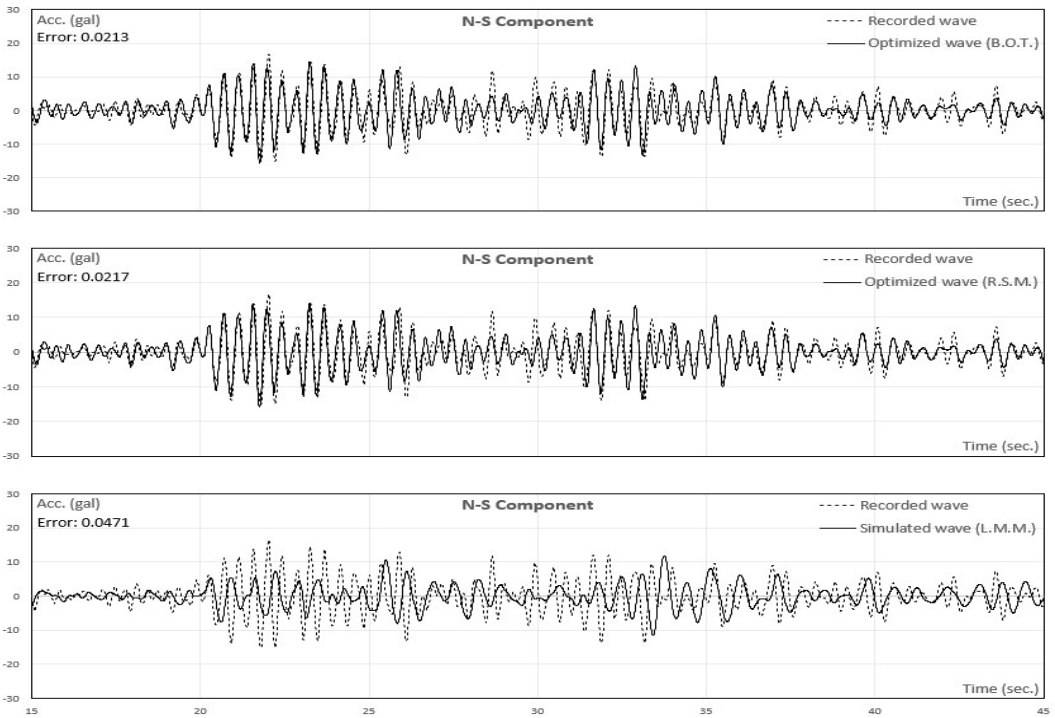

Figure 18: TFSB, 6th floor, Acceleration response, N-S component.

2.7. Model building

2.7.1. Building model

The model building is a 4-story LMM. The story hysteresis model is considered bi-linear with a post-stiffness ratio of 10%. The damping ratio of the first mode is assumed to be equal to *h=3%*. The purpose of this study is to check the efficiency of the BOT in case of nonlinear structural behavior. A one-dimensional time history analysis is carried out.

2.7.2. Input ground motion

The N-S component of El Centro Earthquake of May 18th, 1940, is considered as input ground motion, as shown in Fig. 19.

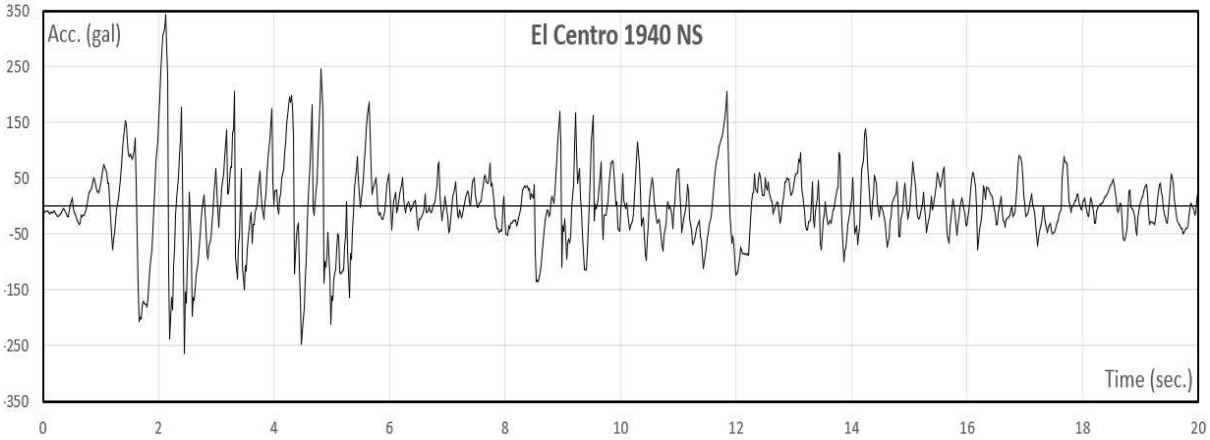

Figure 19: El Centro Earthquake of May 18th, 1940, Acceleration, N-S component.

2.7.3. Initial story stiffness and yield strength optimization

Table 9 shows the results of optimized initial story stiffnesses and the story yield strengths stiffnesses by RSM and BOT and their ratio to the initial values of the LMM. All optimized values are almost equal to those of initial LMM because there are no sources of uncertainties such as the case of real buildings (non-structural elements, soil-structure interaction, material properties…). This result confirms the power of the proposed optimization tool.

Table 9: Model Building, Story stiffness and yield strength optimization.

Model Building (MB) (*h=3%*, *Post-yield stiffness ratio=10%*)							
Story	Weight (kN)	Initial Story Stiffness (kN/mm)			Story yielding strength (kN)		
		Initial LMM	BOT		Initial LMM	BOT	
			Optimized	Ratio		Optimized	Ratio
4th	4894	2772	3085	1.11	1848	2076	1.12
3rd	3669	4473	5109	1.14	2982	3479	1.17
2nd	3691	5139	5846	1.14	3426	3400	0.99
1st	3762	4103	3563	0.87	4103	4121	1.01

Fig. 20 compares the hysteresis loops, Fig. 21 the shear history and Fig. 22 the displacement response at each floor from both initial LMM and updated one by BOT. The shear and displacement errors are computed similarly to Eq.(1). The optimized waves fit very well with the simulated waves. Given the fact that all the optimized results are deduced only by knowing acceleration response at the 3rd floor, the BOT proves again its capacity to provide accurate results in a very short time and with limited data.

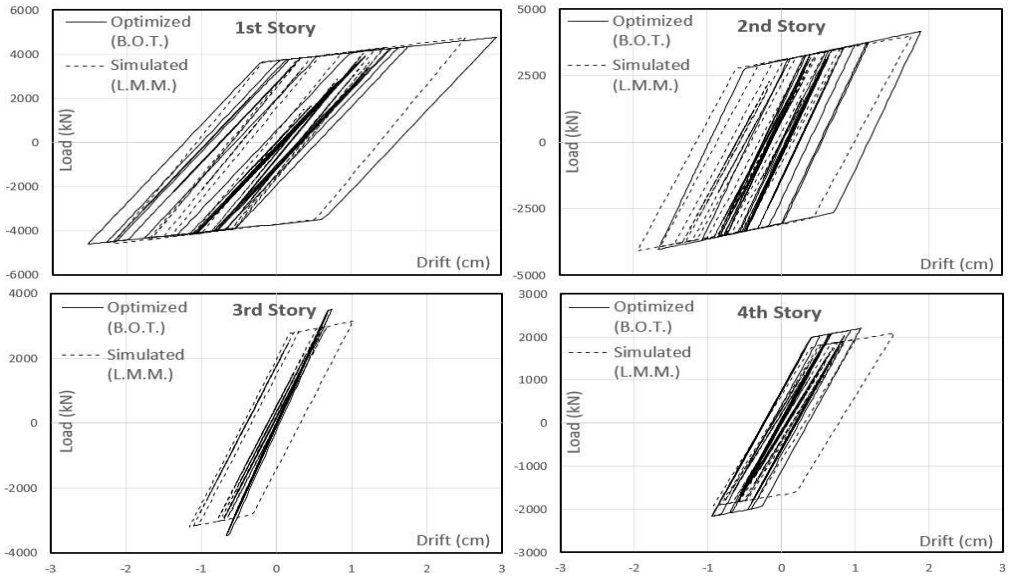

Figure 20: Model Building, Story hysteresis loops.

Figure 21: Model Building, Story shear history.

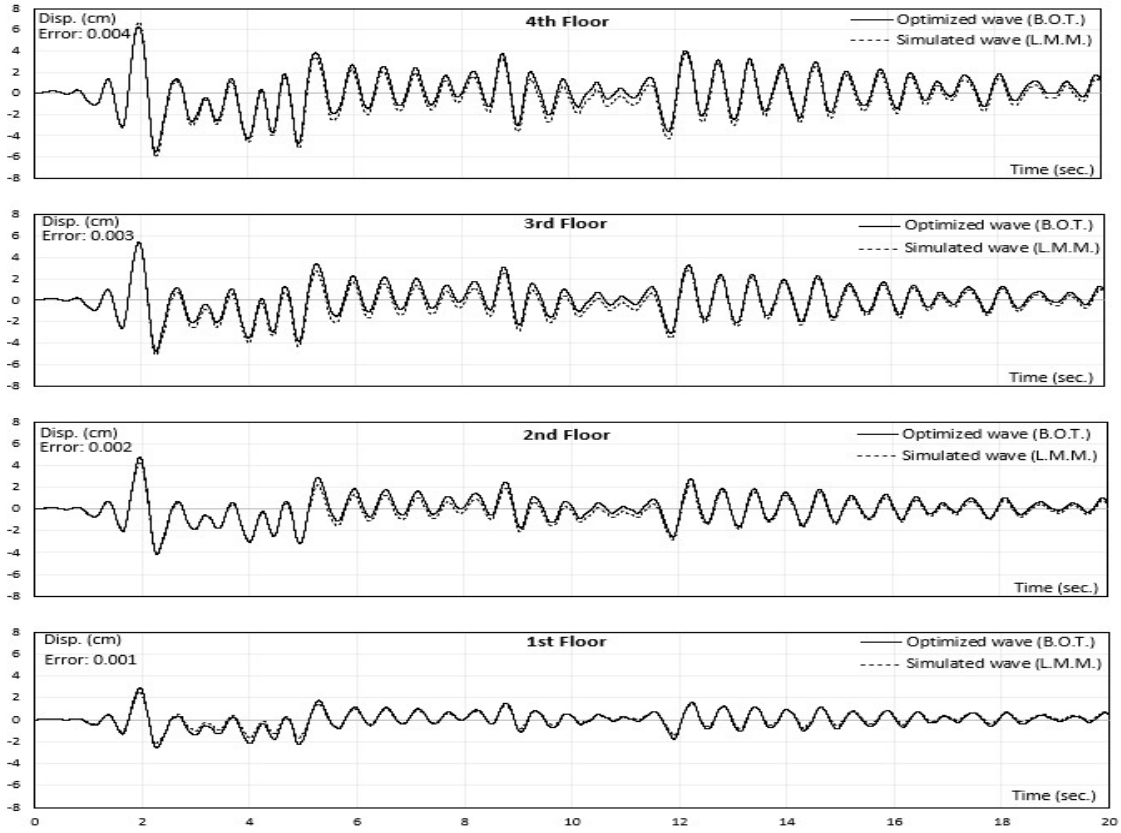

Figure 22: Model Building, Story displacement response.

2.8. Conclusion

Optimization of structural parameters of building models is essential to improve the accuracy of the real-time seismic diagnosis system of Aichi prefecture in Japan, established at TUT. Two optimization methods, Response Surface Method (RSM) and Bayesian Optimization Technique (BOT), were investigated to update the initial LMMs of target existing buildings using very limited acceleration records.

Acceleration responses of updated LMMs fit very well with recorded wavs of studied buildings. The BOT showed constantly higher accuracy than RSM and less computational time. In case of TCH-EB, BOT took around 2 minutes to perform 50 iterations in a common laptop, whereas RSM took more than 10 hours.

Moreover, the BOT could also perform well the non-linear case study. The developed Python script is considered as a program to be implemented in the seismic diagnosis system for online LMM updating; thus, for a more reliable 1st stage seismic evaluation.

Chapter 3: DEEP LEARNING MODELS OF STRUCTURAL COMPONENTS

3.1.Introduction

The hybrid seismic analysis [25] described further in Chapter IV, combines advantages of both mechanics-based and data-driven methods The seismic response of a building structure is simulated based on both analytical models and machine learning models (MLMs) simultaneously. The MLM of the target substructure (namely the seismic isolation layer) is designed/trained/tested using synthetic data, then implemented within an explicit time-integration method to make predictions at each time-step of computation. Seismic responses of three isolated building models subjected to four different ground motions, showed very good agreements with reference analyses. With the scope to validate the hybrid analysis experimentally, this Chapter focuses on the 1st and fundamental step of developing the surrogate models. Synthetic and measured data in full-scale isolated building specimens tested at E-Defense in August 2011 [26], are used in this Chapter to design MLMs capable of predicting the structural behavior of model isolation systems, and of specific seismic isolation devices, namely triple pendulum bearing (TPB) and lead rubber bearing (LRB) respectively.

3.2.Target structural components

3.2.1. Triple pendulum bearing device (TPB)

TPBs are passive seismic isolation devices that decouple a building structure from its foundations through sliding over concave surfaces. The instantaneous supported weight and coefficient of frictions control the amount of dissipated kinematic energy (friction damping), while the recentering mechanism is ensured by the curved geometry of the sliding surfaces. Originally developed and tested with a single concave sliding surface [27, 28], it has been adapted to contain double [29, 30], triple [30], and multiple [31] pendulum systems to withstand different levels of ground shaking. The inner structure of a TPB device is shown in Fig. 23.

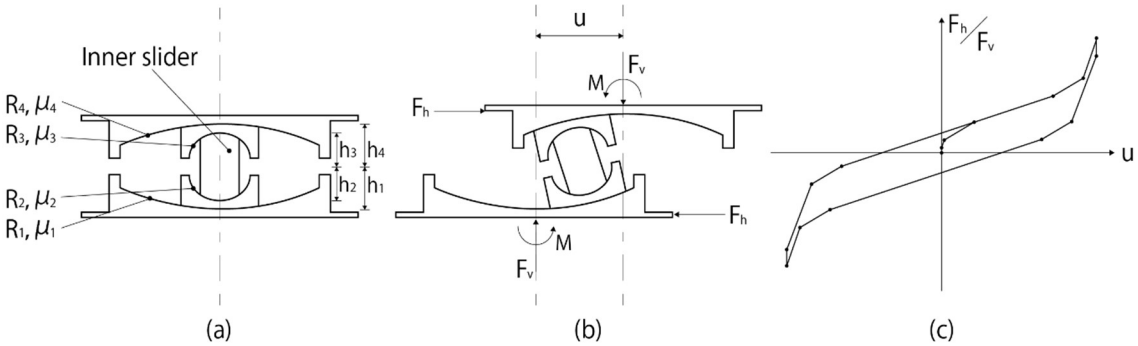

Figure 23: TPB: (a) undeformed state; (b) deformed state; (c) conventional model.

It has four stacked sliding plates and a rigid inner slider, all made from a steel alloy with appropriate longevity and resistance. From bottom to top, the radii of curvature (coefficients of friction respectively) of the sliding surfaces are referred as R_1, R_2, R_3, and R_4 (μ_1, μ_2, μ_3, and μ_4 respectively). The effective radius of a sliding surface R_{eff} is defined as the radius of curvature minus the radial distance h to the center of the inner slider, $R_{effi}=R_i-h_i$. Commonly used TPBs are fabricated with $R_{eff1}=R_{eff4}>R_{eff2}=R_{eff3}$ and, in theory, $\mu_2=\mu_3<\mu_1<\mu_4$ resulting to three distinct pendulum systems. Depending on the initial frictional resistance and the displacement capacity of each sliding surface, Fenz and Constantinou [30] formulated piecewise linear models to map the normalized horizontal force F_h/F_v to the relative displacement between the outer plates u, based on the free body diagrams of TPB components. This one-dimensional model has been revised by Sarlis and Constantinou [32] to include the effect of eccentric axial forces and inertia forces at each TPB component. Becker and Mahin [33] formulated a non-linear kinematic model that captures the bi-directional behavior of a TPB device without any restriction on frictional and geometric properties. Aforementioned analytical models alongside with others [34, 35], showed satisfactory results under the same constraints. However, reported validations by experimental data of single TPB device are very limited quantitively and qualitatively. Most of tests are performed on scaled TPB devices subjected to unrealistic loading conditions such as sine waves and/or constant axial load and/or one-dimensional motion. In actual conditions, TPBs are expected to undergo more complex three-dimensional loading and the dependency of the frictional coefficient on the instantaneous velocity, temperature, and axial pressure [36, 37] is more complicated than some proposed empirical formulas. To the best knowledge of the authors, no exhaustive experimental validation of a device analytical model has been reported so far.

3.2.2. Lead rubber bearing device (LRB)

As shown in Fig. 24, LRB is an elastomeric bearing composed of laminated rubber for vertical load support and restoring mechanism, and a central lead plug for energy dissipation; all in one single unit. Yielding of the lead plug dissipates the seismic energy through generation of heat and its mechanical properties are recovered few minutes later [38, 39, 40], justifying the choice of this material. Since its invention in the 1970′s by a research team headed by W. H. Robinson [41], smooth bilinear models are still commonly used in practice to describe the hysteretic behavior. More sophisticated models have been developed to incorporate other features such as the strength degradation [42, 43, 44], the strain hardening at large shear deformations [45], and the unloading effects [46]. As it is the case for TPB models, most of experimental validations are performed under less representative conditions of scaled LRB devices and/or sinusoidal loading and/or constant axial load and/or one-dimensional motion. More realistic experimental tests on full-scale LRB devices [47, 48, 49] highlighted the influence of the shear strain, the strain

rate, and the coupling of three-dimensional loading on the force-displacement characteristics. Other hysteretic shapes such as pinching around zero-displacement and strength/stiffness degradations have been observed as well. Many physical phenomena behind the behavior of LRB have already been identified including, but not limited to, the heating of the lead core [39, 40], the buckling in compression [50], the rubber cavitation in tension [51], and the torsional deformation in two-dimensional motion [52]. As of today, the development of a generalized analytical model capturing the real behavior of LRBs under representative conditions is still an unfulfilled task.

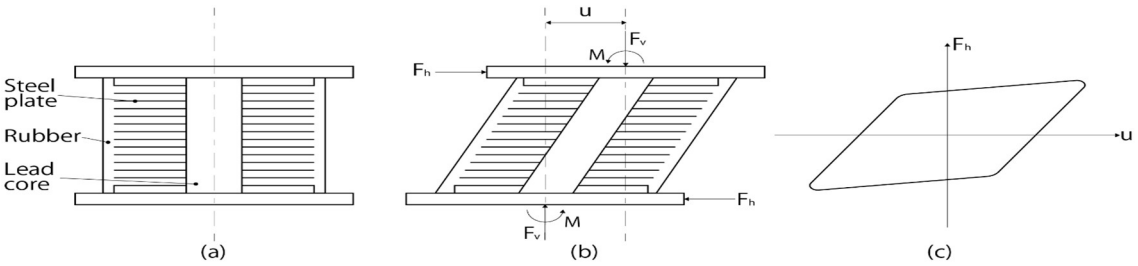

Figure 24: LRB: (a) undeformed state; (b) deformed state; (c) conventional model.

3.2.3. Model isolation system

Three MLMs simulating three artificial isolation layers are designed in this Chapter. Each isolation layer is formed by Natural Rubber Bearing (NRB), Lead Rubber Bearing (LRB), and Oil Damper (Oil), as shown in Fig. 25. The combination of both NRB and LRB devices is assumed to perform a bilinear hysteresis behavior. The force developed in the Oil Damper device is assumed to depend only on the relative velocity of its edges. The three buildings were designed according to Japanese engineering practice [53] and modeled using the software STERA_3D [3]. Tables 10 provides all properties of the three isolation layers.

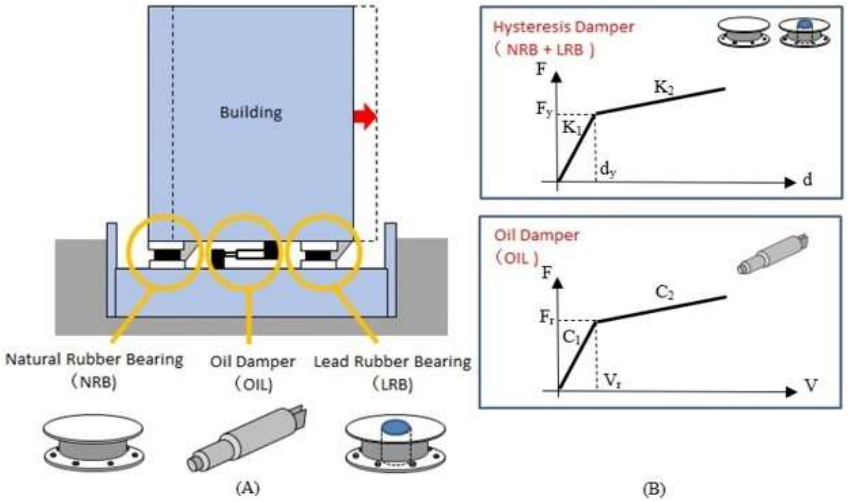

Figure 25: Overview of studied isolation layers and its constitutive devices.

Table 10: Simulated isolation layers properties

Isolation Level No.			1	2	3
Oil Damper	C_1	(kN.s/mm)	2.194	1.617	1.237
	C_2/C_1		0.067	0.067	0.067
	V_r	(mm/s)	320	320	320
LRB+NRB	K_1	(kN/mm)	175.5	129.4	99
	K_2/K_1		0.046	0.042	0.031
	F_y	(kN)	1755	1294	990
ML model designation			MLM1	MLM2	MLM3

3.3.Available structural data

3.3.1. Experimental data: E-Defense test program of August 2011

TPB (LRB respectively) deformation and loading data measured in 20 (14 respectively) different runs of the aforementioned E-Defense test program, are used in this Chapter to develop, and to test a deep learning model capable of predicting the two-dimensional shear time history of the single device. Derived datasets represent realistic loading conditions that include the influence of a full-scale superstructure and a variety of strong ground motions with different amplitudes, durations, and frequency contents. An experimental validation of these surrogate models on such an extensive and representative data would be challenging, unique, and very promising towards an implementation in the hybrid seismic analysis [25].

Shake-table tests were conducted on a full-scale building specimen isolated consecutively by a group of nine identical TPB devices, then by a combination of four identical LRB and cross linear bearing (CLB) devices. Fig. 26 shows an overview of the 5-story steel moment frame superstructure and a typical TPB and LRB connection assembly. Additional eccentric weight, in the form of steel plates, was added at the roof level to induce intentionally torsional vibrations. The total weight of the building was about 5300 kN. The two support configurations are presented in Fig. 27. The isolation layer was instrumented by load cells beneath each isolation device, accelerometers at top connecting plates, three horizontal displacement transducers (wire pots) along each direction, and six laser transducers for vertical displacement. All records are with the same sampling frequency of 1000 Hz, which is enough to capture nonlinearities. A comprehensive and detailed description of both specimens can be found in references [49, 55].

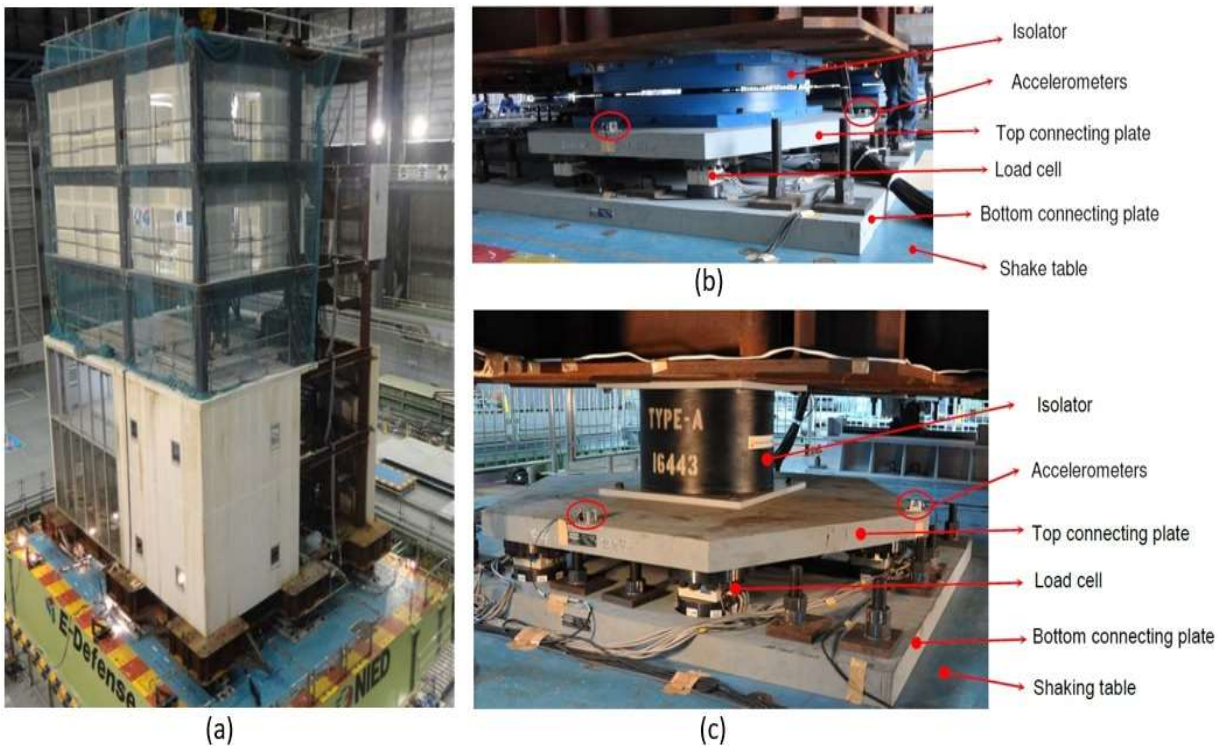

Figure 26: Overview of tested specimen [49, 55]: (a) Superstructure; (b) TPB; (c) LRB.

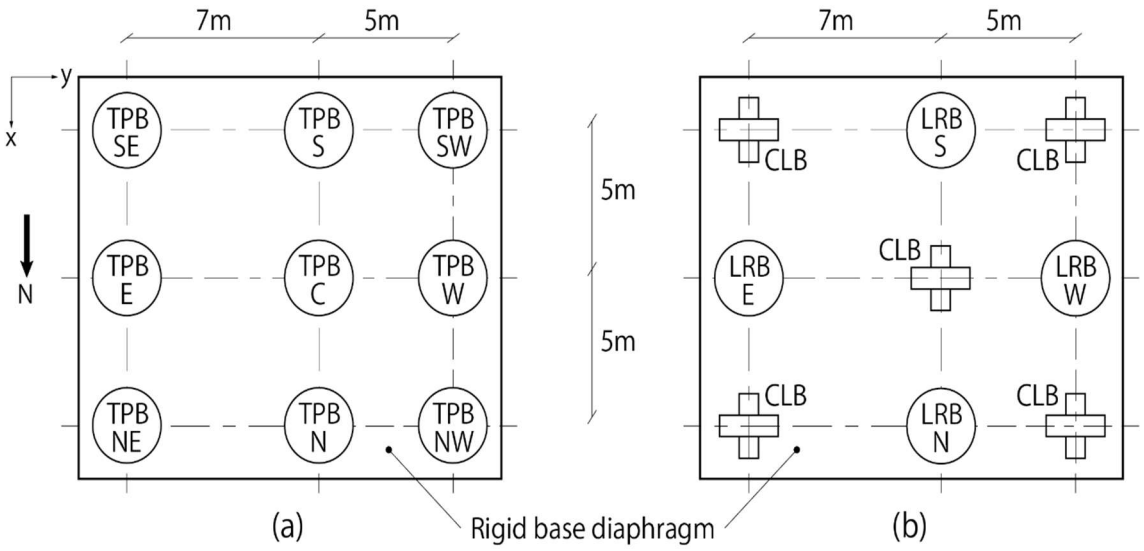

Figure 27: Support configurations: (a) TPB system; (b) LRB/CLB system.

All table motions considered in this study to develop the TPB and LRB MLMs are listed in Table 11 and Table 12 respectively, following the test program sequence. Four accelerometers recorded the table motion at the corners. These records are first filtered (Butterworth bandpass filter [0.1, 20] Hz), then averaged to evaluate the peak table acceleration (*PTA*) of each component

and to draw the corresponding horizontal velocity response spectra (S_v) as illustrated in Fig. 28 and Fig. 29. Data recorded at the isolation level, covering a wide range of amplitudes, frequency contents, and durations, were processed to generate datasets for training and testing the MLMs.

Table 11: TPB isolation system: Realized table motions used in this study.

TM No.	Designation	Reference motion	Scale factor	PTA (gal)			Duration (sec.)
				X	Y	Z	
1	Sin65	Sinusoidal (1D)	65%	98	-	-	35
2	Sin100		100%	138	-	-	
3	WSW80	1987 Superstition Hills-Westermorland	80%	163	149	105	40
4	ELC130	1940 Imperial Valley-El Centro (3D)	130%	286	453	259	40
5	RRS-3D	1994 Northridge-Rinaldi Rec. Sta. (3D)	88%	541	1186	1195	20
6	SYL100	1994 Northridge-Sylmar (3D)	100%	666	1120	502	22
7	TAB50	1978 Tabas-Tabas Sta. (3D)	50%	568	449	321	35
8	LGP70	1989 Loma Prieta-Los Gatos (3D)	70%	443	504	546	25
9	TCU50	1999 Chichi-TCU065 (XY)	50%	441	273	-	60
10	TCU70		70%	631	373	-	
11	IWA100	2011 Tohoku-Iwanuma (XY)	100%	394	562	-	180
12	TAK100	1995 Kobe-Takatori (3D)	100%	769	900	260	40
13	KJM100	1995 Kobe-JMA Kobe (3D)	100%	669	867	398	35
14	RRS-2D	1994 Northridge-Rinaldi Rec. Sta. (XY)	88%	509	1167	-	20
15	TCU80	1999 Chichi-TCU065 (XY)	80%	730	413	-	60
16	TAB80	1978 Tabas-Tabas Sta. (3D)	80%	838	810	537	35
17	TAB90	1978 Tabas-Tabas Sta. (XY)	90%	903	971	-	35
18	TAB100		100%	906	1101	-	
19	SCT100	1985 Mexico City-SCT (XY)	100%	173	103	-	60
20	TAK115	1995 Kobe-Takatori (3D)	115%	920	1063	270	40

PTA: Peak table acceleration.

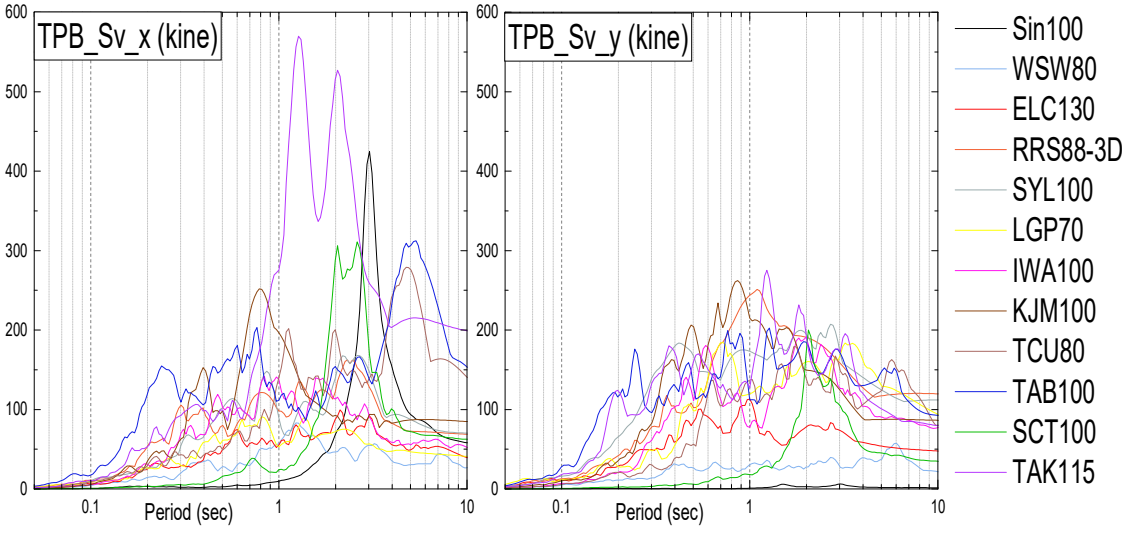

Figure 28: TPB system: Velocity response spectra of used table motions (h=5%).

Table 12: LRB/CLB isolation system: Realized table motions used in this study.

TM No.	Designation	Reference motion	Scale factor	*PTA* (gal)			Duration (sec.)
				X	Y	Z	
1	Sin-1	Sinusoidal (1D)	100 %	-	270	-	20
2	VOG75-1	Synthetic ground motions (3D) [49]	75 %	365	229	209	30
3	VOG100		100 %	486	319	289	
4	VOG125		125 %	617	422	358	
5	VOG150		150 %	759	522	424	
6	VOG175		175 %	902	620	477	
7	DIA80	Synthetic ground motions (XY) [49]	80 %	854	618	442	30
8	DIA95		95 %	1050	754	-	
9	ELC130	1940 Imperial Valley-El Centro (3D)	130 %	283	453	272	40
10	IWA100	2011 Tohoku-Iwanuma (XY)	100 %	396	554	17	180
11	RRS-2D	1994 Northridge-Rinaldi Rec. Sta. (XY)	88 %	487	1107	-	20
12	RRS-3D	1994 Northridge-Rinaldi Rec. Sta. (3D)		487	1114	1171	
13	VOG75-2	Synthetic ground motion (3D) [49]	75 %	362	231	212	30
14	Sin-2	Sinusoidal (1D)	100 %	-	274	-	20

PTA: Peak table acceleration.

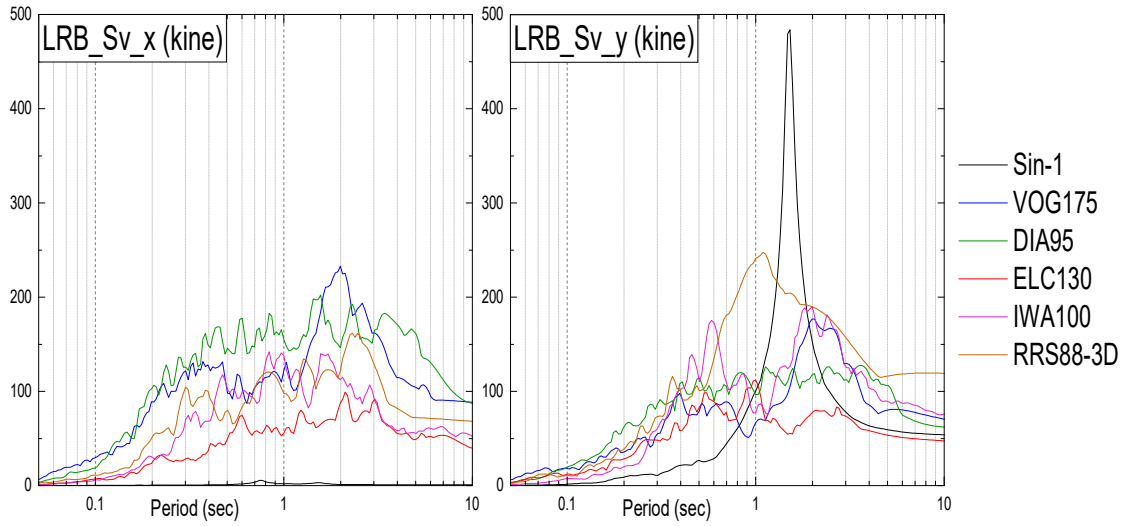

Figure 29: LRB/CLB system: Velocity response spectra of used table motions (h=5%).

Considering the rigidity of the base diaphragm and possible torsional oscillations, compatibility of isolators hysteresis loops of the same run is checked to exclude all devices with excessively irreconcilable data. This data cleaning step is necessary to keep only reliable sequences for the development of MLMs. Therefore, 158 (55 respectively) samples of two-dimensional hysteresis data are selected for the TPB (LRB respectively) device.

3.3.2. Synthetic data: Simulated by STERA-3D

Synthetic data were generated to develop MLM1, MLM2, and MLM3 (Table 10), simulating the behavior of the respective isolation layers (NRB + LRB + Oil Damper). To this end, NTHAs are performed on equivalent 1DOFs with random natural periods and inherent viscous damping. Five ground motions (GMs) are used to generate the synthetic dataset. They

were intentionally derived from famous earthquake records with different amplitudes, frequency content, and duration as shown in Table 13 and Fig. 30.

Table 13: Overview of earthquake ground motions used to generate synthetic data.

GM No.	Ground Motion Designation	Earthquake Event Occurrence Date	PGA (Gal)	Duration (s)	Acceleration Sparkline	Usage in This Study
1	Kobe 1995 NS	17 January 1995	818	5		Tuning network architecture
2	Kobe 1995 NS	17 January 1995	818	15		Training the MLM Hybrid analysis (Ch. IV)
3	Taft 1952 EW	21 July 1952	176	19		Testing the MLM Hybrid analysis (Ch. IV)
4	Tohoku 1978 NS	12 June 1978	258	23		Testing the MLM Hybrid analysis (Ch. IV)
5	El Centro 1940 NS	18 May 1940	342	27		Testing the MLM Hybrid analysis (Ch. IV)

Ch. IV: Chapter IV.

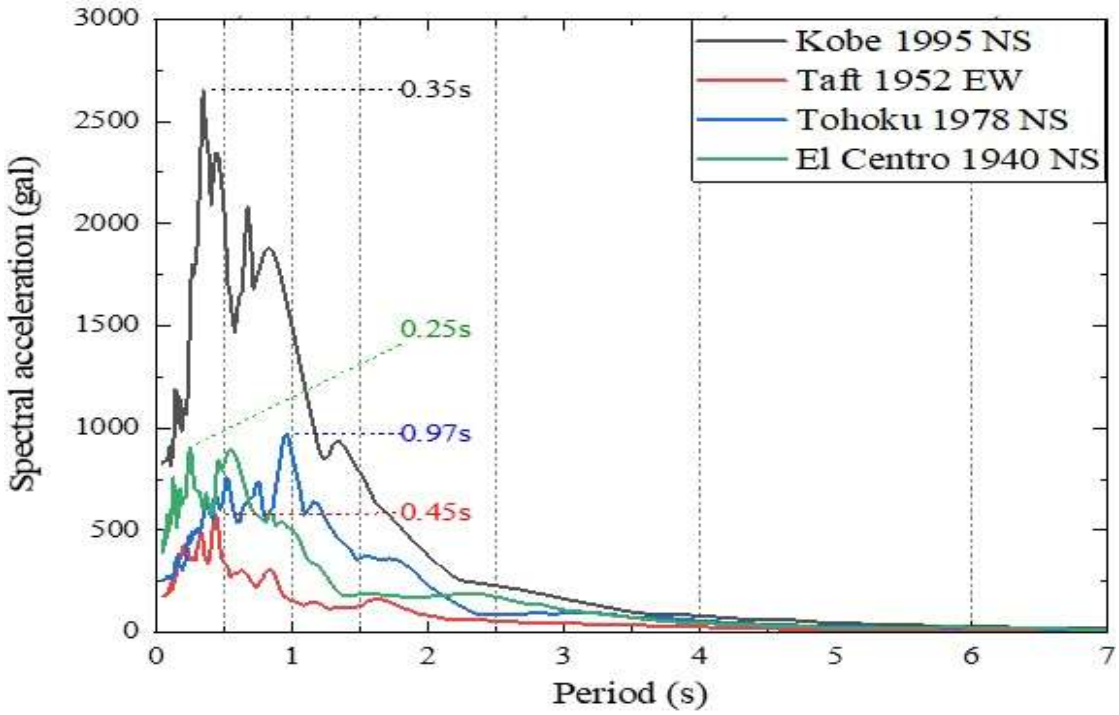

Figure 30: Acceleration response spectra of GM used to generate synthetic data.

By varying randomly the natural period and the inherent damping of the 1DOF, 50 samples of Deformation/Shear time histories are generated for each GM and isolation layer.

3.4.Training and testing data

Splitting of the TPB and LRB datasets into training and testing data is not random. It is intentionally based on their original runs to minimize the size of the training data (which is often faced in real life problems), and to ensure that testing data contain different characteristics than

those used for training. Criteria to select the appropriate original runs for training data are explained further in Section 6.

MLMs simulating model isolation layers were trained by synthetic datasets generated from GM2. Those generated from GM3, GM4, and GM5 were used for testing.

3.5.Machine learning algorithms

Artificial neural networks (ANNs) are the ML algorithms used in this study to simulate the complex hysteretic behavior of target isolation devices. The basic ANN algorithm is the multilayer perceptron (MLP) presented in Fig. 31. The network architecture consists of fully connected input layer, hidden layers, and eventually the output layer. Each layer is formed by many units/cells/neurons which perform basic linear operations combined with an appropriate activation function.

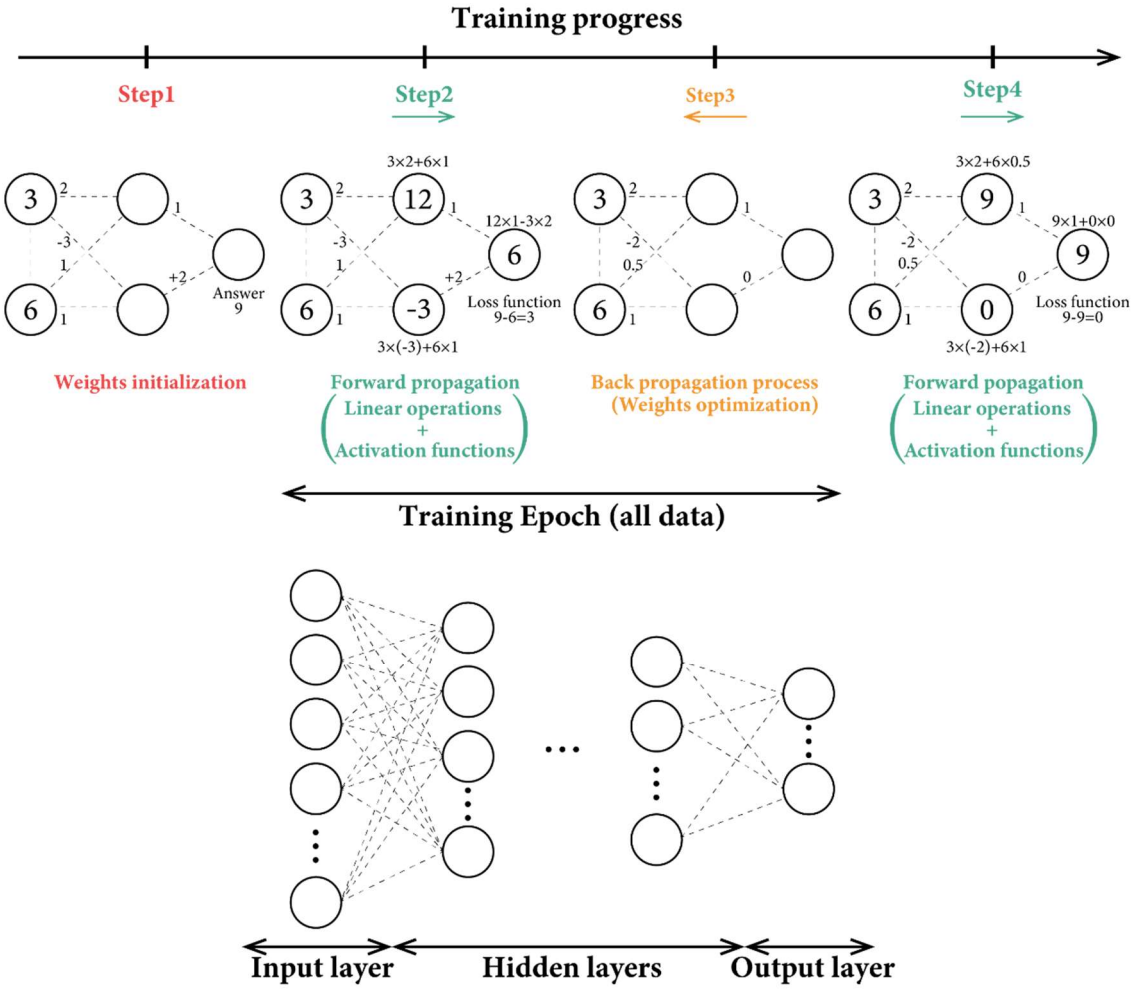

Figure 31: Overview of the MLP algorithms and architecture.

The prediction problem of this study consists of the evaluation of the force-deformation hysteresis of target isolation devices. It deals with sequences with variable lengths. Therefore, RNNs [54] are selected for the regression prediction problem because they are initially designed to deal with sequence data, and they allow to make predictions on sequences with different lengths (different durations). Fig. 32 presents an overview of RNN architectures and most common units/cells/neurons. The study offers a new application of this class of ANNs, rather than advances or descriptions of their algorithms.

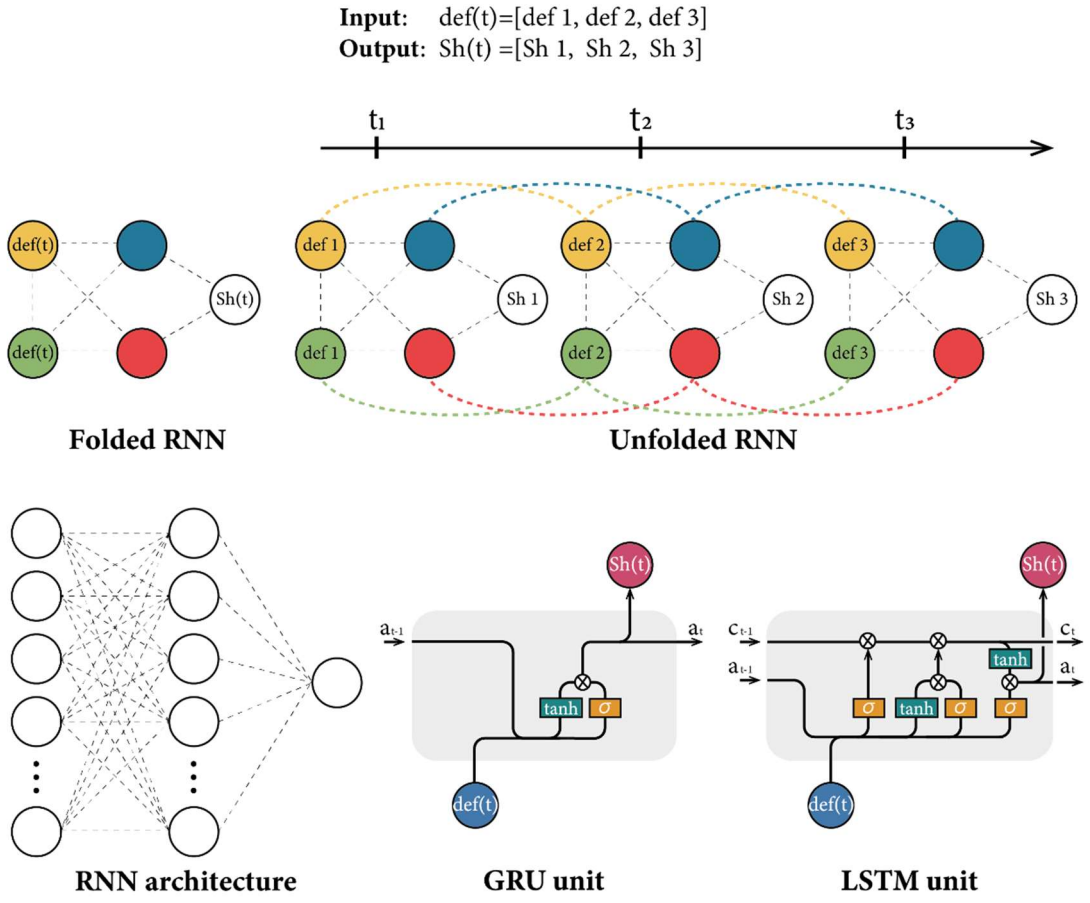

Figure 32: Overview of RNN algorithms and architecture.

3.6.Framework for developing the machine learning models

Methodologies adopted in this study to develop RNN models are presented in Fig. 33 (for experimental data) and Fig. 34 (for synthetic data). Python scripts were made to process the data and to design the models using the TensorFlow machine learning library under Python 3.6. All trainings are performed on a computer with 16 Intel® Xeon® W-2245 CPUs and 1 NVIDIA RTX 5000 GPU card. The frameworks presented hereafter are not limited to this study but may be used to design RNN models for similar sequence-to-sequence prediction problems.

3.6.1. Flowchart for experimental data

Stage 1-Data preprocessing: For a target isolation system and a table motion, all needed raw data at the isolation level are first selected. It consists of records from load cells beneath all isolation devices, accelerometers at top connecting plates (Fig. 26), and horizontal displacement transducers. Corresponding waves are filtered, except the load cell data beneath TPB bearings to avoid omitting signal spikes that may results from pounding of its components when reaching displacement limits and following an uplift excursion [55, 57, 58]. Then, the data are preprocessed to derive the 3D loading and the X-Y displacement time histories of each isolation device. For consistency matter, the same derived data in references [49, 55] are used in this study. Considering the rigidity of the base diaphragm and possible torsional oscillations, compatibility of hysteresis loops of the same run is checked to exclude all devices with excessively irreconcilable data. This data cleaning step is necessary to keep only reliable sequences for the development of MLMs. At this 1st Stage, 158 (55 respectively) samples of two-dimensional hysteresis data are selected for the TPB (LRB respectively) device.

Stage 2-Data processing: The two datasets derived previously must be prepared for ML. Based on the mechanical behavior of the device and on available data, the 1st step is to decide the physical nature of inputs and outputs. The axial load and X-Y displacement time-histories are undoubtedly the main features to include as an input. The isolation mechanism of a TPB device is based mainly on the friction proportional to the supported weight. However, the axial load on a LRB device has other instability effects such as buckling in compression [50] and cavitation in tension [51], mainly at large shear deformations. Since both LRB and CLB devices were combined in the support configuration (Fig. 27), a vertical load transfer to CLBs has been identified at large deformations during the performed tests [49]. The vertical stiffness of CLBs is much higher than LRBs and this load-transfer phenomenon is expected whenever these two types of devices are rigidly connected by a base diaphragm. Local rotations of bearings may influence their behavior as well, but such data are unavailable. Eventually, three features are selected as inputs for the TPB MLM, namely the axial force and the X-Y displacement time histories. For the LRB model, the X-Y displacement time histories are assumed sufficient for this problem. Both models output the X-Y shear time histories. Designing the network architecture is an extremely computational task; thus, only the first 10 seconds of each time sequence are used for the next Stage 3. Then, selected architectures are trained/tested with longer sequences (30 seconds/full durations) at Stages 4/5. All displacement and shear waves are shifted in such a way to vanish the initial offset, then splitting and zero-padding through time were performed on training data for size augmentation. Since selected features (displacement, axial force, shear) have

different ranges, their corresponding sequences are scaled by the maximum absolute value to optimize the learning behavior during the backpropagation process [59]. Eventually, input and output data are shaped into three-dimensional vectors: [samples, time-steps, features].

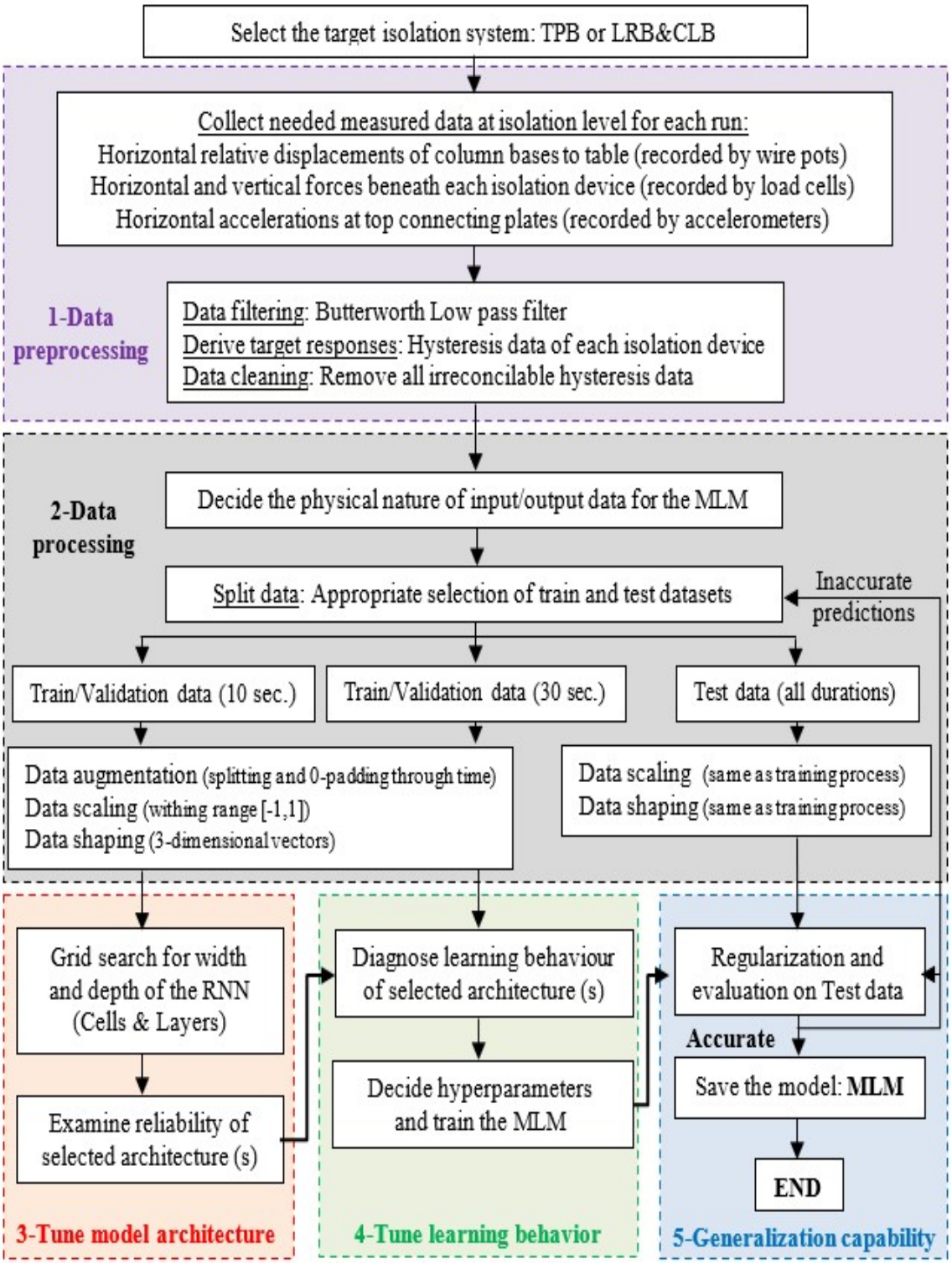

Figure 33: Framework for developing and testing MLMs with experimental data.

Stage 3-Tune model architecture: The architecture of a RNN consists mainly of the number of hidden layers (depth), the number of cells of each layer (width), and the type of the recurrent cell. Two RNN cell variants, namely Long Short-Term Memory (LSTM) [60] and Gated Recurrent Unit (GRU) [61], are commonly used since they both outperform traditional recurrent units and their respective performances are comparable [62, 63, 64]. For a given sequence-to-sequence prediction problem and dataset, designing a RNN architecture is still an open issue and is done mainly by trial-and-error process. Furthermore, a single evaluation of the performance of an ANN is not enough considering the aleatory uncertainty of the training process (weight initialization and shuffling of data). Therefore, a wide range of GRU/LSTM candidate architectures are considered, then trained/evaluated 10 times each before selecting the most appropriate ones. A reliability analysis is performed on selected architectures by repeating the training/evaluation process 10, 20, 30, 40, and 50 times in order to check further its robustness. Statistical comparisons are performed through Box and Whisker plots. The selection is based on a trade-off between accuracy/precision and model simplicity. To this end, the mean square error (MSE) of Eq. (21) and the number of trainable parameters are used as indexes respectively. MSEs are dimensionless since they are evaluated on scaled data.

$$MSE = \frac{\sum_{data}(Reference\ value_i - Predicted\ value_i)^2}{N_{data}} \tag{21}$$

Stage 4-Tune learning behavior: MSEs evaluated at Stage 3 are performances of models trained on reduced sequences (first 10 seconds) and up to 250 epochs. However, final models should be trained on more representative sequences (estimated to 30 seconds for this problem), and the learning behavior has to be diagnosed throughout more epochs for better understanding of the progressive learning. Previously selected architectures are trained up to 1500 epochs and their training and validation losses are analyzed and compared in order to decide the final network architecture and training hyperparameters (epochs, loss function, optimizer, batch size, learning rate, …).

Stage 5-Generalization capability: As opposed to synthetic data, experimental records contain the epistemic uncertainty of measurement. Overfitting on training data would lead to a worthless MLM that can't make good predictions on new unseen sequences. The regularization of the model is performed to prevent any undesirable overfitting. Dropout ratios [65] from 10% to 50% are applied to the hidden layer of the final architecture. Resulting models are trained with the same dataset and hyperparameters, then their respective performances are evaluated on both train and test data to check the generalization capability. The influence of different dropout ratios is discussed, and the one leading to the least MSE on test data is saved as the final MLM. It is

worth mentioning that the generalization capability of developed TPB and LRB MLMs is previously improved through the appropriate selection of training data at Stage 2, and the optimization of the MLM at Stages 3/4. By following the proposed methodology, no further iterations may be needed.

3.6.2. Flowchart for synthetic data

Stage 1: Given the displacement time history of the target isolation layer (NRB + LRB + Oil Damper), the MLM would predict the corresponding shear force-time history. Samples of displacement/shear time histories need to be generated by performing NTHAs of the equivalent 1DOF system having a deformation and velocity-dependent hysteresis behavior as presented in Table 10. Natural periods and inherent viscous damping are chosen randomly with the goal to reach the displacement limit of the target isolation layer (here, fixed to 25 cm). Data derived from GMs 1 and 2 are used to develop the MLMs (Stages 3 and 4), and those corresponding to GMs 3, 4, and 5 are used for testing (Stage 5). The five seconds duration of GM 1 is chosen for the only reason to optimize the computation time of Stage 3. Even though a large artificial dataset could be generated, only 50 Samples are produced intentionally to simulate often-faced cases of a small experimental dataset.

Stage 2: Training ANNs needs as much clean data as possible. Artificial samples generated in this study are supposedly clean. A data augmentation technique is performed to offer a solution for the intentionally generated small dataset: One-second splitting and 0-padding of sequences through time were enough to feed Stage 3 with 250 samples and Stage 4 with 750 samples. These training datasets are scaled by the maximum absolute value to be within the range $[-1,1]$ to avoid any exploding or vanishing gradient descent during the backpropagation process [59]. Then, datasets are shaped into 3-dimensional vectors: Samples, time steps, features. The test data are scaled and shaped similarly, but no size augmentation is needed.

Stage 3: ANNs are stochastic models. The same architecture trained by the same data and with the same hyperparameters leads to different predictions. The randomness of both network weights initialization and splitting to training and validation data generates an aleatory uncertainty. All candidate architectures are trained many times, and their final performances are summarized in a Box and Whisker plot to select the most appropriate one based on accuracy and precision. Ten acts of training (runs) per case are performed for the first level screening to choose between the two most common types of RNN cells: LSTM [60] and GRU [61]. Then, 20 runs of training per case are performed for the second level screening to select the network architecture. In order to test further the reliability of the final network, batches of 10, 20, 30, 40, and 50 independent acts of training were performed to analyze the scattering of its final performances.

The range of candidate architectures and the number of training repetitions are limited only by the computation resources; the reason why sequences corresponding to 5 s duration (derived from GM1) are trained up to 500 epochs for this stage is to obtain a good balance between model reliability and computation effort. Model performance is evaluated by computing the MSE of Eq. (21) between normalized reference values and predicted ones.

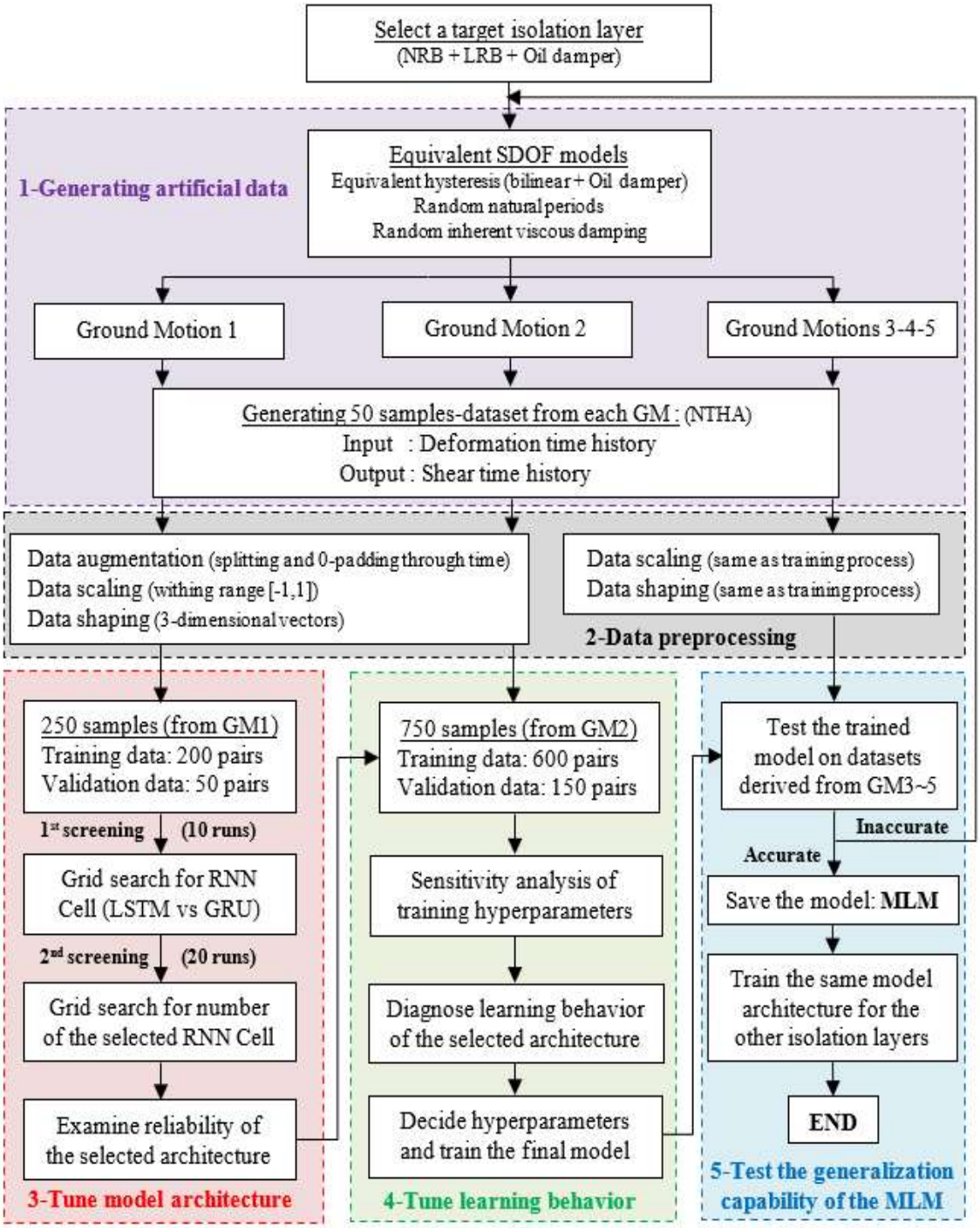

Figure 34: Framework for developing and testing MLMs with synthetic data.

Stage 4: Given the same data and the same network architecture, hyperparameters such as the loss function [66] (the performance assessment metric), the optimizer [67] (the algorithm used to update the network weights), the batch size (the amount of data loaded for each weights update), and the number of training epochs, may influence the learning behavior of the model. A sensitivity analysis to hyperparameters is performed, followed by a deep diagnosis of the learning behavior through training epochs. The objective of this stage is to decide the appropriate hyperparameters among widely used ones and to train the final MLMs on full-length sequences derived from GM2. The same performance assessment metric of Stage 3 (MSE) is used for that purpose.

Stage 5: Developed MLMs are tested on a new unseen dataset derived from GMs 3, 4, and 5. MSEs are computed for the three test sub-datasets containing 50 samples each. For the visualization of each model performance, shear time history predictions of a few random test samples are unscaled, then combined with their respective displacement time histories to draw the corresponding nonlinear cyclic hysteresis loops. In order to keep the same unit of the original waves, the Root Mean Square Error (RMSE) of unscaled sequences ($Shear_{Ops}$ versus $Shear_{Predicted}$) is evaluated as follows:

$$Shear\ RMSE\ (kN) = \sqrt{\frac{\sum_{time}\left(shear_{Ops,i} - shear_{Predicted,i}\right)^2}{N_{time\ steps}}} \tag{22}$$

3.7.Surrogate models for specific LRB and TPB devices

3.7.1. Appropriate selection of training data

Both the size and the quality of training data are crucial to design an efficient MLM. Since available data in civil engineering practice is often limited, a minimalist selection of training data is carried out intentionally to develop the final models. The size is then augmented by splitting and zero-padding through time (Stage 2). Samples should cover the widest range possible of influencing parameters: for the problem treated in this study, deformation, velocity, axial force (only for TPB), and shear force are considered. Even though the strain rate is not an input for ML, a well-designed RNN could infer such an information from the displacement sequence.

To highlight aforementioned issues, six different sets of training data are selected deliberately for each isolator type, to train the same RNN architecture (GRU network of reference [25]) up to 1500 epochs. Tables 14 and 15 show the original runs of training data for each MLM. The 1st set is derived from sinusoidal runs (similar to standard test protocols), the 2nd contains low amplitude sequences (large size but incomplete), and the remaining sets (3rd→6th) contain progressively extreme performances realized by the isolators (displacement, velocity, shear force

in both X and Y directions, and the axial force for the TPB case). The sinusoidal run is added as it is the only one-dimensional strong motion available, and MLMs are expected to learn the structural behavior under both one- and two-dimensional horizontal motions.

Table 14: Selection of training data for TPB MLMs.

Original runs of training data					
TPB MLM1	TPB MLM2	TPB MLM3	TPB MLM4	TPB MLM5	TPB MLM6
Sin65	Sin65	TAB100	TAB100	TAB100	TAB100
Sin100	WSW80	-	TAK115	TAK115	TAK115
-	ELC130	-	-	RRS-3D	RRS-3D
-	SYL100	-	-	LGP70	LGP70
-	KJM100	-	-	-	Sin100

Table 15: Selection of training data for LRB MLMs.

Original runs of training data					
LRB MLM1	LRB MLM2	LRB MLM3	LRB MLM4	LRB MLM5	LRB MLM6
Sin-1	VOG75-1	DIA95	DIA95	DIA95	DIA95
-	ELC130	-	VOG175	VOG175	VOG175
-	-	-	-	Sin-1	Sin-1
-	-	-	-	-	RRS-2D

Resulting MLMs ($1^{st}\rightarrow6^{th}$) are tested on their corresponding remaining data (derived from the remaining runs), which contain new unseen sequences. Fig. 35 shows the size of train data (in blue) and the MSE on test data (in red) for each case. The worst performance is realized for the TPB and LRB MLM1, trained by low amplitude sequences derived from the one-dimensional sinusoidal motions. The large size of the 2^{nd} datasets was not sufficient to design generalizable MLMs (second highest MSEs). By choosing progressively appropriate training data ($3^{rd}\rightarrow6^{th}$), MSEs on test data decreased significantly. This case study emphasizes the importance of preparing appropriate training data, in terms of both size and quality. Datasets used to train the TPB/LRB MLM6 (5/4 runs out of 20/14; 36/16 samples) are considered for the rest of this study, and 20% of which are used for validation. The first 10 seconds duration of each sequence are used to design the network architecture (360/160 samples after data augmentation), and the first 30 seconds duration for training the final MLMs (1080/480 samples after data augmentation).

3.7.2. Artificial neural network architecture

A study of nonlinear hysteresis prediction [25] highlighted that a stacked RNN model of two hidden layers of 60 GRU units each, and an output dense layer was enough to make accurate predictions of wavy bilinear hysteresis loops. However, the data used herein represent a

more realistic and complicated loading conditions of full-scale isolation devices and contain the epistemic uncertainty of measurement. Therefore, the aforementioned RNN architecture is taken as a minimum capacity, and a wider range up to 100 RNN units and 3 hidden layers is investigated herein (Fig. 36 and 37). Both GRU (red color) and LSTM (blue color) units are used to train each model 10 independent times, and final MSEs on validation data are visualized by Box and Whisker plots. For TPB models (Fig. 36), performances of both RNN units are overall similar with slightly more outliers for the LSTM case. Therefore, the simplest one (less trainable parameters) with minimum median/average values is selected: two hidden layers of 95 GRU units each. For LRB models (Fig. 37), LSTM architectures are more accurate but the two GRU hidden layers architectures are very precise. Not much gain of accuracy/preciseness is obtained by deepening networks. Thus, two candidate architectures are selected for further investigation: two hidden layers of 60 GRU (preciseness) and 70 LSTM units (accuracy) respectively.

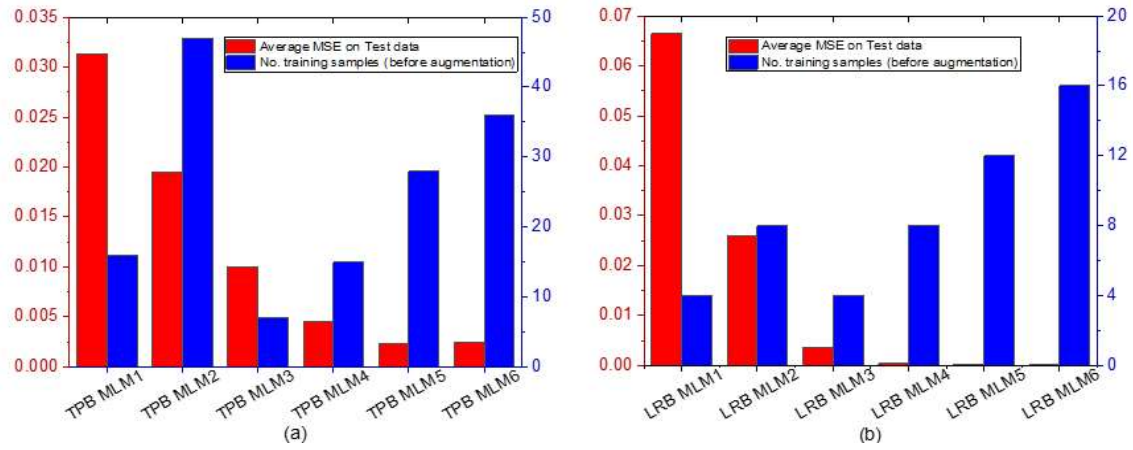

Figure 35: Influence of training data on performance: (a) TPB MLM; (b) LRB MLM.

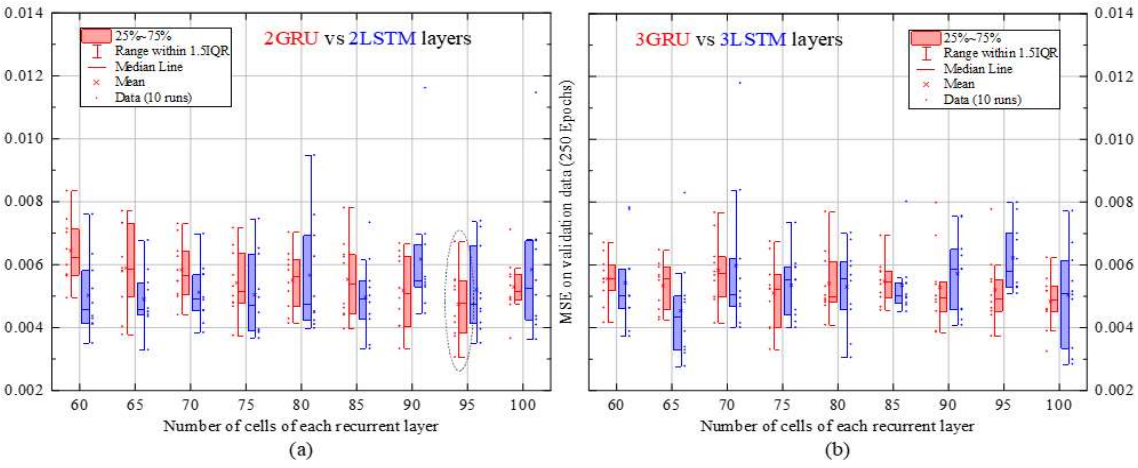

Figure 36: Random search for TPB model architecture: (a) 2 layers; (b) 3 layers.

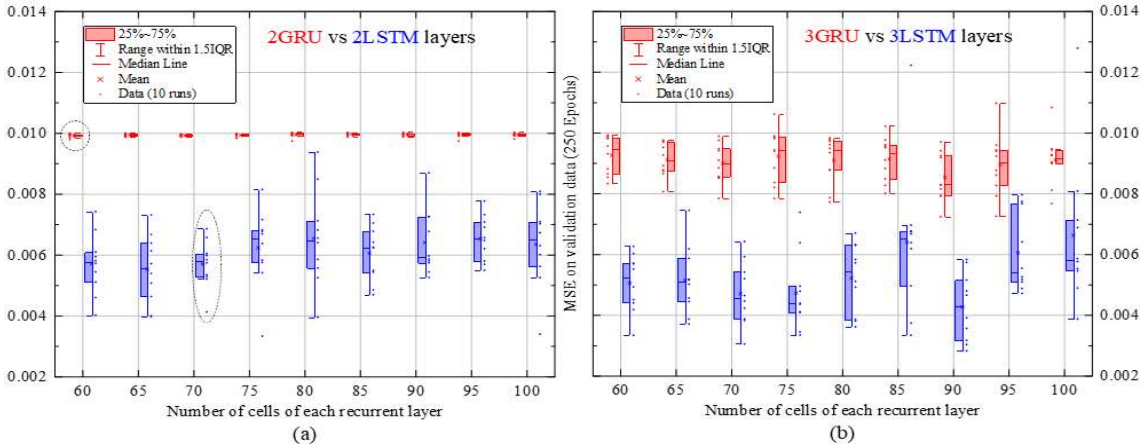

Figure 37: Random search for LRB model architecture: (a) 2 layers; (b) 3 layers.

3.7.3. Model reliability

The robustness of previously selected architectures is checked further by performing independent batches of trainings on the same dataset: 10, 20, 30, 40, and 50 runs. Fig. 38 shows the statistical distribution of MSEs on validation data. The overall performance of each architecture remains similar in terms of median/mean values, but the LSTM units lead to wider interquartile ranges and more outliers for the regression problem treated in this study. It is worth mentioning that the batches of 10 runs are different from those reported in Fig. 36-a and 37-a, highlighting the stochastic aspect of the learning process.

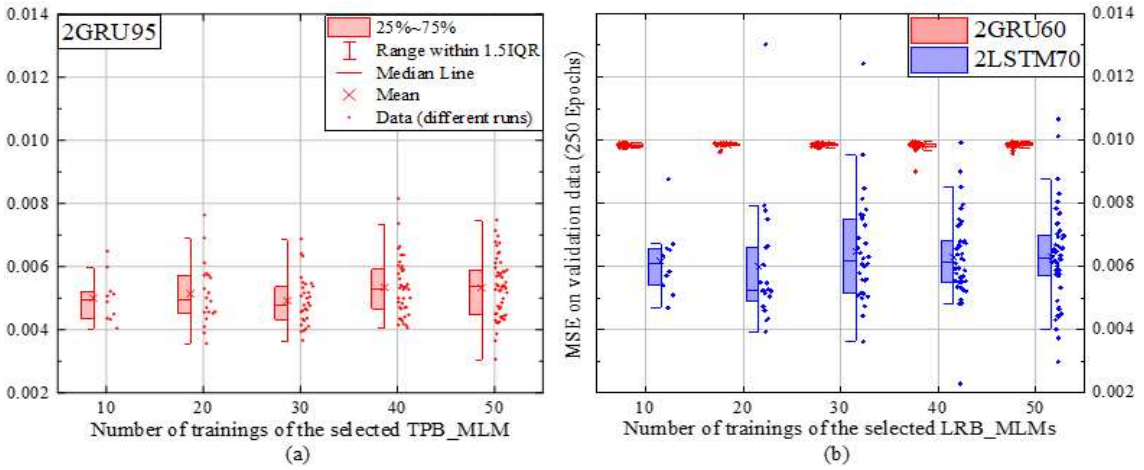

Figure 38: Reliability of selected architectures: (a) TPB MLM; (b) LRB MLM.

3.7.4. Diagnosis of learning behavior

The progressive learning of selected architectures is diagnosed through all training epochs, rather than a single evaluation at 250 epochs (Stage 3). Trainings are performed on longer and more representative sequences (30 seconds duration/30,000 time-steps) and up to 1500 epochs. As stated previously in Fig. 37-a and observed again in Range 1 of Fig. 39, the LSTM

architecture (blue color) learns faster at an early stage of training. However, a turnaround happens after 100 epochs, from which MSEs of the GRU architecture become smaller and smoother than their LSTM counterparts. The overall noisy learning behavior of the LSTM architecture explains the wider interquartile ranges and outliers highlighted in Stage 3. For the LRB MLM, the GRU architecture is selected for the rest of this study. The same smooth and stable learning behavior characterizes the GRU architecture of the TPB model, as shown in Fig. 40. MSEs on both training and validation data decrease jointly and asymptotically to a zero value.

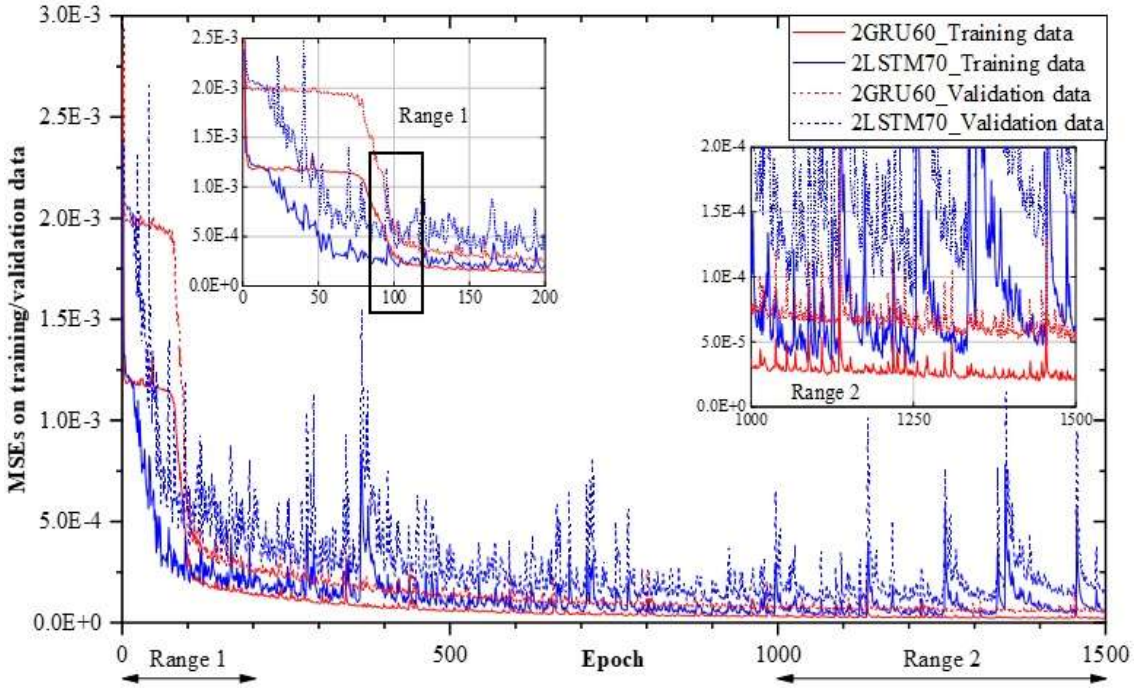

Figure 39: Learning behavior of the selected LRB MLMs.

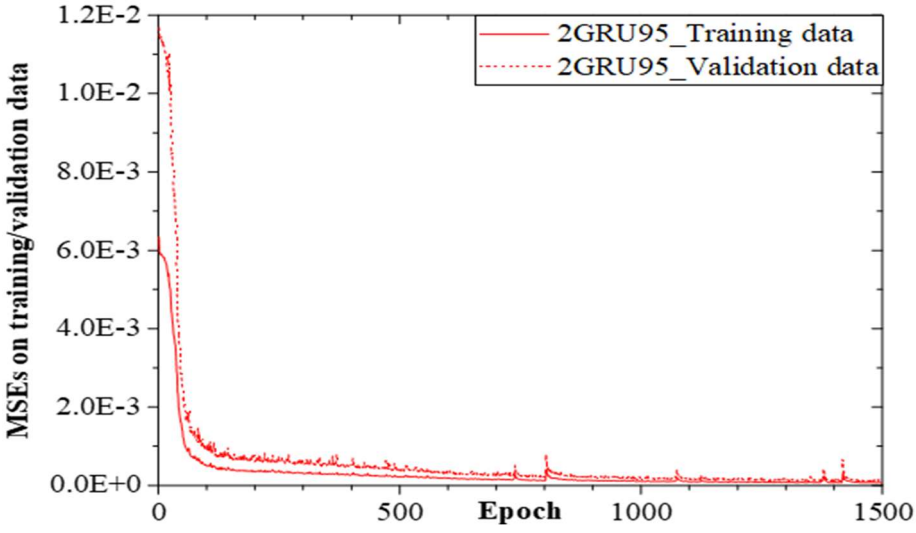

Figure 40: Learning behavior of the selected TPB MLM.

3.7.5. Testing of TPB and LRB MLMs

Dimensionless MSEs presented previously were computed on scaled data used to optimize the learning process of RNNs. The RMSE (Eq. (23)) and the coefficient of determination (R^2) on unscaled data, are provided hereafter for a better appreciation of model predictions on real scale shear data.

$$RMSE\ (kN) = \sqrt{\frac{\sum_{time}(Reference\ shear_i - Predicted\ shear_i)^2}{N_{time\ steps}}} \tag{23}$$

Final GRU architectures are evaluated on full length sequences (full duration reported in Tables 11 and 12). Since the number and content of samples derived from each run are different, grouping them all would lead to an unbalanced dataset. As shown in Tables 16 and 17, RMSEs are evaluated on sub-datasets corresponding to each table motion, and the average value is then computed for both train and test data. Bolded table motions are those used for training, and samples derived from the remaining ones are the new unseen data used for testing. Continuing the MLM numbering of Tables 14 and 15, six TPB (7→12)/LRB (6→11) models are developed depending on common dropout ratios (0~50%), then their respective performances are analyzed and compared.

The dropout technique had more beneficial effect on the LRB case (Table 17), since all average RMSEs on test data (39 samples) are smaller than the one of LRB_MLM6 (0% dropout). This regularization method often reduces the overfitting on train data as it is highlighted for the TPB case, where the TPB_MLM7 (0% dropout) has the least average RMSE on train data. The dropout ratios leading to the best performance on test data are selected, and corresponding MLMs are saved as the most generalizable within the framework proposed in this study: TPB_MLM12 (50% dropout) and LRB_MLM10 (40% dropout). As highlighted in the Tables (in bold), six representative cases are selected for predictions visualization in Section 5 and corresponding to: the sinusoidal run used for training (as the only 1D motion), the smallest and biggest errors on both train and test sub-datasets, the SYL100 motion (TPB test data) to check the model capability of predicting uplift excursions, and the IWA100 (LRB test data) long duration motion to highlight the long-term temporal dependency of developed GRU models.

For each MLM, prediction samples (red color) from the six representative cases highlighted in Tables 16 and 17, are visualized and compared with the experimental data (black color). The isolator position of each presented sample is provided in accordance with Fig. 27.

Table 16: Regularization and testing of the selected TPB architecture.

No.	Table motion	N*	RMSE (kN)_R^2 on full length sequences					
			TPB_MLM	TPB_MLM	TPB_MLM	TPB_MLM	TPB_MLM11	TPB_MLM12
			0% Dropout	10%	20%	30%	40% Dropout	50% Dropout
1	Sin65	8	08.00_0.92	09.70_0.88	08.63_0.92	09.33_0.91	09.02_0.90	08.50_0.92
2	**Sin100**	8	01.08_1.00	02.08_0.99	01.50_1.00	01.16_1.00	01.25_1.00	**01.19**_1.00
3	WSW80	8	05.63_0.88	05.27_0.90	05.38_0.84	05.84_0.83	06.51_0.84	**05.67**_0.87
4	ELC130	8	07.58_0.89	08.07_0.86	07.54_0.85	06.65_0.90	08.52_0.85	07.37_0.87
5	**RRS-3D**	4	02.42_0.99	02.88_0.99	02.67_0.99	02.69_0.99	02.76_0.99	**02.77**_0.99
6	SYL100	7	10.65_0.82	10.24_0.83	10.57_0.83	10.96_0.82	11.67_0.79	**10.87**_0.81
7	TAB50	8	08.30_0.86	08.88_0.84	11.18_0.76	10.53_0.78	07.92_0.86	10.30_0.78
8	**LGP70**	9	01.94_0.99	02.50_0.98	02.38_0.98	01.98_0.99	01.93_0.99	02.10_0.98
9	TCU50	9	14.32_0.85	13.38_0.82	11.55_0.83	11.45_0.80	13.09_0.82	10.78_0.87
10	TCU70	9	11.62_0.80	15.49_0.53	13.29_0.78	13.39_0.69	13.71_0.69	10.72_0.83
11	IWA100	9	10.74_0.53	11.81_0.58	12.51_0.51	13.38_0.51	09.44_0.52	11.45_0.51
12	TAK100	9	09.19_0.92	09.65_0.92	09.98_0.91	09.77_0.92	09.88_0.92	9.67_0.93
13	KJM100	8	09.84_0.83	10.70_0.79	11.03_0.77	11.25_0.76	10.76_0.80	10.76_0.81
14	RRS-2D	7	09.22_0.88	8.88_0.89	09.29_0.88	08.69_0.89	07.53_0.92	08.75_0.89
15	TCU80	8	15.18_0.82	19.63_0.77	15.44_0.82	16.48_0.72	12.19_0.86	**14.55**_0.84
16	TAB80	8	13.72_0.82	17.07_0.65	16.62_0.63	15.52_0.69	14.28_0.78	13.77_0.81
17	TAB90	8	12.75_0.81	12.85_0.78	12.04_0.84	13.63_0.79	12.17_0.82	12.51_0.83
18	**TAB100**	7	01.54_1.00	02.12_0.99	01.73_0.99	01.58_1.00	01.59_1.00	**01.58**_1.00
19	SCT100	8	10.62_0.90	12.09_0.91	12.78_0.90	11.65_0.89	12.02_0.89	10.93_0.91
20	**TAK115**	8	02.70_1.00	03.59_0.99	02.59_0.99	02.84_1.00	02.46_1.00	02.72_1.00
Average error	Train data	36	01.94_1.00	02.63_0.99	02.17_0.99	02.05_1.00	02.00_1.00	02.07_0.99
	Test data	122	10.49_0.83	11.58_0.80	11.19_0.80	11.24_0.79	10.58_0.82	**10.44**_0.83

*Number of full-length samples without data-augmentation.

Table 17: Regularization and testing of the selected LRB architecture.

No.	Table motion	N*	RMSE (kN)_R^2 on full length sequences					
			LRB_MLM	LRB_MLM	LRB_MLM	LRB_MLM	LRB_MLM10	LRB_MLM11
			0% Dropout	10%	20%	30%	40% Dropout	50% Dropout
1	**Sin-1**	4	04.78_0.99	02.64_0.99	02.67_0.99	02.71_0.99	**03.81**_0.99	03.51_0.99
2	VOG75-1	4	10.39_0.94	09.98_0.95	09.83_0.95	08.63_0.96	08.63_0.96	08.20_0.96
3	VOG100	3	10.96_0.96	10.12_0.97	11.04_0.96	09.06_0.97	09.10_0.97	08.54_0.98
4	VOG125	4	09.66_0.98	08.55_0.98	10.65_0.98	09.06_0.98	09.10_0.98	08.54_0.98
5	VOG150	4	07.97_0.99	07.53_0.99	08.30_0.98	07.18_0.99	07.37_0.99	07.78_0.99
6	**VOG175**	4	06.27_0.99	05.69_0.99	05.52_0.99	05.96_0.99	**06.23**_0.99	07.98_0.99
7	DIA80	4	10.16_0.98	09.67_0.98	08.83_0.98	09.66_0.98	08.93_0.99	10.18_0.98
8	**DIA95**	4	06.02_0.99	04.40_0.99	04.27_0.99	04.92_0.99	05.85_0.99	05.58_0.99
9	ELC130	4	10.18_0.94	10.38_0.94	10.33_0.94	10.02_0.95	**09.94**_0.95	10.53_0.95
10	IWA100	4	09.61_0.91	08.62_0.93	09.16_0.92	08.45_0.89	**08.66**_0.89	11.76_0.82
11	**RRS-2D**	4	05.44_0.99	04.79_0.99	03.74_0.99	05.54_0.99	**04.88**_0.99	05.03_0.99
12	RRS-3D	4	05.91_0.99	05.59_0.99	05.23_0.99	06.02_0.99	**05.91**_0.99	06.20_0.99
13	VOG75-2	4	10.78_0.94	10.15_0.95	11.25_0.95	09.92_0.95	09.33_0.96	09.46_0.96
14	Sin-2	4	08.63_0.98	06.41_0.99	08.08_0.99	07.52_0.99	07.88_0.99	07.61_0.99
Average error:	Train data	16	05.63_0.99	04.38_0.99	04.05_0.99	04.78_0.99	05.19_0.99	05.53_0.99
	Test data	39	09.42_0.96	08.70_0.97	09.27_0.96	08.50_0.97	**08.42**_0.97	08.88_0.96

* Number of full-length samples without data-augmentation.

Prediction samples from train and test data are presented in Fig. 41 and 42 respectively. Overall, the TPB_MLM predictions are outstanding for the train data cases and very good for the test ones. One model could predict different and complex structural behaviors of typical TPB devices, in terms of extremum shears and hysteresis loops performed in 1D/2D/3D motions. Many

cases of uplift excursions happened in the realized experimental tests due to overturning moment and/or vertical excitations [55], the TPB_MLM could, not only, learn such a behavior from few training samples (such as TPB-S under RRS-3D presented in Fig. 41), but also predict it under new circumstances (TPB-C under SYL100 presented in Fig. 42). It is worth mentioning that during uplift excursions, conventional analytical models calculating the shear normalized by the instantaneous axial force might fail since the ratio diverges (no tensile resistance). On the contrary, the TPB_MLM showed some limitations in predicting the residual shear for few test data.

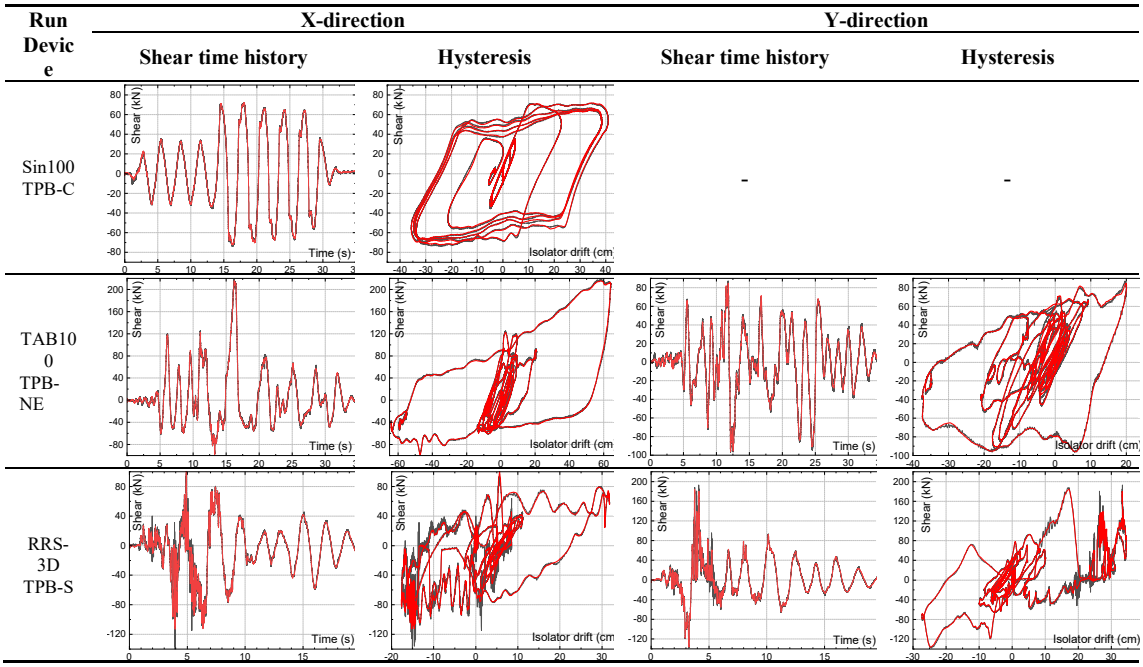

Figure 41: TPB MLM_Train data: Predictions (red) vs. Experiment (black).

Prediction samples from train and test data are presented in Fig. 43-44 respectively. The overall behavior of tested LRB devices could be described by a degrading trilinear analytical model, the conventional smooth bilinear model would over-estimate the energy dissipation capacity. However, some observed local softening and hardening (LRB-W/S under VOG175/RRS-3D presented in Fig. 43-44), strength degradation (LRB-S under Sin-1 presented in Fig. 43), and pinching effects (all cases) would be difficult to combine together in one single analytical model. The same LRB_MLM could capture all aforementioned hysteresis features with a very good accuracy. It performed also very well for the longest table motion duration used in this study of 180 seconds (LRB-N under IWA100 presented in Fig. 44), proving that developed GRU models could behave well even for long-term temporal dependency problems. It is worth mentioning that the sudden shear drops observed in the LRB-E under RRS-2D (Fig. 43), are because of some bolt slippage that occurred at the bottom connecting steel plate [49]; unsurprisingly, the LRB_MLM did not capture these spikes unrelated to the isolator itself.

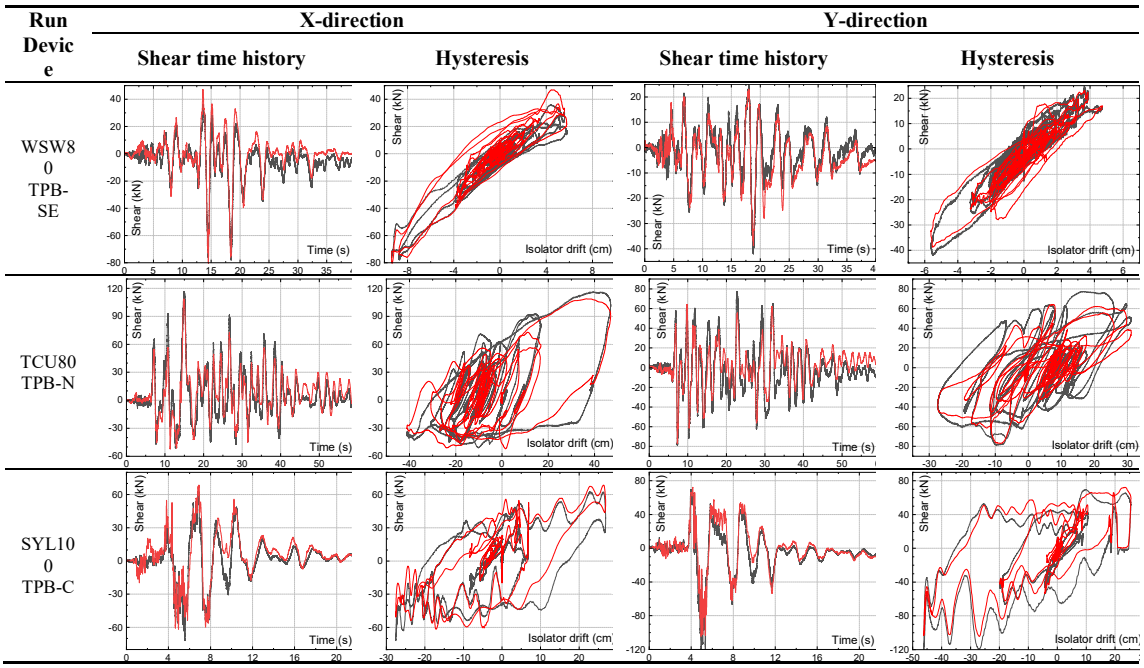

Figure 42: TPB MLM_Test data: Predictions (red) vs. Experiment (black).

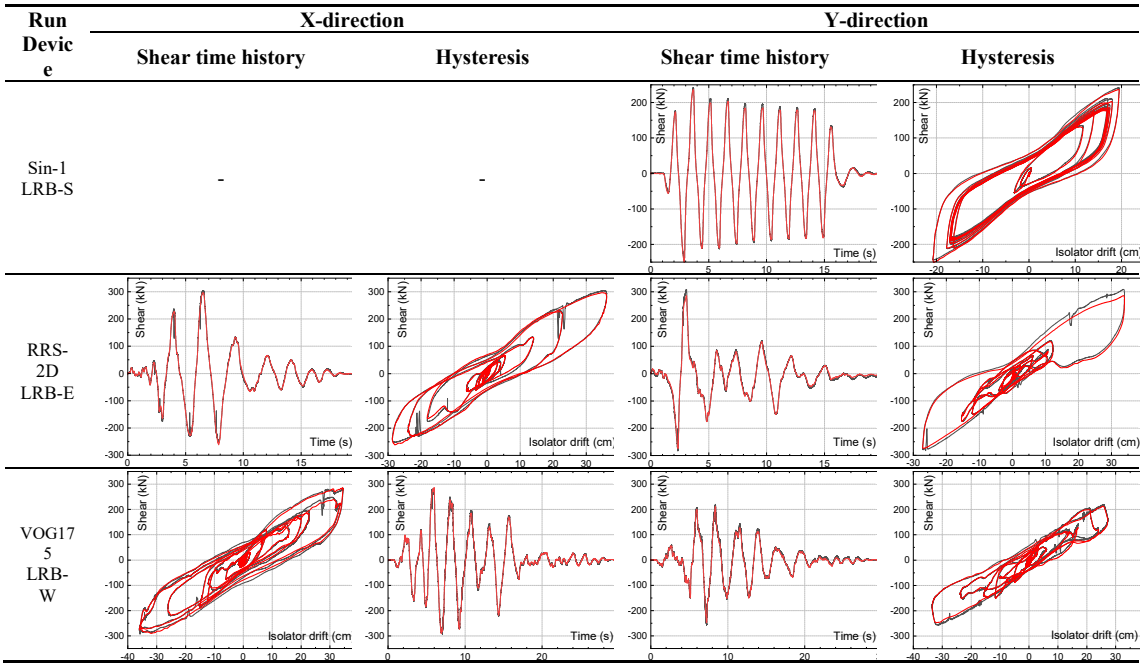

Figure 43: LRB MLM_Train data: Predictions (red) vs. Experiment (black).

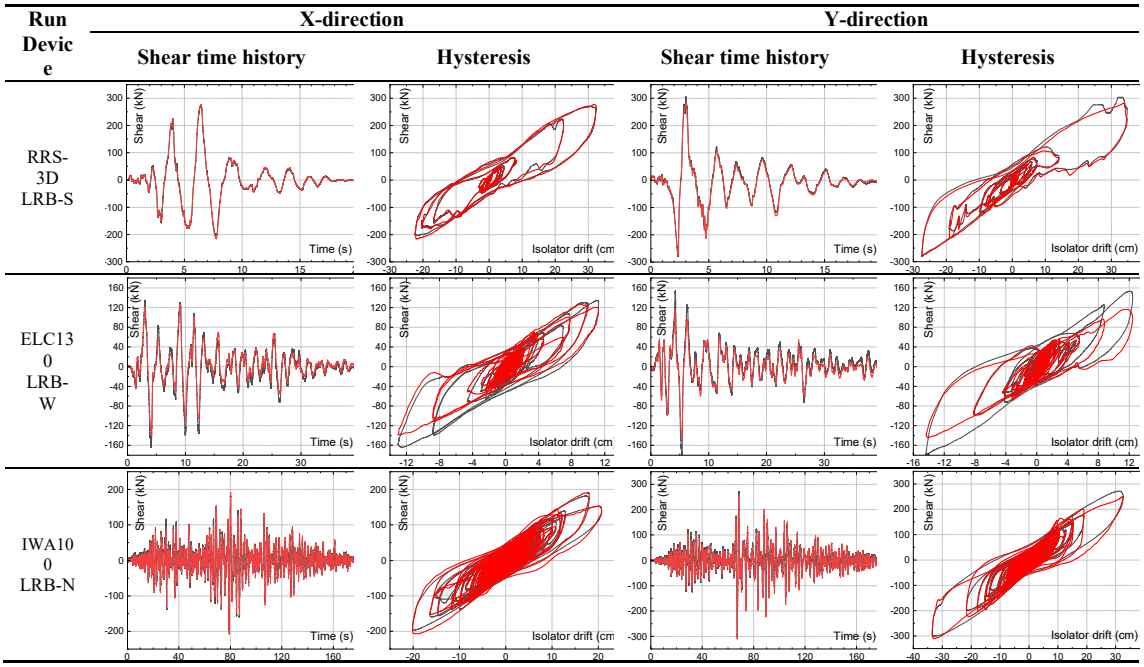

Figure 44: LRB MLM_Test data: Predictions (red) vs. Experiment (black).

3.7.6. Computation time

A summary of elaborated TPB/LRB MLMs is presented in Table 18. These RNN models are accurate since their RMSEs on the substantial test data are acceptable in Structural Engineering (10.44/8.42 kN), and the R^2 values of 0.83/0.97 highlight the strong correlation between experimental and predicted data. Furthermore, models architectures were optimized to minimize the number of trainable parameters (83,412/33,602); thus, the training time (20h52/9h16). A MLM accuracy and simplicity are crucial for a successful implementation in the hybrid analysis [25].

Table 18: Summary of final TPB and LRB MLMs.

	Input	Output	Architecture	Training		Average RMSE (kN)-R^2	
				Sampl	Time	Train	Test data
TPB	X-Y Displacement histories Axial force history	X-Y Shear histories	95 GRU cells Dropout: 50% 95 GRU cells 2 Dense cells	1080	20h52	02.07_0.99 (36 samples)	10.44_0.83 (122 samples)
LRB	X-Y Displacement histories	X-Y Shear histories	60 GRU cells Dropout: 40% 60 GRU cells 2 Dense cells	480	09h16	05.19_0.99 (16 samples)	08.42_0.97 (39 samples)

3.8.Surrogate models for model isolation systems

3.8.1. Artificial neural network architecture

The architecture of a pure RNN is described mainly by the depth (number of recurrent layers), the width (number of recurrent cells in each layer), and the type of the recurrent cell (or

unit). It is very common to add a fully connected Dense layer for the output layer, as presented in the original 1997 LSTM paper [60]. More developed configurations may be considered depending on the problem treated [54]. Since the objective is to predict the shear time history from the displacement time history, a sequence-to-sequence model is adopted. Once trained and tested, the MLM would be implemented to perform hybrid seismic analyses by predicting the shear force at each integration time step; thus, its architecture should be as small as possible to optimize the computation time. Deep RNNs may not systematically increase the performance of the network [68], as opposed to MLPs and CNNs and as long as overfitting-type problems are treated. When unfolded through time, a shallow RNN is actually a deep network. Therefore, a stacked RNN of only three layers is adopted herein: first recurrent layer as an input layer, second recurrent layer as a hidden layer, and a one-unit Dense layer as an output layer. The network depth being fixed, random searches are performed to optimize the type of the recurrent cell (first screening) and the network width (second screening).

LSTM [60] and GRU [61] are the most common and widely used recurrent cells (or units) since they outperform traditional RNN cells [64]. They are gated recurrent units capable of learning long-term temporal dependencies, which is important in this study to predict the nonlinear shear force from the displacement time history. The GRU is a recent variant of the LSTM with less trainable parameters. However, the performance of one relative to the other is still an open research field [63]. Both LSTM and GRU cells are used and compared in this study. Box and Whisker plots are visualized to describe the statistical distribution of models' final performances. For each RNN architecture, scores (MSE on validation data after 500 training epochs) are dot marked next to the boxplot, their mean value by a cross mark, and the median value by a horizontal line within the Inter Quartile Range (IQR). Fig. 45 shows the performance of LSTM (red color) and GRU (blue color) models, all with the same depth but different widths. The horizontal axis represents the number of RNN cells per each of the two recurrent layers. A 5-units step is adopted from 10 up to 100 units. For each architecture, 10 independent runs are performed, leading to 10 different evaluations, which attest to the aleatory uncertainty of the training process. MSEs of both LSTM and GRU models are decreasing uniformly up to 35-cells width. From 35 to 100-cells width, the performance of GRU models is more stable compared to LSTM models, which have more outliers and larger IQRs. Therefore, the GRU cell slightly outperforms the LSTM cell for the problem treated in this study. The width range between 60- and 80-GRU cells are selected for the second screening since there is no major gain in accuracy and precision for larger widths, and the minimization of network architecture is a crucial criterion for an efficient implementation of MLMs in hybrid seismic analyses.

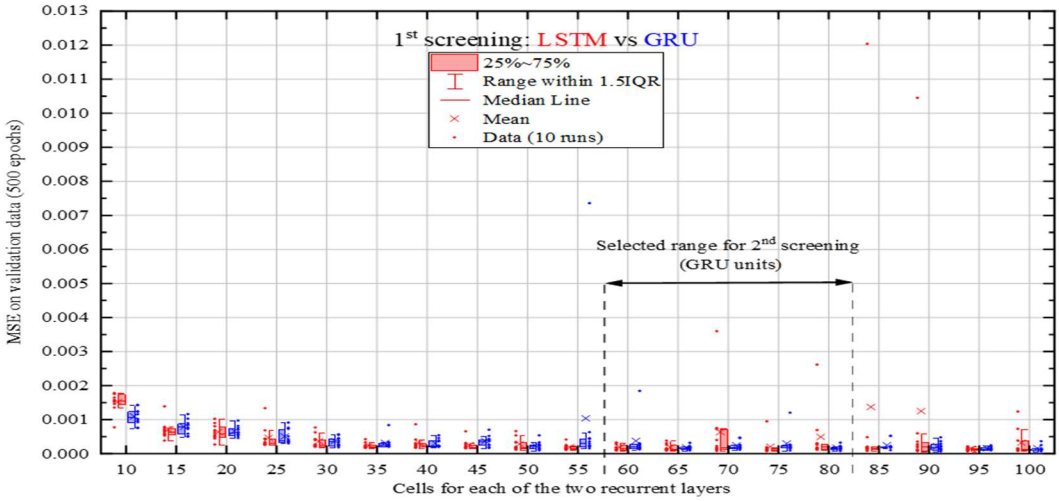

Figure 45: Isolation layer-MLM1: 1st Screening for random search of architecture.

3.8.2. Models reliability

GRU architectures within the previously selected width range are trained and evaluated 20 independent times again, as shown in Fig. 46(A). The global performance is still stable as all MSE means and median values are less than 3×10^{-4}, and data are less scattered (tighter IQRs). Since all these models perform similarly (in terms of mean value, median value, and IQR), the one with the fewer GRU units is selected to minimize the computation time when implemented for hybrid seismic analysis. The reliability of the selected 60-GRU architecture is tested further to ensure its robustness, as shown in Fig. 46(B). All MSE means and median values are again less than 3×10^{-4}, although few outliers are included within the data. It is worth mentioning that the cases of 10- and 20-runs of the selected 60-GRU architecture are independent of those performed at first and second screenings. The difference in results is due to the randomness of the training process.

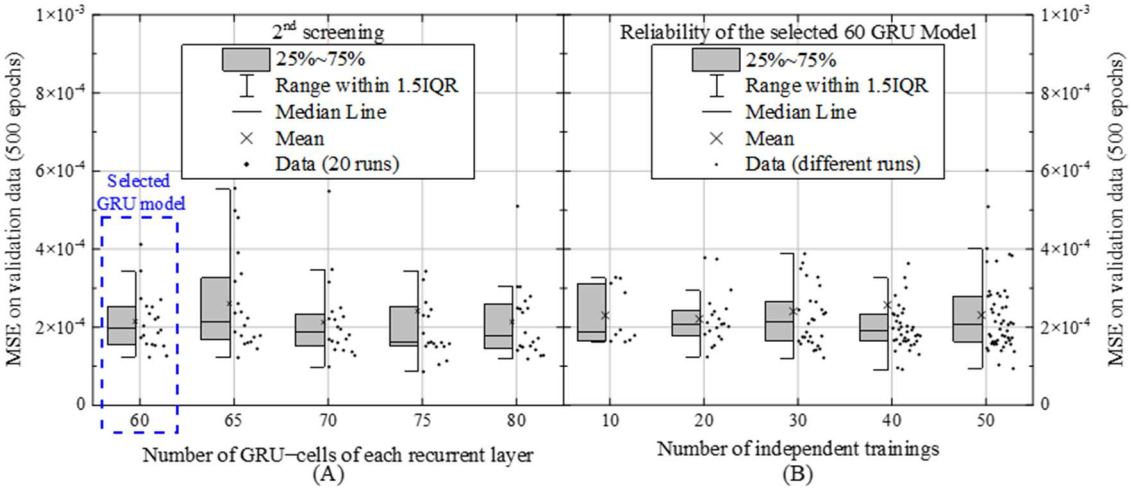

Figure 46: Isolation layer-MLM1: (A) 2nd Screening and (B) reliability of GRU model.

3.8.3. Sensitivity analysis to hyperparameters

The optimizer, the number of epochs, and the batch size are commonly recognized as the most influencing hyperparameters on the performance (accuracy and computation time) of neural networks [54]. More specifically, the learning rate of the optimizer (here, Adam optimizer [69]) that scales the magnitude of the network weights update is a key hyperparameter [70]. The loss may be a highly non-convex function [71]. Very small learning rates delay the network learning and/or may stick the loss function to a local minimum. Very high learning rates make the learning very noisy with a risk of divergence. The number of epochs combined with the batch size defines how often the weights are updated, which influences both the learning accuracy and the computation time. For a fixed number of 500 epochs, the sensitivity of the selected RNN to commonly used values of learning rate and batch size is investigated. As shown in Fig. 47(A), high learning rates (0.005~0.01) and frequencies of weights updates (batch size of 16 and 32) lead to a divergence of the loss function, and a small learning rate (0.0001) delays the learning and especially for small frequencies of weights updates (batch size of 64 and 128). A good balance is obtained for intermediate (diagonal) values. The learning rate has almost no influence on the training duration, which is inversely proportional to the batch size, as shown in Fig. 47(B). Since the RNN architecture was minimized at Stage 3 and GRU cells have less trainable parameters than LSTM cells, the training time is less than one hour in all cases. Therefore, the values of learning rate (0.001) and batch size (32) used previously at Stage 3 are kept unchanged.

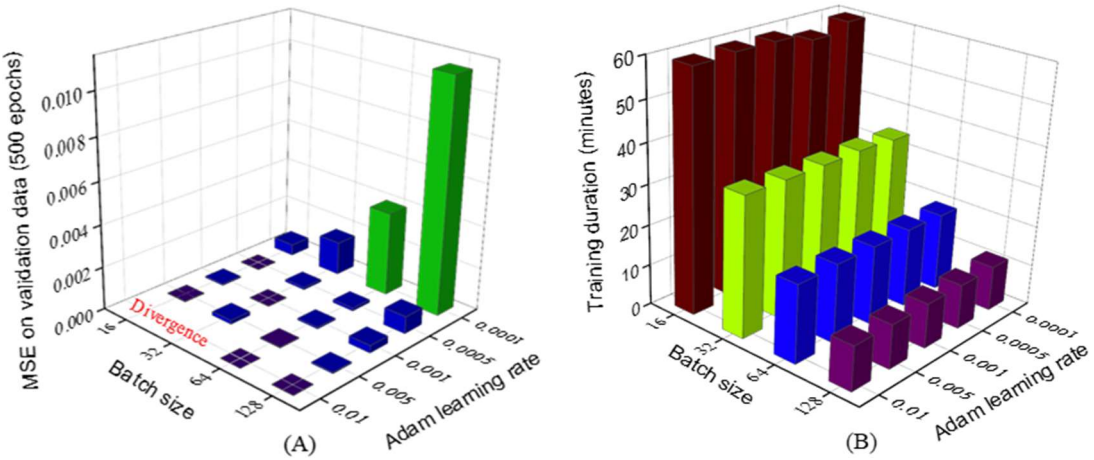

Figure 47: Sensitivity analysis to hyperparameters: (A) MSE; and (B) Training time.

3.8.4. Diagnosis of learning behavior

The selected GRU architecture has shown satisfactory final performance up to 500 epochs. In order to decide the number of training epochs to train the final model, the learning behavior has been diagnosed throughout the first 1500 epochs for five independent runs (5 colors in Fig. 48). The MSE on training data is represented by solid lines and dashed lines for validation

data. The most important phase of learning is established in the first 125 epochs (Range 1). Both validation and training losses decrease and stabilize jointly for the five independent runs. No exaggerated underfitting or overfitting behavior is observed after 125 training epochs. The mean loss of both training and validation data decreases below 5×10^{-5} after only 1000 epochs and keeps converging asymptotically to a zero value (Range 2). Similar nonlinear dynamic response prediction problems treated in recent studies using recurrent networks required 10,000 [72] and 50,000 [4] epochs to reach losses of the same order and with networks having about 130,000 [4] trainable parameters (here, only 33,361 for the selected 60 GRU architecture). MLM1 is trained up to 1500 epochs, and its MSE on validation data is 1.69×10^{-5}. This outstanding performance is due to the quality/size of training data and to the network optimization process.

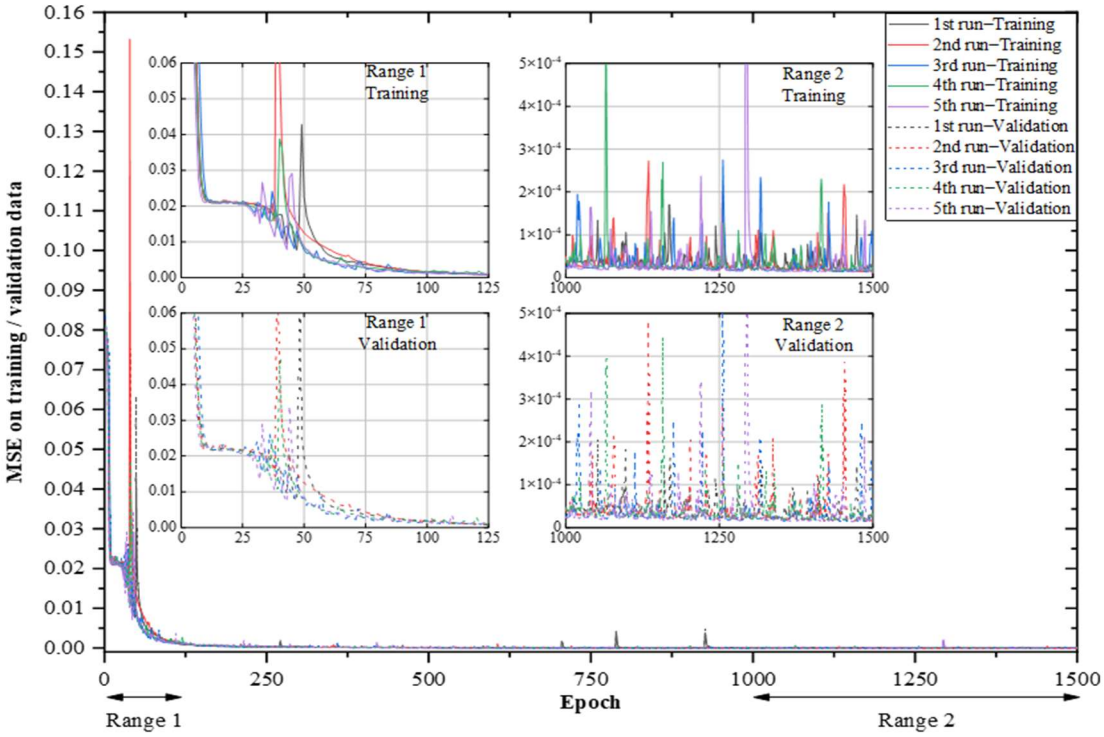

Figure 48: Isolation layer-MLM1: Learning behavior.

MLM2 and MLM3 are designed for a sequence prediction problem of the same nature as MLM1. The only differences are the properties of the isolation layers they simulate (Table 10). Therefore, the same architecture and hyperparameters adopted for MLM1 were used for their training activities on datasets of the same size but with different contents. The MLM2 (MLM3 respectively) MSE on validation data is 6.51×10^{-6} (1.24×10^{-5} respectively).

3.8.5. Testing of isolation layer MLMs

Three test datasets of 50 samples each were derived from GMs 3~5 (Stages 1 and 2). In order to test developed MLMs, their MSEs on these new unseen data are evaluated. As shown in

Table 19, all MSEs are in the order of 10^{-4}, which are greater than those of training data (~10−5), but it is still a very good performance knowing that test data were intentionally generated from GMs with different properties than GM2 used for training (see Table 13 and Fig. 30).

Table 19: Isolation layers-MLMs: MSEs on test datasets.

	Test Dataset 3 (GM3: Taft 1952 EW)	**Test Dataset 4 (GM4: Tohoku 1978 NS)**	**Test Dataset 5 (GM5: El Centro 1940 NS)**
MLM1	2.73×10^{-4}	6.04×10^{-4}	3.84×10^{-4}
MLM2	5.04×10^{-4}	7.04×10^{-4}	4.97×10^{-4}
MLM3	6.75×10^{-4}	9.72×10^{-4}	6.63×10^{-4}

To illustrate the accuracy of developed models on real scale data, shear time history predictions of a few random samples are unscaled, then combined with their respective displacement time histories to draw the corresponding nonlinear cyclic hysteresis loops. Fig. 49 to 51 show respectively the resulting curves compared with reference ones of NTHAs. It is worth mentioning that for each sample case, both MLM and NTHA have the same displacement time history; thus, RMSE is provided only for the shear sequence. The predicted hystereses fit very well reference curves, and all RMSEs are in the order of tens of kN, which is widely accepted in earthquake engineering.

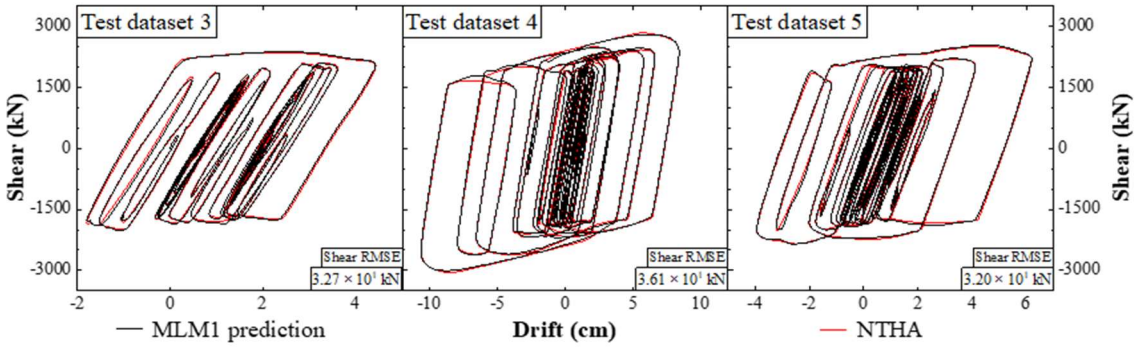

Figure 49: MLM1: Prediction (black) vs reference (red) of a random sample.

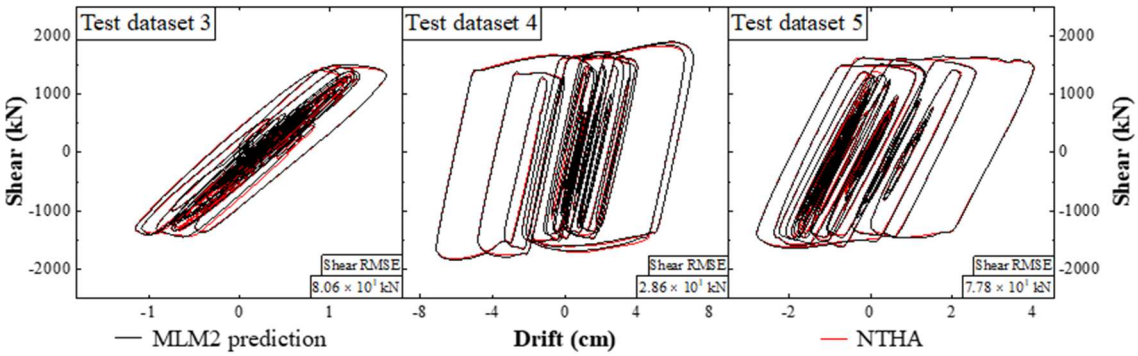

Figure 50: MLM2: Prediction (black) vs reference (red) of a random sample.

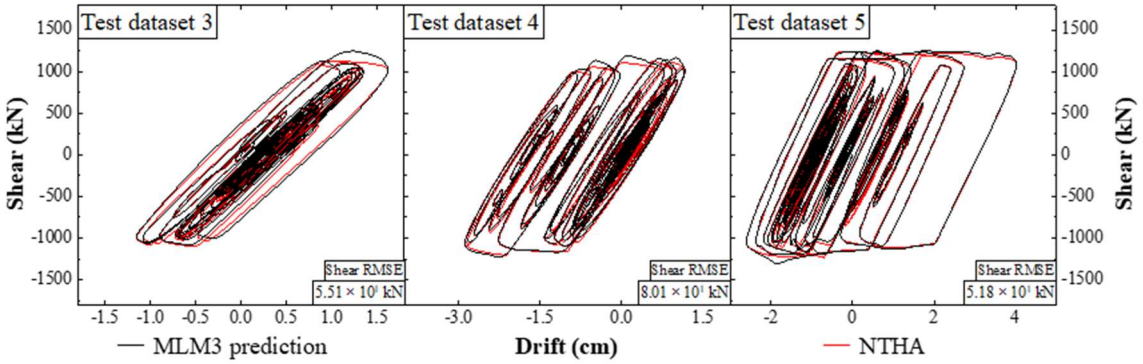

Figure 51: MLM3: Prediction (black) vs reference (red) of a random sample.

3.8.6. Computation time

Table 20 shows the consumed computation time for each step of Stages 3 and 4. GRU models are about 27% faster than LSTM models since they were initially designed with less trainable parameters. The third stage is the most time-consuming in the proposed framework since 630 independent training acts were performed for a cumulative computation time of almost 3 days. The sequence length is the number of integration time-steps used for NTHAs, which is equal to the GM duration divided by the modified time-step of its original record (here, 0.02/5 = 0.004 s). The time subdivision by five is commonly used for an accurate nonlinear analysis. Considering the randomness of the training process of ANNs, the skill of a model should never be evaluated by a single run. The number of repetitive training acts is limited only by the available time and the computation resources.

Table 20: Isolation layer: Computation time for developing the MLMs.

Training	Sequence Length	Epochs	Batch Size	Number of Training	Time (h)
1st screening	1251	500	32	LSTM: 19 × 10 = 190 GRU: 19 × 10 = 190	23.93 18.87
2nd screening	1251	500	32	5 × 20 = 100	09.82
Model reliability	1251	500	32	10 + 20 + 30 + 40 + 50 = 150	14.80
Sensitivity analysis	3751	500	16~128	20	10.27
MLM1	3751	1500	32	5	08.49
MLM2	3751	1500	32	1	01.65
MLM3	3751	1500	32	1	01.66

Chapter 4: HYBRID SEISMIC ANALYSIS OF BUILDING STRUCTURES

4.1.Introduction

The conventional method to simulate the time history response of a building model subjected to dynamic loadings, such as earthquake ground motion and wind load, is based on the principle of mechanics. Newton's laws of motion are the essence behind the establishment of the equilibrium equations. When considering the complexity of the original formulation and the development of numerical computation resources in the second half of the 20th century, the resulting second-order differential equations had been reformulated and numerically solved through discretization in space and time using the Finite Element Method (FEM) and time integration algorithms, respectively. Many analytical models to simulate the nonlinear behavior of common structural members, such as reinforced concrete (RC) structural components, had already been formulated and validated by experimental results [73]. The combination of all these modules makes it possible to compute a building response by performing NTHA. Many assumptions and/or simplifications are considered, whether in the original physics laws, the FEM, or the hysteresis models of structural components. Time integration methods also generate numerical errors, and their stability may be compromised [74,75]. Despite all these inevitable limitations, the NTHA remains the most accurate and reliable mechanics-based method to evaluate the seismic performance of a structural model. This know-how must be the reference for response prediction problems (RPPs) of building structures.

For RPPs, deep learning (DL) models such as multilayer perceptrons (MLPs), convolutional neural networks (CNNs), and RNNs are becoming more attractive since no need to identify features within input data are required, and more sophisticated DL algorithms are being constantly developed [76]. Even though RNNs were initially designed for time series forecasting problems, only very few of their applications are counted in earthquake engineering. Zhan et al. [18] predicted the nonlinear inter-story drifts of three building structures (five degrees-of-freedom system, six-story instrumented RC building, and three-story steel building model) using LSTM [60] recurrent networks. In general, very high prediction accuracy was observed for a close-to-linear structural response, and it decreases with nonlinearities. The same research team had improved the prediction accuracy and robustness of the previously developed LSTM models by encoding some laws of physics in the network architecture and embedding them in the overall loss function [72]. Eshkevari et al. [77] developed a physics-based recurrent cell (DynNet) that predicts the full state space (acceleration, velocity, displacement, and internal forces of MDOF, given a ground motion. Nonlinear responses of two 4DOF systems with different nonlinearity

types (elastoplastic and nonlinear elastic stiffnesses) were quite successfully predicted; thus, concluding that the performance of the DynNet in capturing the nonlinear response is promising. All these implementations of RNNs for RPPs highlighted some drop of accuracy in predicting large nonlinearities, and their respective models remain limited to predict limited response quantities of the studied structures.

In order to address many of the aforementioned limitations, the hybrid seismic analysis proposed in this Chapter combines the advantages of both NTHA (mechanics-based method) and MLMs (data-driven method) as shown in Fig. 52. The term hybrid is related to the time integration algorithm of the NTHA, not to the input data nor to the model architecture. Some existing or newly developed materials, structural components, or devices may have an excessively complicated analytical model and/or a still not-exhaustive understanding of their true behavior among researchers and practitioner communities. Instead of adopting simplified analytical models based on many assumptions which introduce a modeling error, an RNN trained by available experimental data can capture the true behavior of the target component or group of components, then make predictions on new unseen data at each time-step of the hybrid seismic analysis. Therefore, this study presents the novelty of implementing DL models into the numerical time-integration algorithm, targeting only structural components of interest. The proposed hybrid analysis is not limited to a specific building structure since the MLM can be saved and reused in any new building model containing the same target component(s), it can compute the full dynamic response, and it aims to increase further the accuracy of conventional NTHAs. Both synthetic and experimental data are used in this Chapter to check the efficiency of the method.

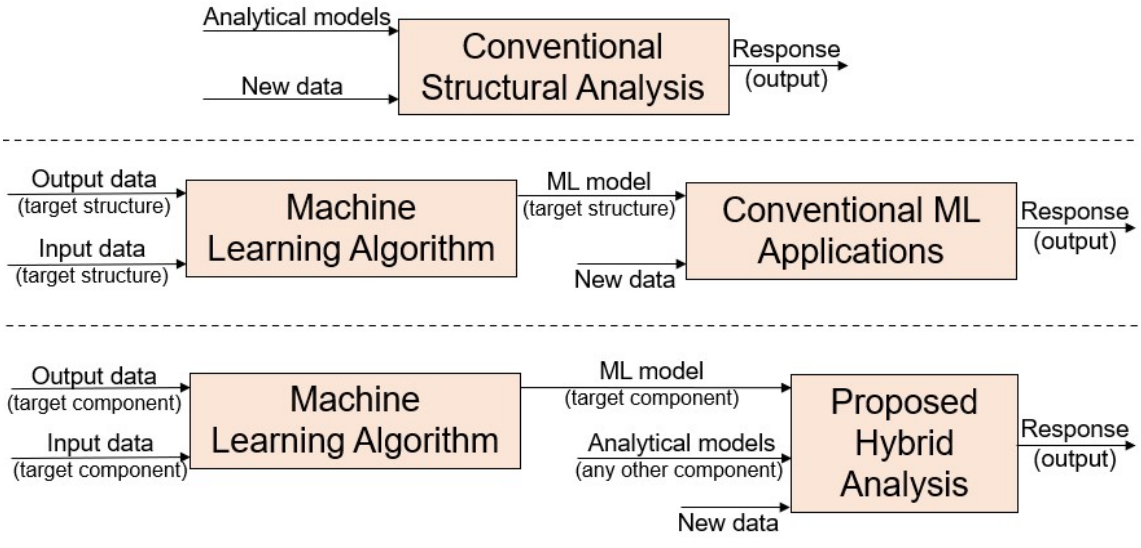

Figure 52: Principle of the proposed hybrid seismic analysis.

4.2.Principle of the proposed hybrid seismic analysis

4.2.1. Background

The proposed hybrid analysis is inspired by the hybrid simulation developed by Nakashima et al. [78,79] for real-time pseudo-dynamic testing. The target structure is divided into a numerical model and a physically tested model. The latter one may be a structural component or a group of components as a sub-structure. It is an efficient and most economical alternative to testing an entire structure. The control and the limitation of the numerical error require the choice of an appropriate numerical integration method [80]. Nakashima et al. [81] proposed a mixed implicit-explicit direct integration method that incorporates the physically measured restoring force into the numerically solved second order equation of motion. It is a predictor-one-corrector displacement method based on the operator splitting technique proposed by Hughes et al. [82] and the implicit Newmark-β method [83]. It was proven that this method (referred to as the OpS method in the remainder of this dissertation) is unconditionally stable for pseudo-dynamic testing of structures with softening-type nonlinearities.

4.2.2. Proposed deep learning-based integration method

Instead of measuring the restoring force developed in the tested physical model, the proposed hybrid seismic analysis evaluates it using a MLM, previously trained to simulate the hysteretic behavior of the target component or group of components. The commonly used OpS method is selected as a suitable numerical integration algorithm for NTHA. Fig. 53 summarizes the hybrid integration loop. Assuming a building structure and an input ground motion, the predictor displacement vector is first evaluated at the current time step following the algorithm of the OpS method. Restoring forces of structural components with already mastered hysteresis behavior, such as reinforced concrete or steel columns and beams, are evaluated using available validated analytical models. Some existing or newly developed materials, components, or devices may have an excessively complicated analytical model and/or still not-exhaustive understanding of their true behavior among researchers and practitioner communities. Instead of adopting simplified analytical models based on many assumptions, a MLM previously trained by available experimental data can capture the true behavior of the target component or group of components and then be used to make predictions within the time integration algorithm. It would predict the component restoring force at the next time step, based on the displacement time history and the current predictor displacement. Then, the full seismic response at the next time step is computed as performed in the OpS method. The same process is repeated till the end of the analysis.

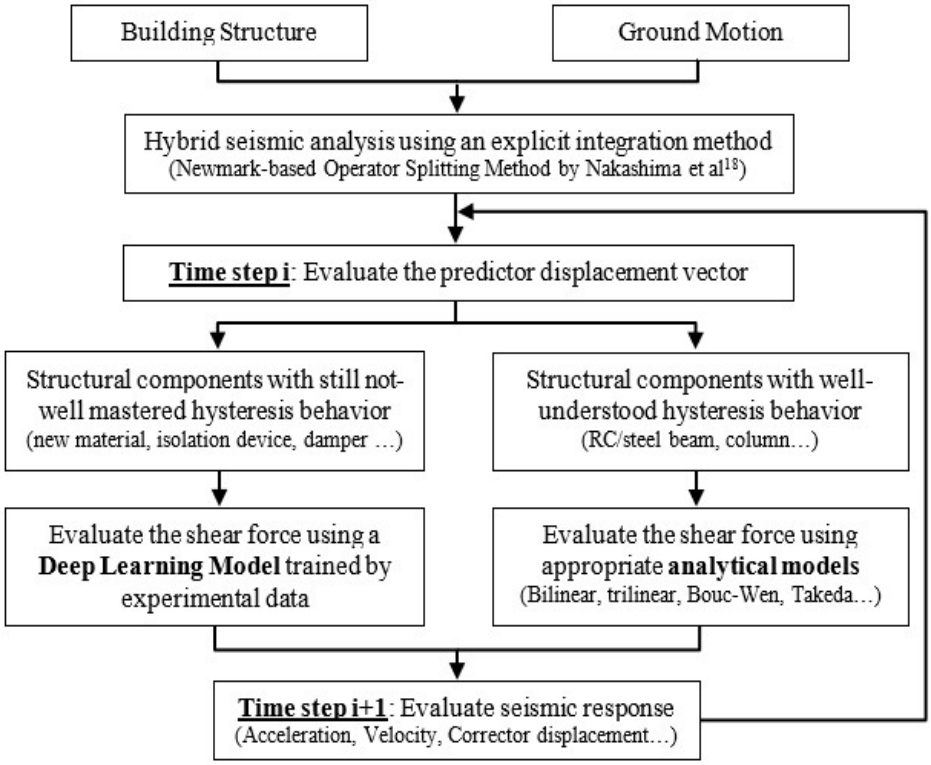

Figure 53: Principle of the deep learning-based integration method.

The concept of the proposed hybrid seismic analysis is general to any structure and relies on developing MLMs beforehand. The development of MLMs from experimental data is nonrepetitive since it can be saved and reused in any new structure containing the same target components. For instance, the same isolation device can be used in different buildings but with different configurations and numbers. New experimental data of the same nature may be used to update the MLM, though.

Python scripts were made to process the data and to perform conventional and hybrid NTHAs using the TensorFlow machine learning library under Python 3.6. All runs are performed with 16 Intel® Xeon® W-2245 CPUs. Source codes are provided in Appendices A and B.

4.3.Hybrid seismic analysis of lumped-mass building models

4.3.1. Isolated building models

Three base-isolated buildings of 5, 10, and 15 stories are considered in this study. A Lumped Mass Model (LMM) is adopted for the superstructure, which behaves linearly. The isolation layer is formed by NRB, LRB, and Oil Damper (Oil), as shown previously in Fig. 25. The combination of both NRB and LRB devices is assumed to perform a bilinear hysteresis behavior. The force developed in the Oil Damper device is assumed to depend only on the relative velocity of its edges. The three buildings were designed according to Japanese engineering

practice [53] and modeled using the software STERA_3D [12]. Tables 21 and 22 provide all the necessary properties to reproduce the same models. More design information and even the STERA_3D may be downloaded online [84]. MLMs developed in Chapter III are used herein to perform the hybrid seismic analyses of studied isolated buildings.

Table 21: Lumped-mass model properties of model building structures.

	Building 1		**Building 2**		**Building 3**	
Ref.	**MB1**		**MB2**		**MB3**	
Period	**$T_{n,1}$ = 0.5 (s)**		**$T_{n,2}$ = 1.0 (s)**		**$T_{n,3}$ = 1.5 (s)**	
Story Level	**Stiffness (kN/mm)**	**Weight (kN)**	**Stiffness (kN/mm)**	**Weight (kN)**	**Stiffness (kN/mm)**	**Weight (kN)**
15th	-	-	-	-	80	3000
14th	-	-	-	-	156	3000
13th	-	-	-	-	225	3000
12th	-		-	-	290	3000
11th	-	-	-	-	349	3000
10th	-	-	121	3000	402	3000
9th	-	-	229	3000	451	3000
8th	-	-	326	3000	494	3000
7th	-	-	410	3000	531	3000
6th	-	-	483	3000	563	3000
5th	241	3000	543	3000	590	3000
4th	435	3000	592	3000	612	3000
3rd	579	3000	628	3000	628	3000
2nd	676	3000	652	3000	639	3000
1st	724	3000	664	3000	644	3000

Table 22: Isolation level properties of model building structures.

Isolation Level			**Building 1**	**Building 2**	**Building 3**
Effective Period		**(s)**	**$T_{eff,1}$ = 2.5**	**$T_{eff,2}$ = 4.0**	**$T_{eff,3}$ = 6.0**
Base Weight		**(kN)**	**4500**	**4500**	**4500**
Oil Damper	C_1	(kN.s/mm)	2.194	1.617	1.237
	C_2/C_1		0.067	0.067	0.067
	V_r	(mm/s)	320	320	320
LRB+NRB	K_1	(kN/mm)	175.5	129.4	99
	K_2/K_1		0.046	0.042	0.031
	F_y	(kN)	1755	1294	990
ML model designation			MLM1	MLM2	MLM3

4.3.2. Input ground motions

GMs used to perform NTHAs are the same as those presented previously in Table 13 and their acceleration response spectra were presented in Fig. 30. Fundamental horizontal periods of the building's superstructures ($T_{n,1}$, $T_{n,2}$, and $T_{n,3}$) and the effective periods of their respective isolation layers ($T_{eff,1}$, $T_{eff,2}$, and $T_{eff,3}$) were marked with vertical dashed lines, covering the common period range of based isolated structures.

4.3.3. Isolation system response

Seismic analyses of Building 1, 2, and 3 subjected to GMs 2, 3, 4, and 5 are performed using both the conventional NTHA (OpS method) taking as a reference and the new proposed hybrid analysis (MLM1~3 simulating the isolation layer: NRB, LRB, and Oil Damper). The superstructure response is evaluated by its analytical models in both cases. The isolation system response, the peak story deformation, and the peak story acceleration obtained by both analyses are presented hereafter for comparison. Since both drift and shear are computed at each time-step, the drift RMSE is also evaluated as follows,

$$Drift\ RMSE\ (cm) = \sqrt{\frac{\sum_{time}\left(drift_{OpS,i} - drift_{Hybrid,i}\right)^2}{N_{time\ steps}}} \tag{24}$$

The isolation system response of Building 1 is presented in Fig. 54. Hysteresis loops of the isolation layer are not perfectly bilinear because of the effect of the Oil Damper. Hybrid seismic analyses results fit very well reference curves for all the GMs considered in this study, despite the long nonlinearities (drift up to 13.5 cm for the case of GM2). The maximum drift RMSE (respectively shear RMSE) is 0.098 cm for GM5 (respectively 32.4 kN for GM4). All RMSEs are of the same order and remain within an acceptable range. The maximum shear RMSE is 27.1 kN (GM4, first floor). Similar remarks may be formulated for isolation system response of Buildings 2 and 3 presented in Fig. 55 and 56 respectively.

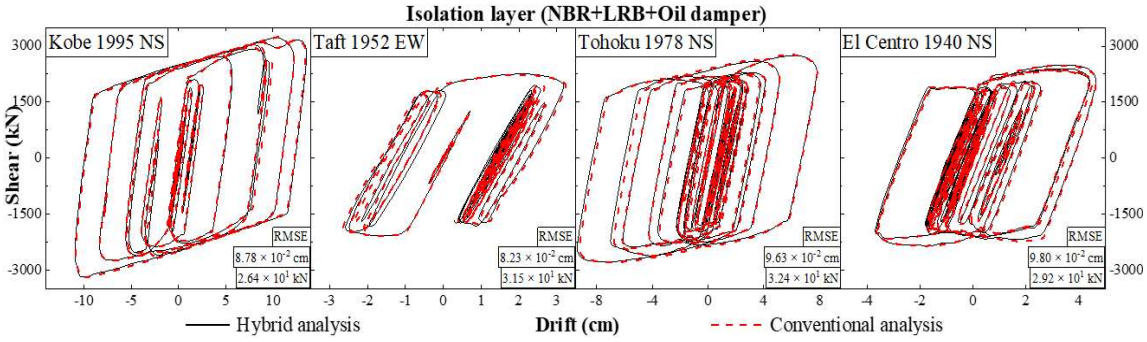

Figure 54: MB1 isolation layer hystereses: Hybrid vs. Conventional analyses.

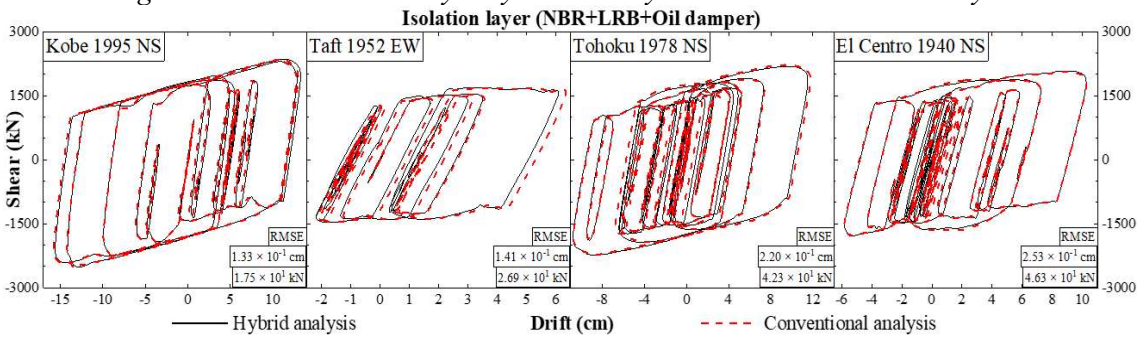

Figure 55: MB2 isolation layer hystereses: Hybrid vs. Conventional analyses.

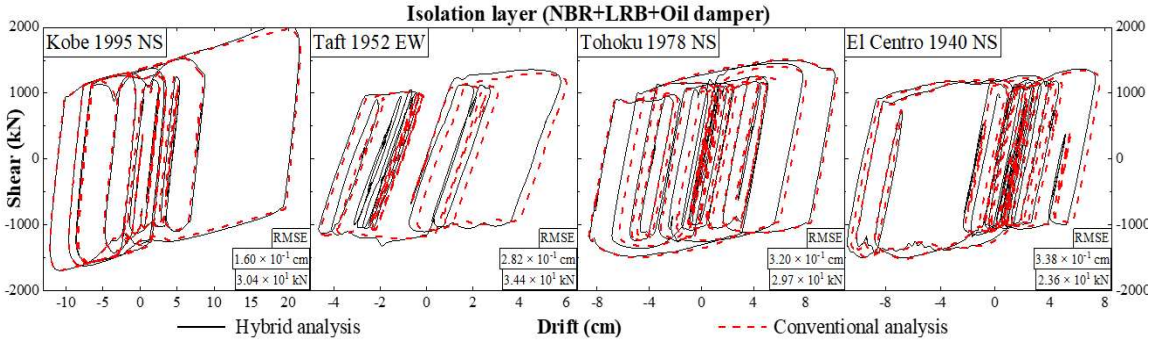

Figure 56: MB3 isolation layer hystereses: Hybrid vs. Conventional analyses.

4.3.4. Peak story deformations

Peak deformation at geometric center of all floors of Building 1 are presented in Fig. 57 for each GM (4 colors) and each seismic analysis (solid lines for hybrid analysis and dashed lines for conventional one). The deformation is unsurprisingly concentrated in the isolation and layer superstructure deforms linearly. The height wise distribution of peak deformations matches with the flexural deformation of the fundamental mode of the fixed base configuration. Evaluations by both analyses fit very well. The maximum drift RMSE is 0.00528 cm (GM 2, roof). Similar remarks may be formulated for Buildings 2 and 3 presented in Fig. 58 and 59 respectively.

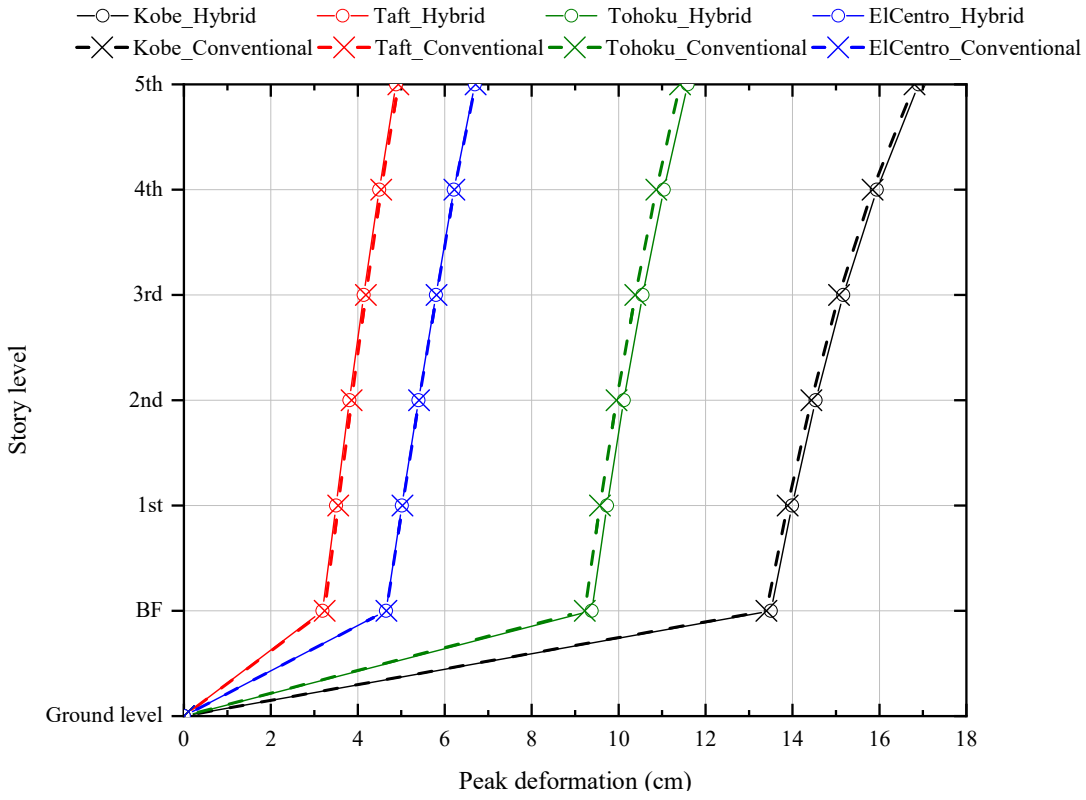

Figure 57: Peak floor deformations of MB1: Hybrid vs. Conventional analyses.

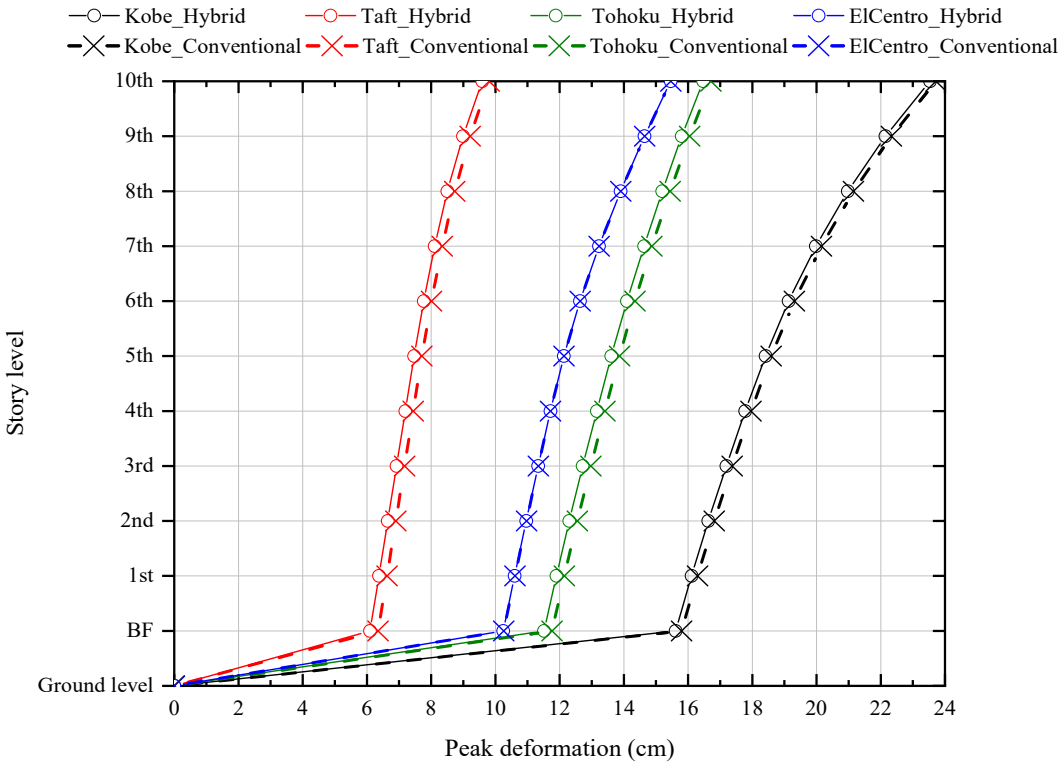

Figure 58: Peak floor deformations of MB2: Hybrid vs. Conventional analyses.

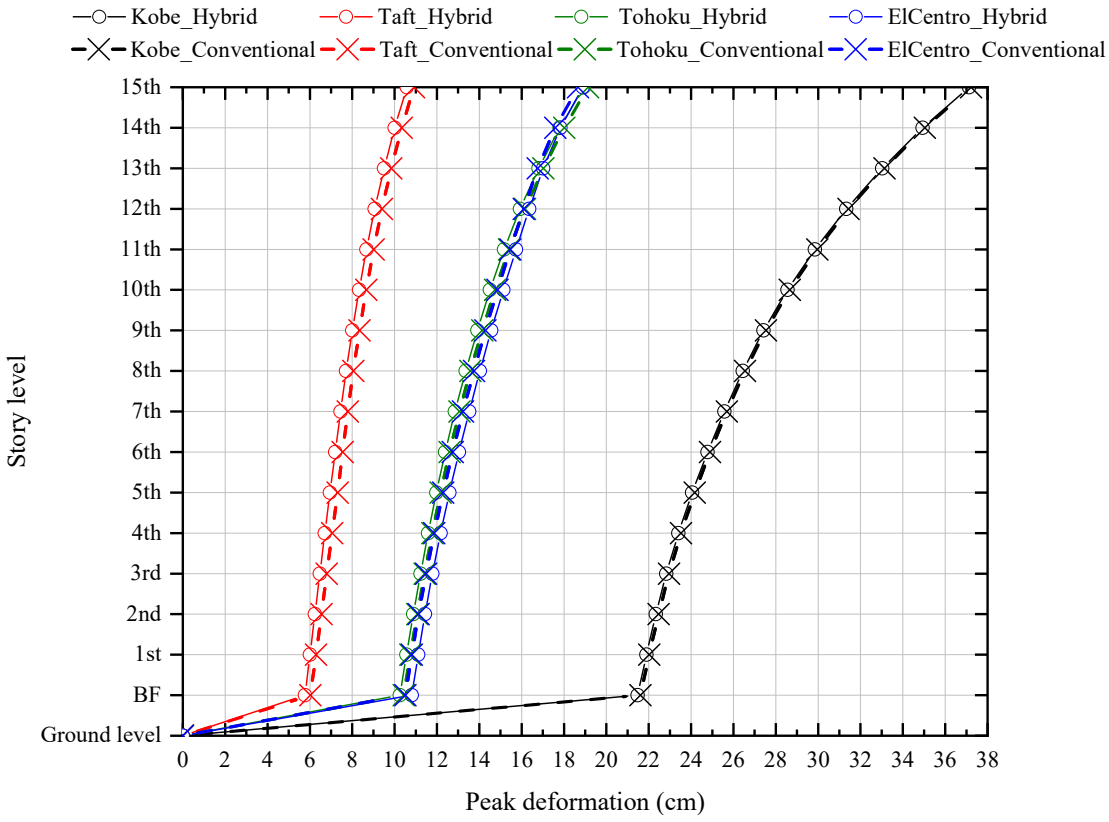

Figure 59: Peak floor deformations of MB3: Hybrid vs. Conventional analyses.

4.3.5. Peak story accelerations

Peak acceleration at geometric center of all floors of Building 1 are presented in Fig. 60 for each GM (4 colors) and each seismic analysis (solid lines for hybrid analysis and dashed lines for conventional one). Acceleration transmissibility from the ground level exhibits a significant drop due to the isolation layer, followed by a relatively constant distribution of peak floor accelerations throughout the height until a quite moderate increase at the top levels. Peak floor accelerations are lower than corresponding PGAs in most of cases. Evaluations by both analyses fit very well. Similar remarks may be formulated for Buildings 2 and 3 presented in Fig. 61 and 62 respectively.

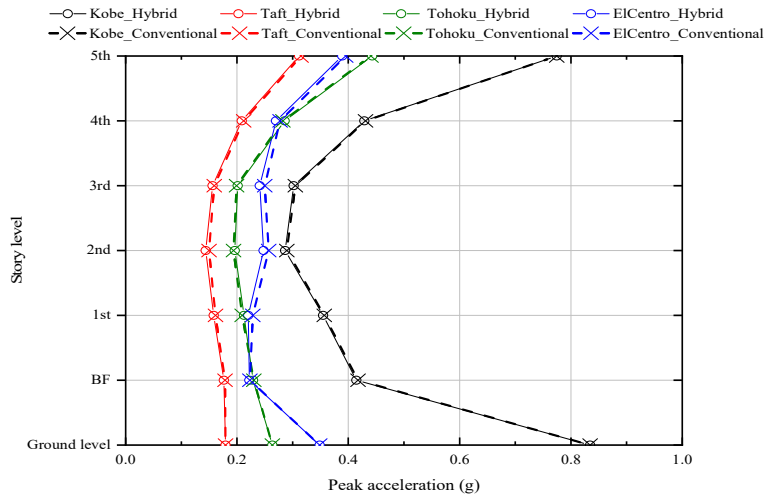

Figure 60: Peak floor accelerations of MB1: Hybrid vs. Conventional analyses.

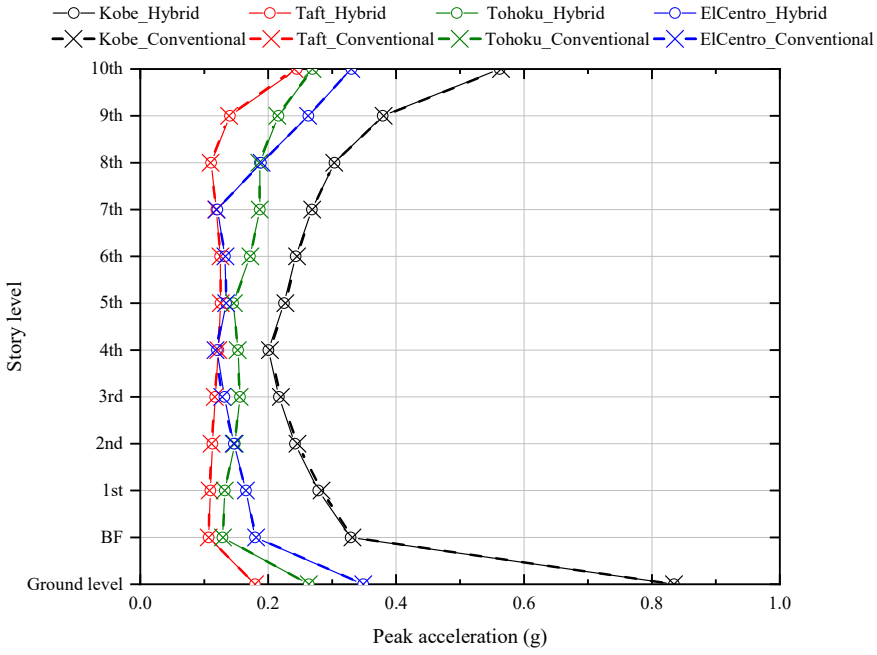

Figure 61: Peak floor accelerations of MB2: Hybrid vs. Conventional analyses.

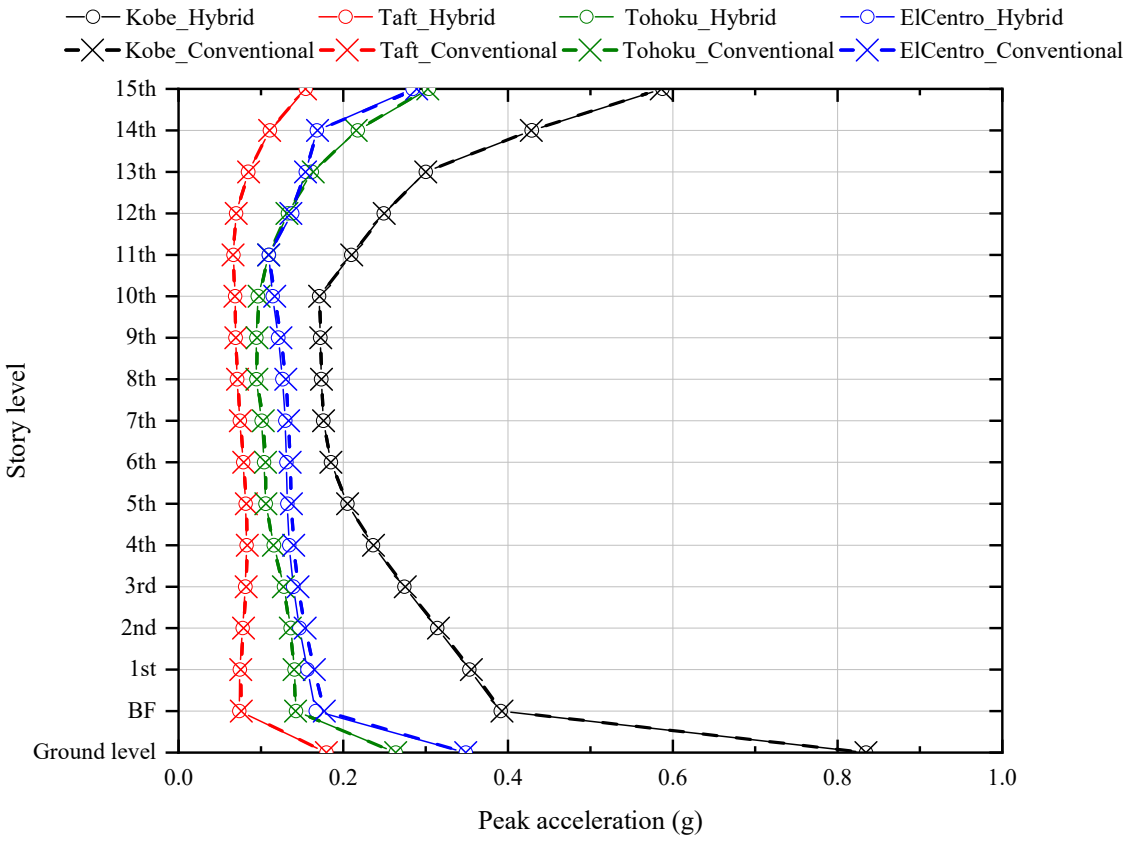

Figure 62: Peak floor accelerations of MB3: Hybrid vs. Conventional analyses.

4.3.6. Computation time

Table 23 presents the computation times of the twelve hybrid seismic analyses performed in this study: Buildings 1, 2, and 3 subjected to GMs 2, 3, 4, and 5. A Python script is written to perform the structural analysis of corresponding MDOFs and to load previously developed MLMs. All computations are performed on the same CPU (16 Intel® Xeon® W-2245 CPUs). When assuming a specific computer's performance, the consumed time depends mainly on the number of integration time-steps since the MLM would make predictions at each step. This number is a function of the duration of the GM, the original time step of the record (here, 0.02 s), and its subdivision (here, by 5) commonly chosen for accurate NTHA. The minimum computation time corresponds to GM2 (the shortest duration) and has an average of 12.80 min. The most time-consuming case happens obviously for the GM5 of longest duration, with an average value of 38.12 min. Furthermore, computation times of hybrid analyses of different buildings under the same GM are almost the same since analytical models describing the behavior of the respective superstructures are processed in a very short time (here, less than 1 s). It will only increase if more MLMs are used to simulate other components in the same building. Since the structural design is performed once in a lifetime of a building, the additional computation time is supposedly

negligible. Considering the accuracy advantage and the reasonable computation time, the efficiency of the proposed hybrid seismic analysis is proven in this study.

Table 23: Computation time of hybrid seismic analyses of model Buildings.

		GM2 (Kobe 1995 NS)	GM3 (Taft 1960 EW)	GM4 (Tohoku 1978 NS)	GM5 (El Centro 1940 NS)
GM duration (s)		15	19	23	27
Integration time steps		3750	4750	5750	6750
Time (min)	MB1	12.71	19.18	29.93	39.30
	MB2	12.66	20.25	29.53	38.76
	MB3	12.93	19.08	26.75	36.31

4.4.Hybrid seismic analysis of a tested full-scale building specimen

4.4.1. Overview of the tested building specimen

The building specimen tested at E-Defense shake table in August 2011, is a full-scale 5-story steel moment frame superstructure isolated consecutively by a TPB and a LRB/CLB isolation layers as described in Chapter III (Fig. 26-27). The specimen was initially constructed in 2008 for a previous test program about the performance of inter-story dampers [85]. It was designed according to Japanese code and design practice. The same specimen had been adapted and reused in August 2011 for the test program object of this study. Its structural layout is presented in Fig. 63. Many non-structural elements and content were incorporated to the structure for different research objectives. In this study, only the performance of the main structure in investigated. Details about design and structural drawings may be found in [49, 55, 85].

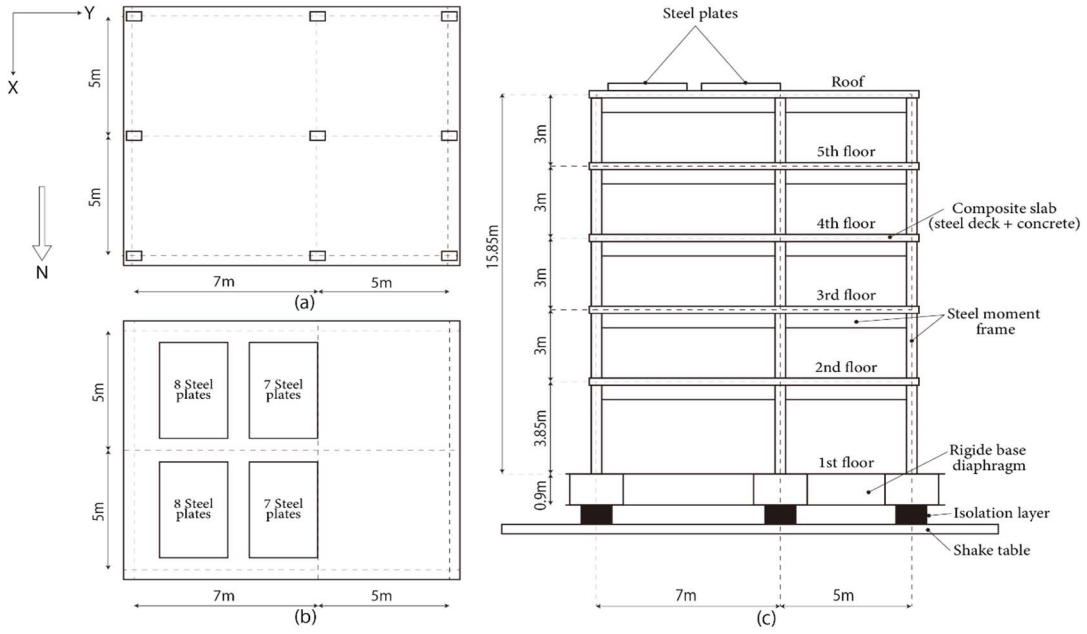

Figure 63: Structural layout of tested specimen: (a) Regular floor; (b) Roof; (c) Elevation

A series of 20 and 14 table motions were performed for the TPB and the LRB/CLB isolation support systems respectively (Tables 11-12). It includes harmonic waves and a large spectrum of synthetic and real earthquake ground motions. It is worth mentioning that realized table motions represent realistic loading conditions of different amplitudes, frequency contents, durations, and components (1D, 2D, 3D).

4.4.2. 3D-Frame model of the superstructure

In this Chapter, hybrid simulations are performed on a one-dimensional LMM derived from a 3D-frame model. The isolation layer is simulated by the TPB and LRB MLMs designed in Chapter 3, and the superstructure with Physics-based analytical models. Therefore, the latter should be as realistic as possible to minimize computation uncertainties from the superstructure. To this end, the fixed-base configuration has been modeled beforehand using the Software STERA_3D [12], and its natural modes were compared with test data (from 1D white noise excitations) and a reference OpenSees model [55]. Table 24 presents natural periods and mode shapes up to the 7^{th} mode in accordance with STERA_3D values. Relative errors to test data are provided, except for torsional modes which test data are not available. Eigen modes obtained from the STERA_3D model match very well with experimental data and even better than those obtained from the OpenSees model, with a maximum relative error of 2.15% in the 2^{nd} mode.

4.4.3. LMM of the superstructure

Hybrid analyses performed in this research work are applied on one-dimensional LMMs. The tested specimen was a 5-story steel moment frame building that can be assumed as a shear building, and it has deformed within the linear range in both isolation support configurations. Therefore, story weights, initial story stiffnesses, and inherent damping would be sufficient to model its equivalent one-dimensional LMMs. To this end, the following procedure is adopted:

- ✓ Automatic generation of LMM from the STERA_3D frame model [12],
- ✓ Optimization of story initial stiffnesses using the BOT (Chapter 2),
- ✓ Modeling of inherent damping matrix based on Stiffness and/or Mass matrices, and damping ratios of fundamental modes determined from white noise excitations of the fixed-based configuration of the tested specimen.

As shown in Table 25, test data from two table motions of the fixed-base configuration were used to this end: the 1987 Superstition Hills motion (Westermorland 3D) for BOT purpose, and the 1994 Northridge motion (Rinaldi 2D) for test purpose. The fixed-base specimen behaved linearly in both cases. Table 26 summarizes structural parameters of the optimized equivalent 1D LMMs. Fig. 64-67 show the comparison between acceleration responses simulated by the equivalent LMMs and the experiment. Both responses fit very well; thus, confirming the LMMs.

Table 24: Eigen modes of the tested specimen.

Mode No.	Nature	Direction	Period (sec.) / relative error (%)			Shape
			Test [55]	STERA_3D	OpenSees [55]	
1	Trans.	X	0.677	0.677 0.00%	0.687 1.48%	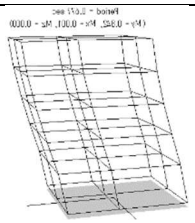
2	Trans.	Y	0.686	0.638 2.15%	0.666 2.15%	
3	Tors.	*	0.454	0.515	0.472	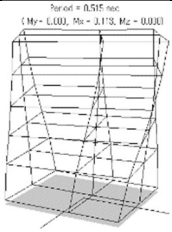
4	Trans.	Y	0.212	0.215 1.90%	0.219 3.79%	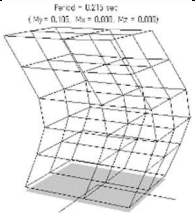
5	Trans.	X	0.205	0.200 1.96%	0.213 4.41%	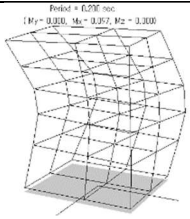
6	Tors.	*	*	0.167	*	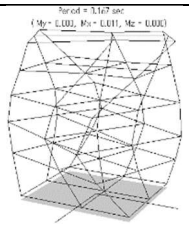
7	Trans.	Y	0.113	0.114 0.88%	0.111 1.77%	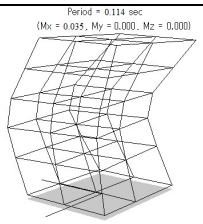

*Unreferred

Table 25: Table motions used to design the equivalent LMMs of the tested specimen.

Support configuration	Table motion	Scale factor	Peak A_{xy} (g)	Peak A_z (g)	Purpose
Fixed base	1987 Superstition Hills-Westermorland 3D-WSW	80%	0.17	0.2	BOT of LMM (Target floors: 1st & 5th)
	1994 Northridge-Rinaldi (XY)-RRS	35%	0.28	0.0	Test the LMM

Table 26: Equivalent LMMs properties of the tested specimen.

Story Level	Story stiffness (kN/cm)		Damping Matrix	
	X	Y	X	Y
5	127	157	Stiffness proportional (1st mode: 3.3%)	Stiffness proportional (1st mode: 2.5%)
4	127	157		
3	88	90		
2	88	90		
1	136	113		

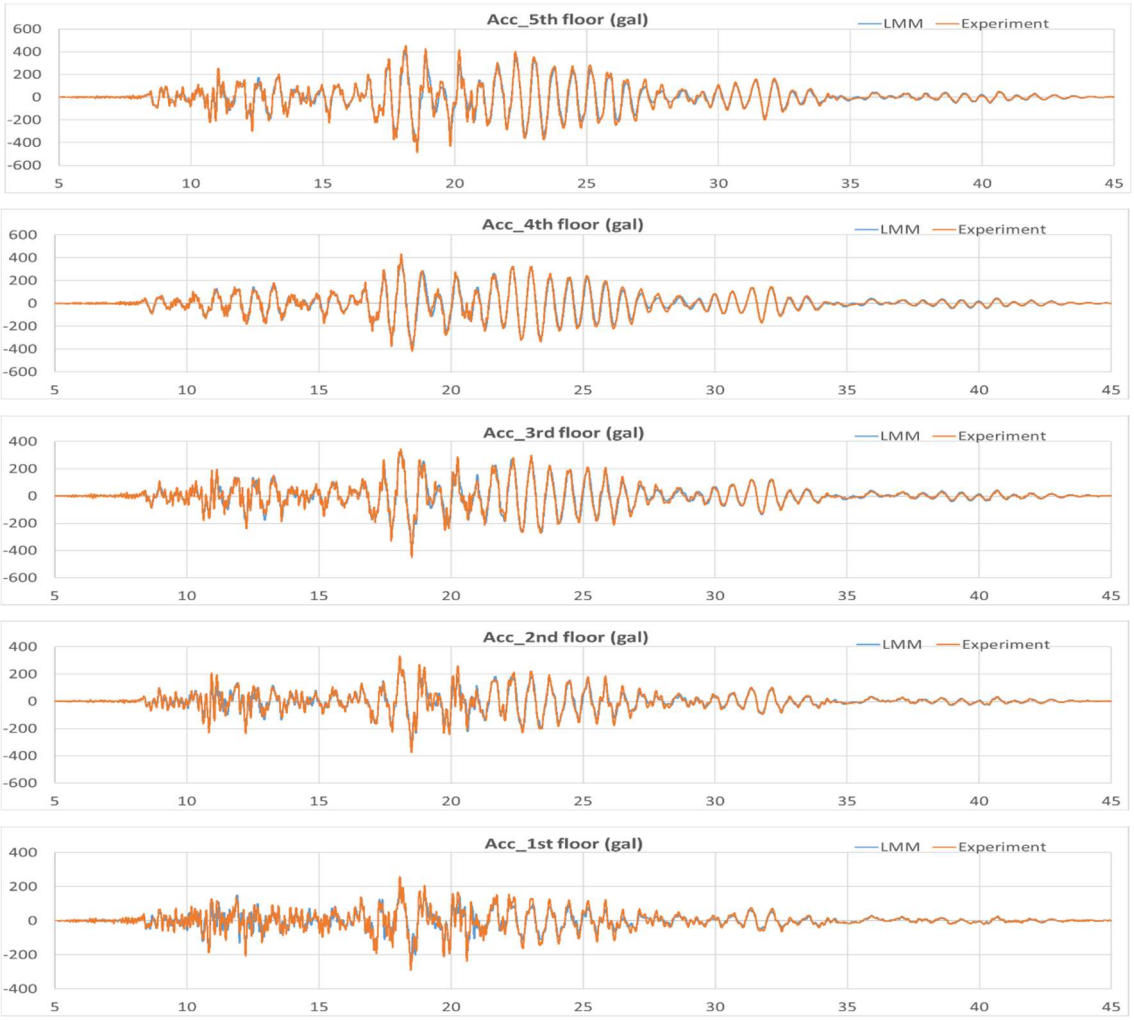

Figure 64: Fixed base_WSW_X: LMM acceleration responses vs. experiment.

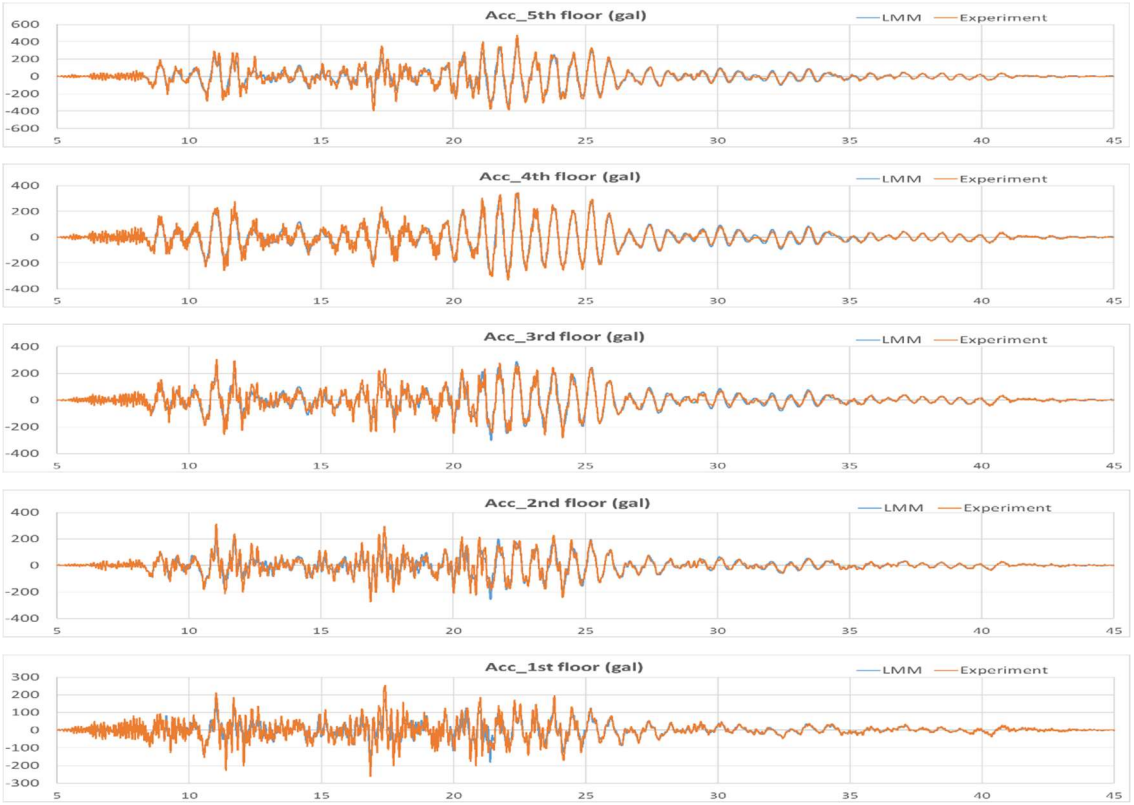

Figure 65: Fixed base_WSW_Y: LMM acceleration responses vs. experiment.

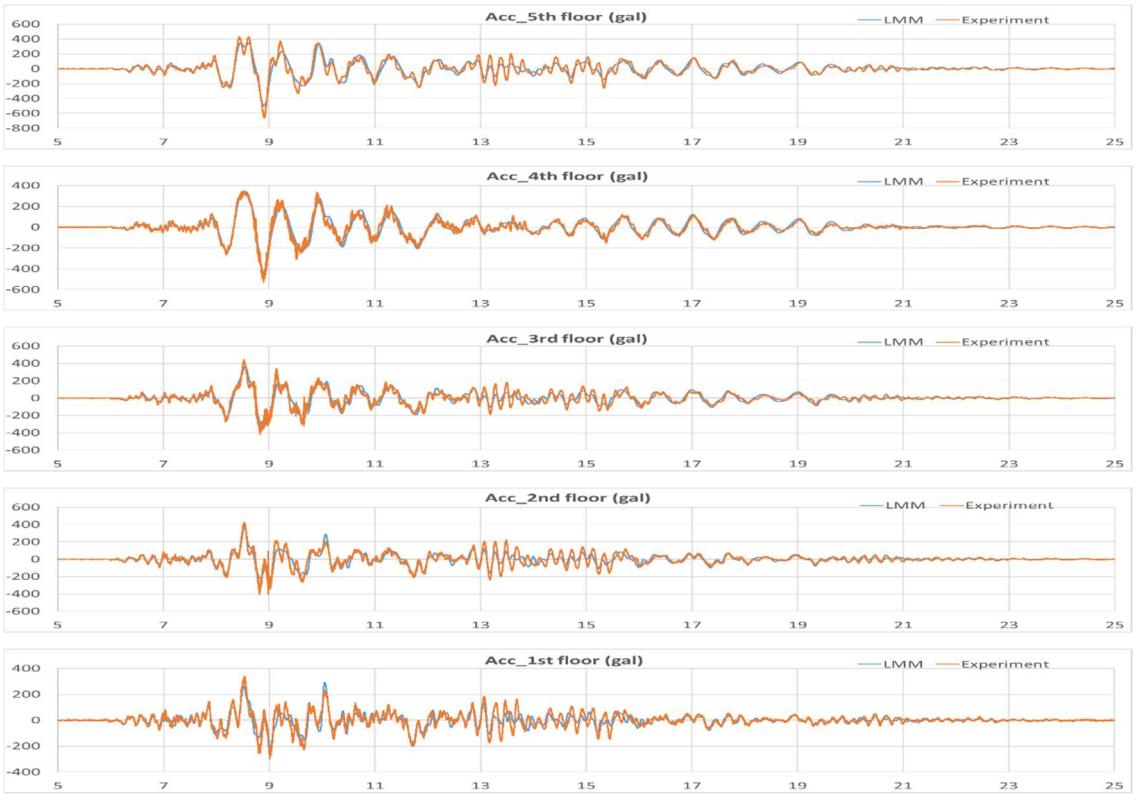

Figure 66: Fixed base_RRS_X: LMM acceleration responses vs. experiment.

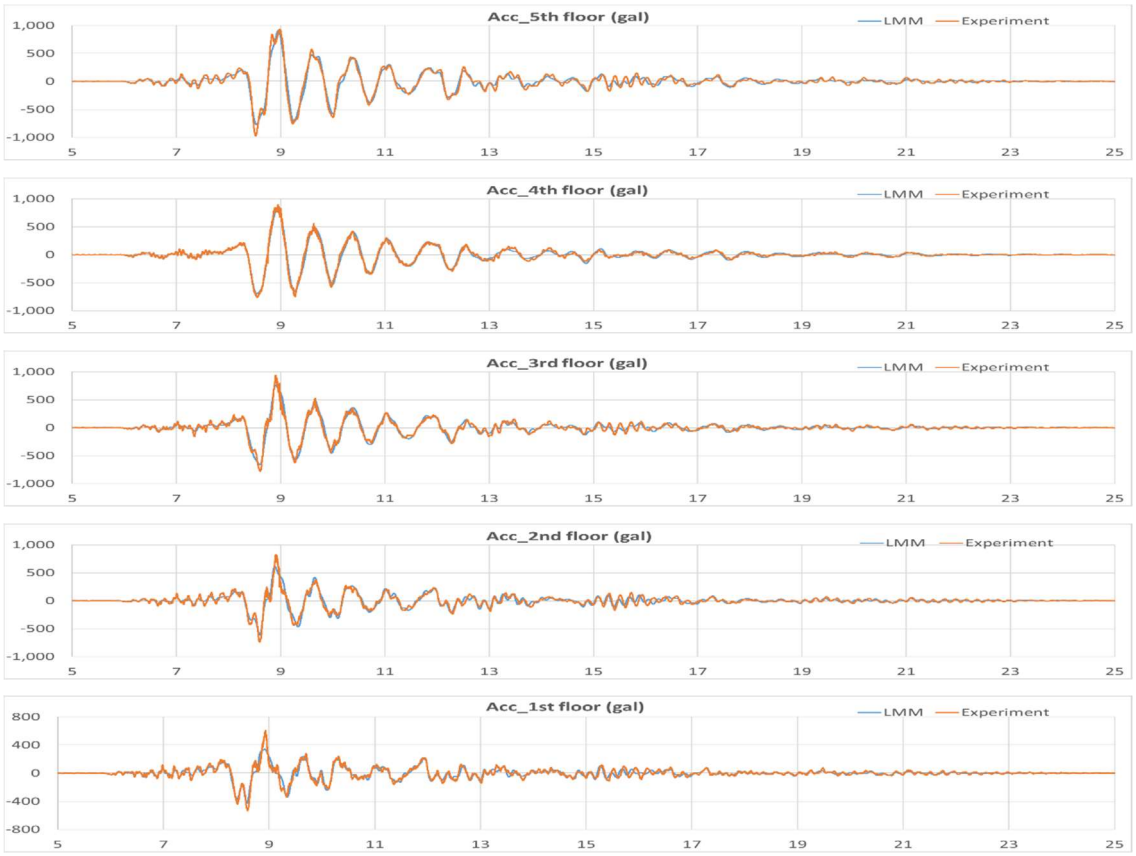

Figure 67: Fixed base_RRS_Y: LMM acceleration responses vs. experiment.

4.4.4. Structural responses of LRB-isolated specimen

The optimized LMM of the tested specimen (Chapter 4) was combined together with the LRB_MLM (Chapter 3) to perform hybrid analyses of the base-isolated configurations. Even though the LRB_MLM predicts the 2D structural behavior of the isolator, only 1D response was taken into consideration. The other component was set to zero. The four LRB devices (Fig. 27-b) are assumed to behave identically; therefore, the isolation layer response is assumed to be 4-times the one of a single LRB device. The initial stiffness of the isolation layer was included in the overall stiffness matrix but not in the damping matrix since both inherent and hysteretic damping of the isolator are included in its corresponding MLM. Fig. 68-72 show the comparison between hybrid analysis results and the experiment for three representative table motions in term of: isolation layer response, peak story acceleration, and peak story displacement. Even though the 1D LMM does not simulate the real behavior of the tested specimen such as the 2D interactions and torsional oscillations, but it could capture quite well the isolation layer energy dissipation capacity and peak story responses. It is worth mentioning that the LMM hybrid analysis overestimates slightly the deformation response of the isolation layer which is actually safe for the design. These results provide an experimental validation of the proposed hybrid analysis.

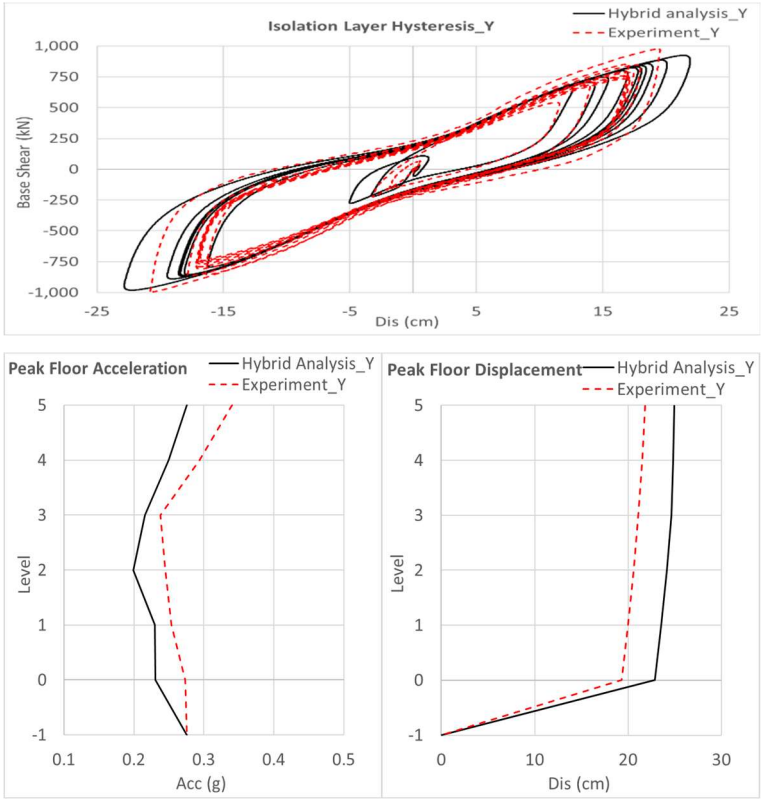

Figure 68: LRB_Sin1_Y: Hybrid analysis (black) vs. experiment (red).

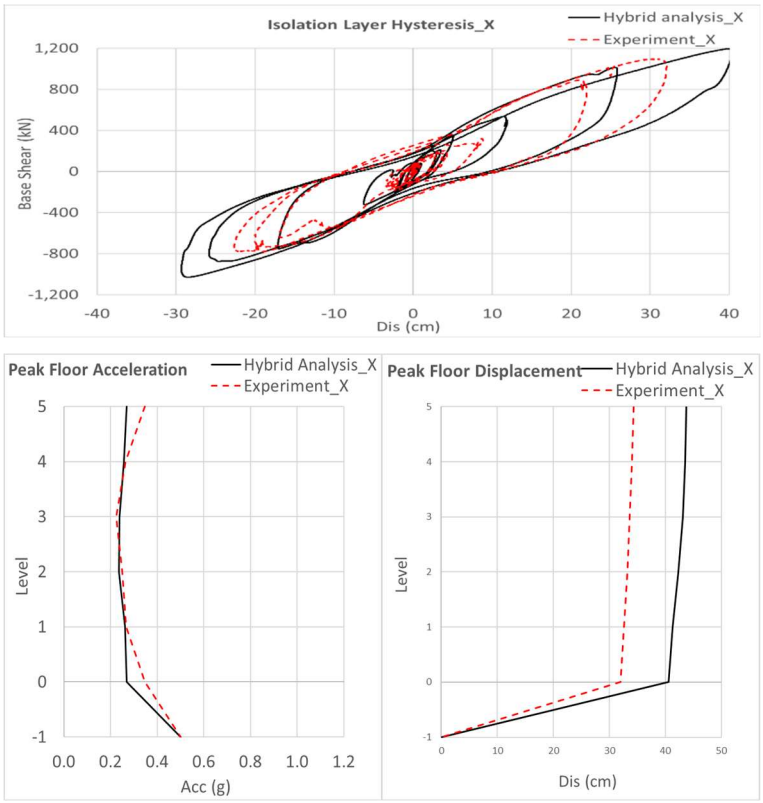

Figure 69: LRB_RRS-2D_X: Hybrid analysis (black) vs. experiment (red).

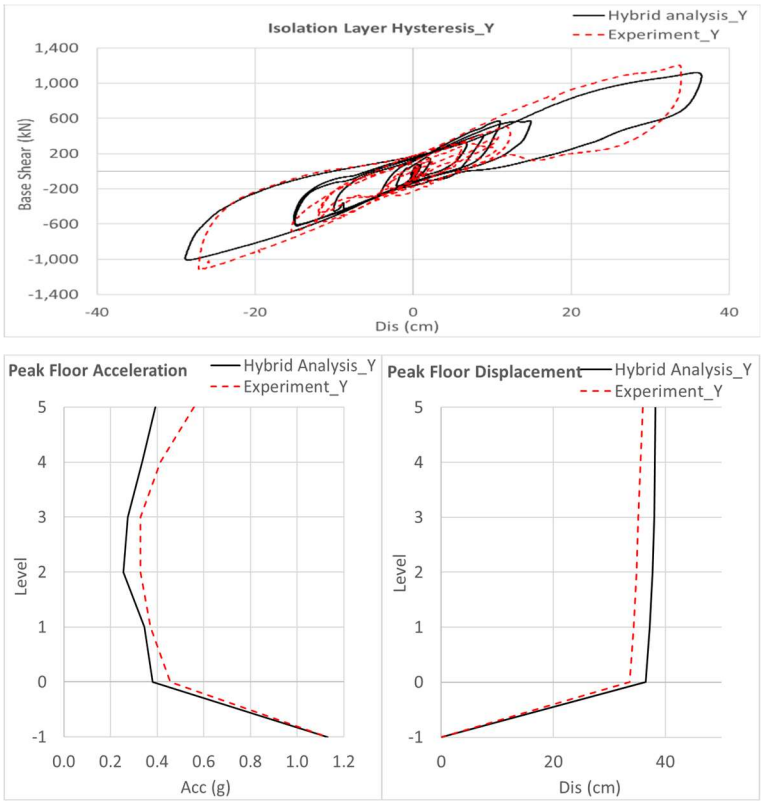

Figure 70: LRB_RRS-2D_Y: Hybrid analysis (black) vs. experiment (red).

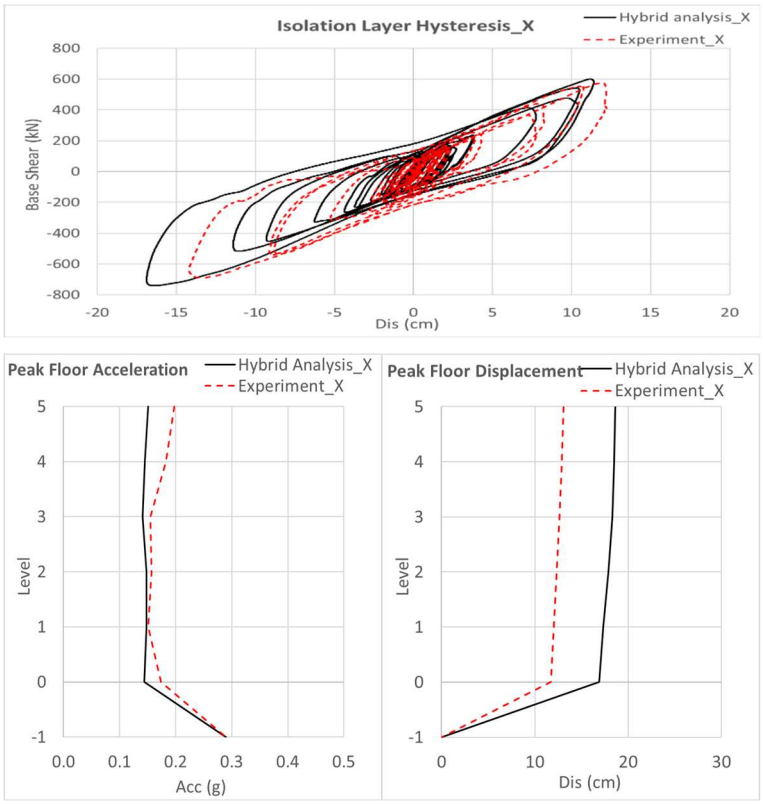

Figure 71: LRB_ELC130_X: Hybrid analysis (black) vs. experiment (red).

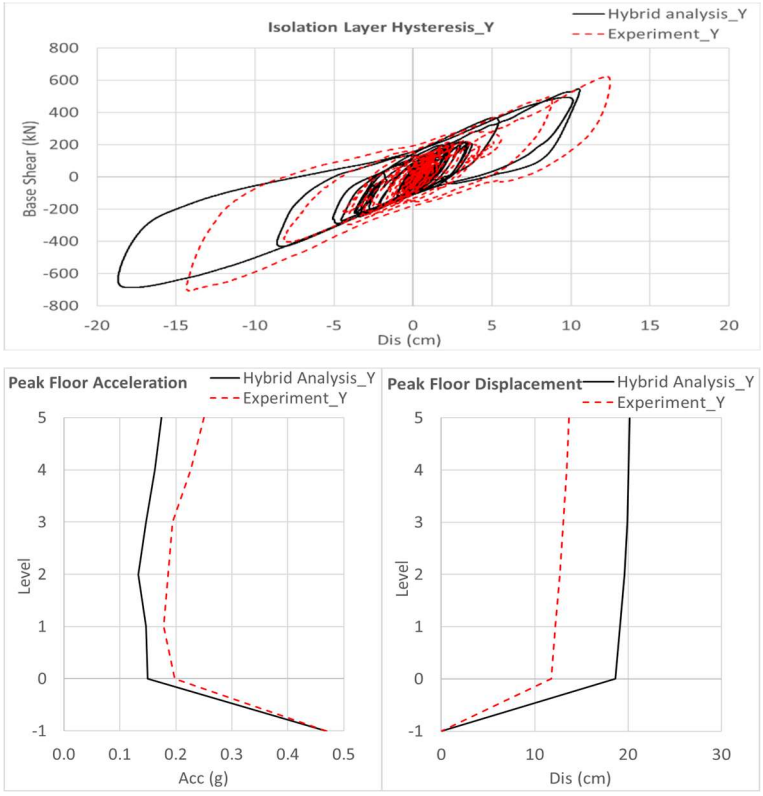

Figure 72: LRB_ELC130_Y: Hybrid analysis (black) vs. experiment (red).

4.4.5. Structural responses of TPB-isolated specimen

The optimized LMM of the tested specimen (Chapter 4) was combined together with the TPB_MLM (Chapter 3) to perform hybrid analyses of the base-isolated configurations. Even though the TPB_MLM predicts the 2D structural behavior of the isolator, only 1D response was taken into consideration. The other component was set to zero. The nine TPB devices (Fig. 27-a) are assumed to behave identically; therefore, the isolation layer response is assumed to be 9-times the one of a single TPB device. The initial stiffness of the isolation layer was included in the overall stiffness matrix but not in the damping matrix since both inherent and hysteretic damping of the isolator are included in its corresponding MLM. Since the analysis is performed on a LMM, the input vertical force for the TPB_MLM is set constant to $1/9^{th}$ the total weight of the specimen. Fig. 73-77 show the comparison between hybrid analysis results and the experiment for three representative table motions in term of: isolation layer response, peak story acceleration, and peak story displacement. Even though the 1D LMM does not simulate the real behavior of the tested specimen such as the 2D interactions and torsional oscillations, but it could capture quite well the isolation layer energy dissipation capacity and peak story responses for the Sin100 run. The LMM hybrid simulation failed to capture the true structural response of the tested specimen for other earthquake-like motions. TPBs are friction-based devices which behavior is strongly related to their axial force. The variable vertical force on each isolator can't be simulated by a LMM.

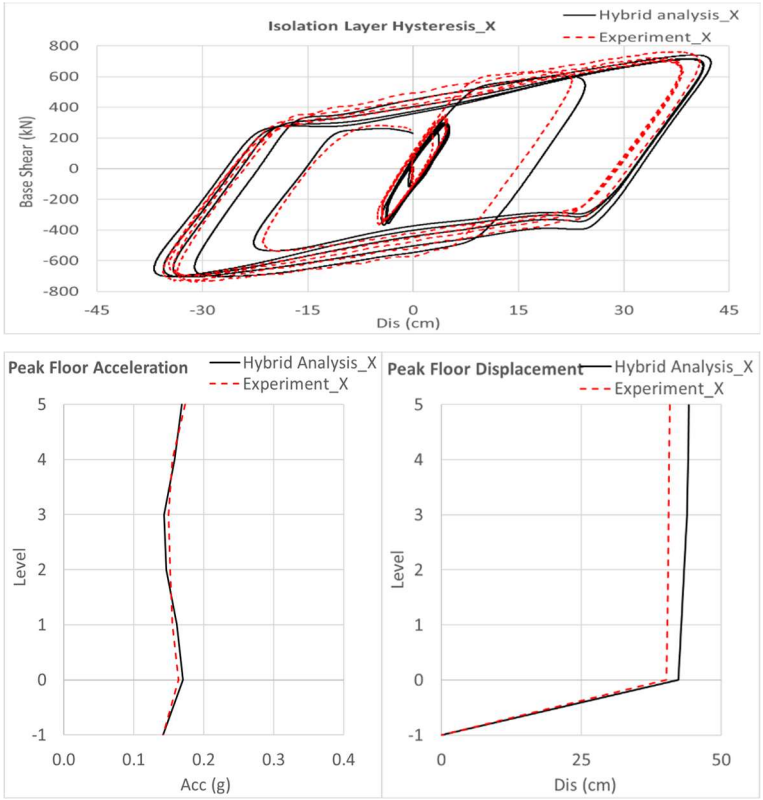

Figure 73: TPB_Sin100_X: Hybrid analysis (black) vs. experiment (red).

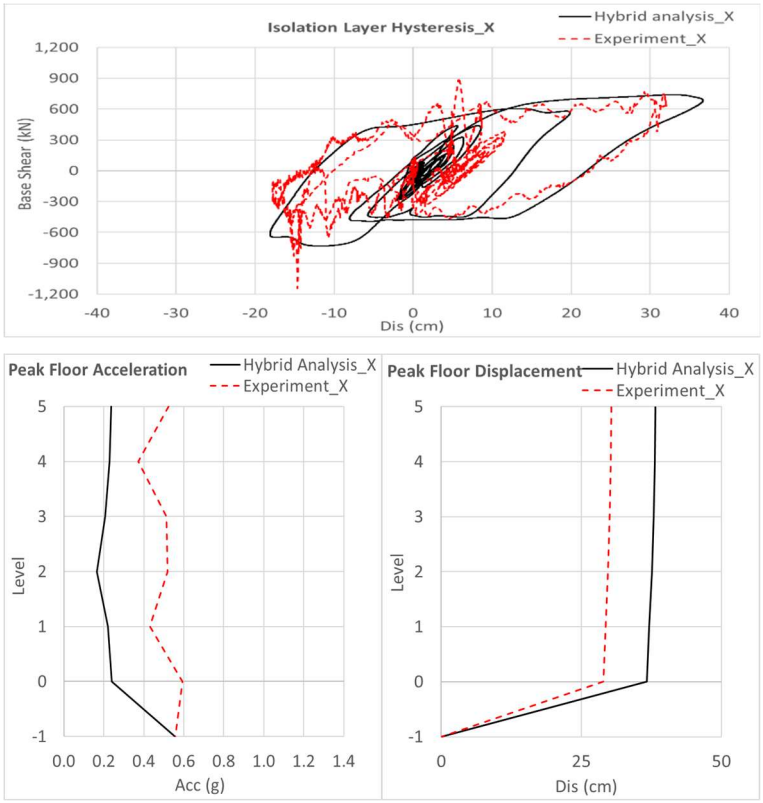

Figure 74: TPB_RRS-3D_X: Hybrid analysis (black) vs. experiment (red).

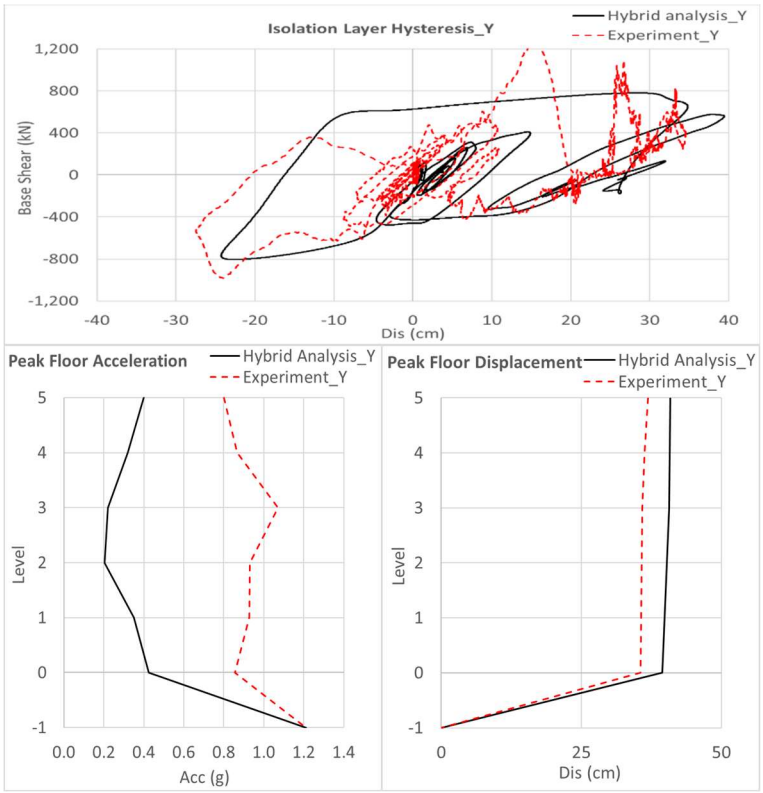

Figure 75: TPB_RRS-3D_Y: Hybrid analysis (black) vs. experiment (red).

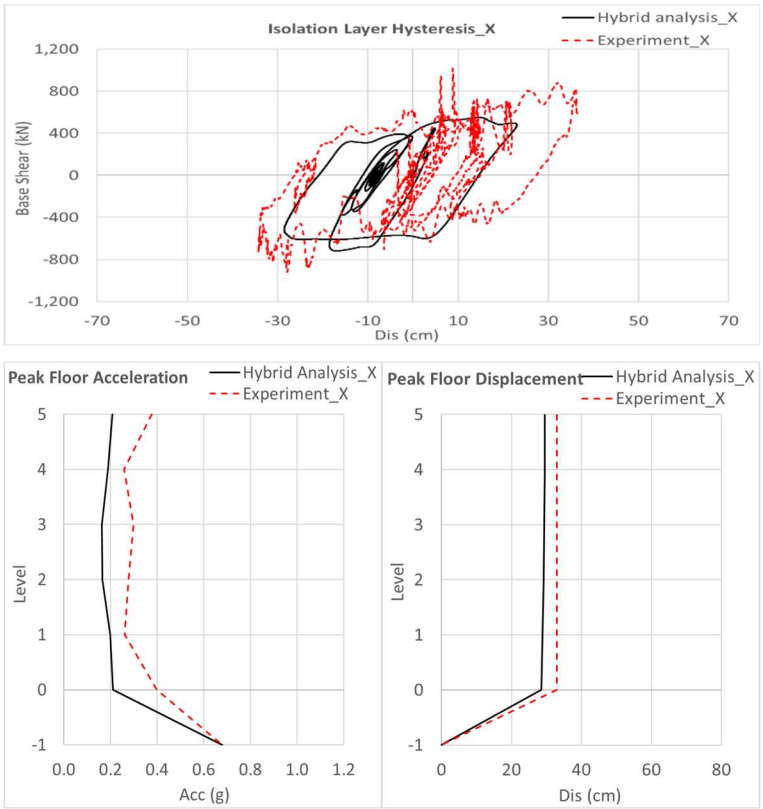

Figure 76: TPB_SYL100_X: Hybrid analysis (black) vs. experiment (red).

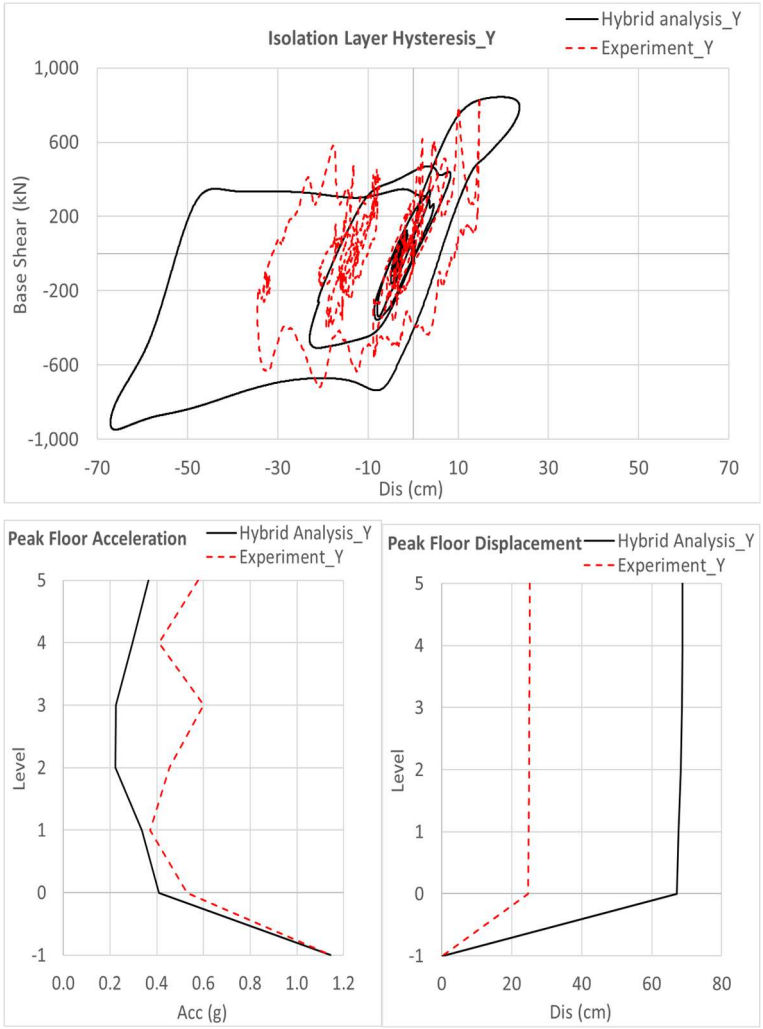

Figure 77: TPB_SYL100_Y: Hybrid analysis (black) vs. experiment (red).

4.4.6. Computation time

Tables 27-28 present the computation times of the three hybrid seismic analyses performed for each isolator type: LRB and TPB. A Python script is written to perform the structural analysis of equivalent LMMs and to load previously developed MLMs (Chapter 3). All computations are performed on the same CPU (16 Intel® Xeon® W-2245 CPUs). When assuming a specific computer's performance, the consumed time depends mainly on the number of integration time-steps since the MLM would make predictions at each step. This number is a function of the duration of the GM, the original time step of the record (here, 0.001 sec.), and its subdivision (here, by 1). The computation is always fast at the beginning of each simulation (about 1 sec per 20 integration-steps), then it slows down progressively as the sequence length (deformation time history) of the MLM is constantly increasing. Furthermore, the computation time is directly proportional to the number of MLM predictions performed at each time-step.

Table 27: Computation time of hybrid seismic analyses of tested LRB-specimen.

		Sin1	RRS-2D	ELC130
TM* duration (s)		20	20	40
Integration time steps		20001	20001	40001
Time	X	-	4h27	17h13
(h:min)	Y	3h41	4h25	17h20

*Table motion

Table 28: Computation time of hybrid seismic analyses of tested TPB-specimen.

		Sin100	RRS-3D	SYL100
TM* duration (s)		35	20	22
Integration time steps		35001	20001	22001
Time	X	13h12	4h32	5h28
(h:min)	Y	-	4h34	5h10

*Table motion

4.5.Conclusion

A hybrid seismic analysis is elaborated in this Chapter to compute the full response of a building structure, by incorporating both analytical and RNN models into an explicit time integration method. TPB and LRB MLMs designed in Chapter 3 are used to predict the nonlinear response of interest at each time-step of computation. Both synthetic building models and tested building specimens were used to check the efficiency of the proposed hybrid analysis. Hence, the following conclusions are formulated:

- ✓ The proposed hybrid seismic analysis computes the full response in term of acceleration, velocity, and displacement at each degree of freedom. The term hybrid is related to the time integration algorithm, not to the input data nor to the MLM architecture, offering a novel application of ML in civil engineering. Once the MLM is developed, it can be saved and reused to perform structural analysis of any building model containing the same component or group of components the MLM was trained to simulate. Therefore, the novel hybrid analysis proposed herein overcomes the shortcoming of most applications of ML in structural RPPs being limited to predict specific response quantity (s) of the structure (s) used in the training process.
- ✓ Hybrid seismic analyses responses of the studied building models under the four GMs are compared with results of the conventional analysis (OpS method) taking as a reference in this study. The linear response of the superstructures is very well evaluated with a maximum drift RMSE (respectively shear RMSE) of 0.00528 cm (respectively 27.1 kN)

among all the twelve cases. The hybrid analysis could accurately capture the nonlinear hysteresis loops of isolation layers. The maximum drift RMSE (respectively shear RMSE) at the isolation level was of 0.338 cm (respectively 46.3 kN) among all configurations. These results offer a numerical validation of the accuracy of the proposed hybrid seismic analysis since all RMSEs are acceptable in the earthquake engineering practice.

- ✓ Hybrid analyses of the tested LRB specimen showed quite well results compared to experiment. It could capture the complex nonlinear behavior of the isolation level and approximate peak story accelerations and deformations as well. However, hybrid analyses performed for the TPB case showed some limitations for earthquake-like excitations and cannot be reliable. It is mainly due to the incapability of a LMM to simulate the variable axial force on TPB devices. Such a limitation did no influence the LRB case since the latter was used together with CLB devices that take over the vertical weight under large deformations of the isolation layer.
- ✓ The computation times of the hybrid seismic analysis depends mainly on the number of time-integration steps, the number of MLM predictions at each integration step, and the MLM input sequence length. For synthetic building models, the maximum computation time was of 39.30 minutes corresponding to 6750 integration time-steps. For the tested specimen, , the maximum computation time was of 17h20min corresponding to 40001 integration time-steps. The capability of the proposed hybrid seismic analysis to simulate the true structural behavior of a structural model in a relatively acceptable time, proves its efficiency for the engineering practice.

Chapter 5: CONCLUSIONS AND FUTURE WORKS

This research work proposes an original way to predict the seismic response of building structures, by combining AI-based algorithms and conventional Physics-based models. AI is used as a complementary solution when conventional models fail to predict the real structural behavior under realistic loading conditions.

At the story level, two optimization methods, Response Surface Method (RSM) and Bayesian Optimization Technique (BOT), were investigated to calibrate story stiffnesses of the equivalent LMMs of three existing buildings using very limited acceleration records. Acceleration responses of updated LMMs fit very well with recorded wavs of studied buildings. The BOT showed constantly higher accuracy than RSM and less computational time. In case of TCH-EB, BOT took around 2 minutes to perform 50 iterations in a common laptop, whereas RSM took more than 10 hours. Moreover, the BOT could also perform well the non-linear case study. The developed Python script is considered as a program to be implemented in the seismic diagnosis system for online LMM updating; thus, for a more reliable 1st stage seismic evaluation.

At the component level, RNN algorithms are designed to simulate the structural behavior of complex component so far not well mastered by Physics. Isolation devices are selected as target components for this study. The framework proposed for developing the MLMs considers the main three steps to design a sequence-to-sequence prediction model: data framing, tuning of model architecture, and diagnosis of learning behavior. For the synthetic isolation system (LRB+NRB+Oil damper), a shallow GRU model with two recurrent layers of 60 cells each and a one-unit Dense layer as an output layer has been found the most appropriate in terms of accuracy, reliability, and simplicity. The MSEs were in the order of 10^{-4} on testing data. For the real full scale TPB and LRB isolators, Shallow recurrent networks of two hidden layers were found sufficient for the development of accurate and reliable MLMs for the problem treated in this study. Moreover, the learning behavior of GRU architectures was stable and less noisy than the LSTM counterpart. Therefore, two GRU layers of 95 units each were adopted for the TPB_MLM, and 60 units each for the LRB_MLM. The dropout regularization technique reduced the overfitting on train data and improved the generalization capability of developed models. A dropout ratio of 50% (40% respectively) applied to the 1st hidden layer, lead to the best performance on test data for the TPB_MLM (LRB_MLM respectively). The average shear RMSE of the TPB_MLM (LRB_MLM respectively) on test data was of 10.44 kN (8.42 kN respectively), which is considered acceptable in Structural Engineering. The R^2 values of 0.83 (0.97 respectively) reveal a strong correlation between experimental and predicted data. This excellent

performance is due to the data curation and the optimization of network architecture and hyperparameters, performed by following the proposed framework. Visualized prediction samples proved that developed MLMs could learn very well the two-dimensional behavior of studied isolators, by capturing most of the hysteresis features of experimental data: extremum shears, strength degradation, local softening and hardening, uplift excursions of TPBs, and pinching effects for LRBs; thus, the energy dissipation capacity. However, the TPB_MLM showed some limitations in predicting the residual shear.

The surrogate MLMs of structural components were then incorporated into an explicit time-integration method to perform the proposed hybrid seismic analysis. Simulated responses of the studied building models under the four GMs are compared with results of the conventional analysis (OpS method). The linear response of the superstructures is very well evaluated with a maximum drift RMSE (respectively shear RMSE) of 0.00528 cm (respectively 27.1 kN) among all the twelve cases. The hybrid analysis could accurately capture the nonlinear hysteresis loops of isolation layers. The maximum drift RMSE (respectively shear RMSE) at the isolation level was of 0.338 cm (respectively 46.3 kN) among all configurations. Hybrid analyses of the tested LRB specimen showed quite well results compared to experiment. It could capture the complex nonlinear behavior of the isolation level and approximate peak story accelerations and deformations as well. However, the TPB case showed some limitations for earthquake-like excitations and couldn’t provide reliable response. It is mainly due to the incapability of a LMM to simulate the variable axial force on TPB devices. Such a limitation did no influence the LRB case since the latter was used together with CLB devices that took-over the vertical weight under large deformations of the isolation layer.

The surrogate models developed in this study revealed the capability of ML in describing the complex structural behavior of the studied seismic isolation devices. These MLMs can be implemented within an explicit integration method to perform hybrid seismic analysis of the isolated building specimen. However, they are limited to the specific isolators used in the test program, and they do not include other known effects such as initial offset, fatigue, and aging. Furthermore, performed hybrid analysis of 1D LMMs showed its efficiency for synthetic data and the LRB experimental test, but it was not any more reliable for the TPB experimental case. These limitations concern more the LMM rather than the concept of the hybrid analysis. The former cannot include the 2D-interaction, torsional oscillation, overturning effect, and the specific variable vertical force on TPB devices. 3D-frame model analyses are strongly recommended for further studies to simulate better the isolation layer hystereses provided in Appendices C and D.

REFERENCES

1) Ipek C, Wolff ED, Constantinou MC. Accuracy of analytical models to predict primary and secondary system response in seismically isolated buildings. *Soil Dynamics and Earthquake Engineering* **2021**;150:106944.

2) Thai HT. Machine learning for structural engineering: A state-of-the-art review. *Structures* **2022**;38:448-491.

3) Xie Y, Sichani ME, Padgett JE, DesRoches R. The promise of implementing machine learning in earthquake engineering: A state-of-the-art review. *Earthquake Spectra* **2020**;36(4):1769-1801.

4) Zhang R, Chen Z, Chen S, Zheng J, Buyukozturk O, Sun H. Deep long short-term memory networks for nonlinear structural seismic response prediction. *Computers and Structures* **2019**;220:55-68.

5) Luo H, Paal SG. Machine learning-based backbone curve model of reinforced concrete columns subjected to cyclic loading reversals. *ASCE Journal of Computing in Civil Engineering* **2018**;32(5):04018042.

6) Charalampakis AE, Tsiatas GC, Kotsiantis SB. Machine learning and nonlinear models for the estimation of fundamental period of vibration of masonry infilled RC frame structures. *Engineering Structures* **2020**;216:110765.

7) Mekaoui N, Horioka T, Hayashi K, Saito T. Real-time parameter identification of seismically excited building structures using response surface method and Bayesian optimization technique: case study. *AIJ Journal of Structural Engineering* **2021**;67(B):643-653.

8) Nguyen HD, LaFave JM, Lee YJ, Shin M. Rapid seismic damage-state assessment of steel moment frames using machine learning. *Engineering Structures* **2022**;252:113737.

9) Xu Y, Lu X, Cetiner B, Taciroglu E. Real-time regional seismic damage assessment framework based on long short-term memory neural network. *Computer-Aided Civil and Infrastructure Engineering* **2021**;36(4):504-521.

10) K.Hayashi, T.Saito, T.Horioka and E.Sato: Implementation of real-time seismic diagnostic system on emergency management center buildings: system introduction and operational status on minucipal government office buildings, Journal of Civil Structural Health Monitoring, Vol.9, pp.529-541, **2019**.

11) T.Saito: Simulation and monitoring tools to protect disaster management facilities against earthquakes, IGNITE-AICCE'17 International Conference, AIP Conference Proceedings 1892, pp.020002-1--020002-6, **2017**.

12) T.Saito: STructural Earthquake Response Analysis 3D version 10.7 (STERA_3D v10.7), http://www.rc.ace.tut.ac.jp/saito/software-e.html#p01, accessed on 17 Septembre **2020**.

13) F.Naeim: Real-Time Damage Detection and Performance Evaluation for Buildings, Earthquakes and Health Monitoring of Civil Structures, M.Garevski (ed.), Springer, pp.167-196, **2013**.

14) K.Kanda, M.Nakashima, Y.Suzuki, S.Ogasawara: "q-NAVI": A case of market-based implementation of structural health monitoring in Japan, Earthquake Spectra, July **2020**.

15) L.Xie, A.Mita, L.Luo, M.Q.Feng:"Innovative substructure approach to estimating structural parameters of shear structures," *Journal of Structural Control and Health Monitoring*, First published: 19 January **2018**, DOI: 10.1002/stc.2139, Vol 25,Issue 4, e2139, 18 pages (2018.04).

16) S.W.Doebling, C.R.Farrar, M.B.Prime, D.W.Shevitz: Damage identification and health monitoring of structural and mechanical systems from changes in their vibration characteristics: a literature review. Technical Report LA‐13070‐MS, Los Alamos National Laboratory, Los Alamos, NM, **1996**.

17) N.Hirata: The earthquake in Osaka-Fu Hokubu on 18 June 2018 and its ensuing disaster, *Journal of Disaster Research*, Vol.13, No.4, pp.813-816, **2018**.

18) R.H.Myers, D.C.Montgomery, C.M.Anderson-cook: *RESPONSE SURFACE METHODOLOGY*, 4th edition, WILEY, **2016**.

19) K.Rajkumar, M.Muthukumar: Response surface optimization of electro- oxidation process for the treatment of C.I. Reactive Yellow 186 dye: reaction pathways. *Applied Water Science*. 7(2), 637−652 (**2017**).

20) M.A.Watson et al.: Response surface methodology investigation into the interactions between arsenic and humic acid in water during the coagulation process. *J. Hazard Mater*. 312, 150–158 (**2016**).

21) Machine learning group of the University of Sheffield: GPyOpt module, http://sheffieldml.github.io/GPyOpt/, accessed on 17 September **2020**.

22) GPyOpt tutorial, https://www.blopig.com/blog/wp-content/uploads/2019/10/GPyOpt-Tutorial1.html, accessed on 04 January **2021**.

23) C.E.Rasmussen and C.K.I.Williams: *Gaussian Processes for Machine Learning*, the MIT Press, **2006**.

24) N.D.Freitas: Bayesian optimisation, bandits and Thompson sampling, https://www.cs.ubc.ca/~nando/540-2013/lectures/l7.pdf, accessed on 17 September **2020**.

25) Mekaoui N, Saito T. A deep learning-based integration method for hybrid seismic analysis of building structures: numerical validation. *Applied Science* **2022**;12,3266.

26) Ryan KL, Dao ND, Sato E, Sasaki T, Okazaki T. Aspects of isolation device behavior observed from full-scale testing of an isolated building at E-Defense. *ASCE 20th Analysis & Computation Specialty Conference* **2012**; https://doi.org/10.1061/9780784412374.003.

27) Zayas VA, Low SS, Mahin SA. A simple pendulum technique for achieving seismic isolation. *Earthquake Spectra* **1990**;6(2):317-333.

28) Mokha A, Constantinou MC, Reinhorn AM, Zayas VA. Experimental study of friction-pendulum isolation system. *ASCE Journal of Structural Engineering* **1991**;117(4):1201-1217.

29) Fenz DM, Constantinou MC. Behavior of the double concave Friction Pendulum bearing. *Earthquake Engineering and Structural Dynamics* **2006**;35(11):1403-1424.

30) Fenz DM, Constantinou MC. Spherical sliding isolation bearings with adaptive behavior: Theory. *Earthquake Engineering and Structural Dynamics* **2008**;37(2):163-183.

31) Tsai CS, Lin YC, Su HC. Characterization and modeling of multiple friction pendulum isolation system with numerous sliding interfaces. *Earthquake Engineering and Structural Dynamics* **2010**;39(13):1436-1491.

32) Sarlis AA, Constantinou MC. A model of triple friction pendulum bearing for general geometric and frictional parameters. *Earthquake Engineering and Structural Dynamics* **2016**;45(11):1837-1853.

33) Becker TC, Mahin SA. Experimental and analytical study of the bi-directional behavior of the triple friction pendulum isolator. *Earthquake Engineering and Structural Dynamics* **2012**;41(3):355-373.

34) Ray T, Sarlis AA, Reinhorn AM, Constantinou MC. Hysteretic models for sliding bearings with varying frictional force. *Earthquake Engineering and Structural Dynamics* **2013**;42(15):2341-2360.

35) Dao ND, Ryan KL, Sato E, Sasaki T. Predicting the displacement of triple pendulum™ bearings in a full-scale shaking experiment using a three-dimensional element. *Earthquake Engineering and Structural Dynamics* **2013**;42(11):1677-1695.

36) Mokha A, Constantinou MC, Reinhorn A. Teflon bearings in base isolation I: Testing. *ASCE Journal of Structural Engineering* **1990**;116(2):438-454.

37) Konstantinidis D, Kelly JM, Makris N. Experimental investigations on the seismic response of bridge bearings. Report No. EERC 2008-02, Earthquake Engineering Research Center, University of California, Berkeley, **2008**.

38) Kalpakidis IV, Constantinou MC. Effects of heating and load history on the behavior of lead-rubber bearings. Report No. MCEER-08-0027, Multidisciplinary Center for Earthquake Engineering Research, Buffalo, NY, **2008**.

39) Kalpakidis IV, Constantinou MC. Effects of heating on the behavior of lead-rubber bearings. I: Theory. *ASCE Journal of Structural Engineering* **2009**;135(12):1440-1449.

40) Kalpakidis IV, Constantinou MC. Effects of heating on the behavior of lead-rubber bearings. II: Verification of theory. *ASCE Journal of Structural Engineering* **2009**;135(12):1450-1461.

41) Robinson WH. Lead-rubber hysteretic bearings suitable for protecting structures during earthquakes. *Earthquake Engineering and Structural Dynamics* **1982**;10(4):593-604.

42) Kalpakidis IV, Constantinou MC, Whittaker AS. Modeling strength degradation in lead-rubber bearings under earthquake shaking. *Earthquake Engineering and Structural Dynamics* **2010**;39(13):1533-1549.

43) Kumar M, Whittaker AS, Constantinou MC. An advanced numerical model of elastomeric seismic isolation bearings. *Earthquake Engineering and Structural Dynamics* **2014**;43(13):1955-1974.#

44) Liu Y, Zhong W, Mercan O, Tan P, Zhou F. A new nonlinear model to describe the degradation law of the mechanical properties of lead-rubber bearings under high-speed horizontal loading. *Structural Control and Health Monitoring* **2021**;28(12):e2836.

45) Eem S, Hahm D. Large strain nonlinear model of lead rubber bearings for beyond design basis earthquakes. *Nuclear Engineering and Technology* **2019**;51(2):600-606.

46) Marquez JF, Mosqueda G, Kim MK. Modeling of lead rubber bearings under large cyclic material strains. *ASCE Journal of Structural Engineering* **2021**;147(11):04021170.

47) Minewaki S, Yamamoto M, Higashino M, Hamaguchi H, Yoneda H. A study on performance of large size isolators for super high-rise isolated buildings through full-scale tests. Takenaka Technical Research Report No. 66, Takenaka Corporation, Japan, **2010**. (In Japanese)

48) Kim JH, Kim MK, Choi I. Experimental study on seismic behavior of lead-rubber bearing considering bi-directional horizontal input motions. *Engineering Structures* **2019**;198(4a):109529.

49) Coria CB, Ryan KL. Response of lead rubber bearings in a hybrid isolation system during a large-scale shaking experiment of an isolated building. Ph.D. dissertation, University of Nevada, Reno, USA, **2015**.

50) Weisman J, Warn GP. Stability of elastomeric and lead-rubber seismic isolation bearings. *ASCE Journal of Structural Engineering* **2012**;138(2):215-223.

51) Kelly JM, Marsico MR. Tension buckling in rubber bearings affected by cavitation. *Engineering Structures* **2013**;56:656-663.

52) Nakamura T, Kouchiyama O, Kikuchi M. Behaviors of lead rubber bearing under horizontal bi-directional loading test. *Proceedings of the 15th World Conference on Earthquake Engineering*, Lisbon, Portugal, September 24-28, **2012**.

53) MLIT. The Notification and Commentary on the Structural Calculation Procedures for Building with Seismic Isolation; Ministry of Land, Infrastructure, Transport and Tourism: Tokyo, Japan, **2000**. (In Japanese)

54) Brownlee J. *Long Short-Term Memory Networks with Python*. Machine Learning Mastery; **2020** v1.7. 245 p. Available from https://machinelearningmastery.com/lstms-with-python/.

55) Dao ND, Ryan KL. Seismic response of a full-scale 5-story steel building isolated by triple pendulum bearings under 3D excitations. Ph.D. dissertation, University of Nevada, Reno, USA, **2012**.

56) Huang YN, Whittaker AS, Kennedy RP, Mayes RL. Assessment of base-isolated nuclear structures for design and beyond-design basis earthquake shaking. Report No. MCEER-09-0008, Multidisciplinary Center for Earthquake Engineering Research, Buffalo, NY, **2009**.

57) Okazaki T, Sato K, Sato E, Sasaki T, Kajiwara K, Ryan K, Mahin S. NEES/E-Defense base isolation tests: performance of triple-pendulum bearings. *Proceedings of the 15th World Conference on Earthquake Engineering*, Lisbon, Portugal, September 24-28, **2012**.

58) Becker TC, Bao Y, Mahin SA. Extreme behavior in a triple friction pendulum isolated frame. *Earthquake Engineering and Structural Dynamics* **2017**;46(15):2683-2698.

59) Rumelhart DE, Hinton GE, Williams RJ. Learning representations by back-propagating errors. *Nature* **1986**;323:533-536.

60) Hochreiter S, Schmidhuber J. Long short-term memory. *Neural Computation* **1997**;9(8):1735-1780.

61) Cho K, Merrienboer BV, Bahdanau D, Bengio Y. On the properties of neural machine translation: Encoder-decoder approaches. *Proceedings of SSST-8, Eight Workshop on Syntax, Semantics and Structure in Statistical Translation (W14-4012)* **2014**;103-111.

62) Petnehazi G. Recurrent neural network for time series forecasting. arXiv **2019**, arXiv:1901.00069

63) Yang S, Zhou Y, Yu X. LSTM and GRU neural network performance comparison study. International Workshop on Electronic Communication and Artificial Intelligence (IWECAI) **2020**;20054050.

64) Chung J, Gulcehre C, Cho K, Bengio Y. Empirical evaluation of gated recurrent neural networks on sequence modeling. NIPS Deep Learning and Representation Learning Workshop **2014**;arXiv:1412.3555v1.

65) Srivastava N, Hinton G, Krizhevsky A, Sutskever I, Salakhutdinov R. Dropout: a simple way to prevent neural networks from overfitting. *Journal of Machine Learning Research* **2014**;15(56):1929-1958.

66) Keras API Reference/Losses. Available online: https://keras.io/api/losses/ (accessed on 25 January **2022**).

67) Keras API Reference/Optimizers. Available online: https://keras.io/api/optimizers/ (accessed on 25 January **2022**).

68) Levine, Y.; Sharir, O.; Shashua, A. Benefits of depth for long-term memory of recurrent networks. In Proceedings of the 6th International Conference on Learning Representations (ICLR), Vancouver, Canada, April-May **2018**.

69) Kingma, D.P.; Ba, J.L. Adam: A method for stochastic optimization. In Proceedings of the 3rd International Conference on Learning Representation (ICLR), San Diego, USA, May **2015**.

70) Smith, L.N. Cyclical learning rates for training neural networks. In Proceedings of the 2017 IEEE Winter Conference on Applications of Computer Vision (WACV), Santa Rosa, USA, March **2017**.

71) Li, H.; Xu, Z.; Taylor, G.; Studer, C.; Goldstein, T. Visualizing the loss landscape of neural nets. In Proceedings of the 9th International Conference on Learning Representation (ICLR), May **2021** (virtual only).

72) Zhang, R.; Liu, Y.; Sun, H. Physics-informed multi-LSTM networks for metamodeling of nonlinear structures. *Comput. Methods Appl. Mech. Eng.* **2020**, *369*, 113226.

73) Sengupta, P.; Li, B. Hysteresis Modeling of Reinforced Concrete Structures: State of the Art. *ACI Struct. J.* **2017**, *114*, 25–38.

74) Dokainish, M.A.; Subbaraj, K. A survey of direct time-integration methods in computational structural dynamics-I. Explicit methods. *Comput. Struct.* **1989**, *32*, 1371–1386.

75) Subbaraj, K.; Dokainish, M.A. A survey of direct time-integration methods in computational structural dynamics-II. Implicit methods. *Comput. Struct.* **1989**, *32*, 1387–1401.

76) Brownlee, J. Deep Learning for Time Series Forecasting. Machine Learning Mastery; **2020** v1.8. 555p. Available online: https://machinelearningmastery.com/ deep-learning-for-time-series-forecasting/ (accessed on 25 January 2022).

77) Eshkevari, S.S.; Takac, M.; Pakzad, S.N.; Jahani, M. DynNet: Physics-based neural architecture design for nonlinear structural response modeling and prediction. *Eng. Struct.* **2021**, *229*, 111582.

78) Nakashima, M.; Kato, H.; Takaoka, E. Development of real-time pseudo dynamic testing. *Earthq. Eng. Struct. Dyn.* **1992**, *21*, 79–92.

79) Nakashima, M. Hybrid simulation: An early history. *Earthq. Eng. Struct. Dyn.* **2020**, *49*, 949–962.

80) Schellenberg, A.H.; Mahin, S.A.; Fenves, G.L. *Advanced Implementation of Hybrid Simulation*; University of California, Berkeley: Pacific Earthquake Engineering Research Center (Berkeley, USA): **2009**; Volume 104, 286p.

81) Nakashima, M.; Ishida, M.; Ando, K. Integration techniques for substructure pseudo dynamic test. *J. Struct. Constr. Eng.* **1990**, 417, 107–117. (In Japanese)

82) Hughes, T.J.R.; Pister, K.S.; Taylor, R.L. Implicit-explicit finite elements in nonlinear transient analysis. *Comput. Methods Appl. Mech. Eng.* **1979**, *17*, 159–182.

83) Newmark, N.M. A method of computation for structural dynamics. *ASCE J. Eng. Mech. Div.* **1959**, 85, 67–94.

84) Lumped Mass Models (with Seismic Isolation). Available online: http://www.rc.ace.tut.ac.jp/saito/software_sample_SI02-e.html (accessed on 25 January **2022**).

85) Kasai, K.; Hiroshi, I.; Yoji, O.; Tsuyoshi H.; Koichi, K.; Shojiro, M.; Hitoshi, O.; Masato, I. Full-scale table tests of 5-story building with various dampers. *Proc., 7th Intern. Conf. on Urban Earthquake Engineering & 5th Intern. Conf. on Earthquake Engineering*. Tokyo Inst. Tech., Tokyo, Japan, **2010**.

APPENDIX A: Python script for conventional seismic analysis of MDOF

```python
# -*- coding: utf-8 -*-
"""
Seismic Analysis of MDOF: Operator Splitting Method (OpS)

Created on Mon May  3 13:10:31 2021

@author: MEKAOUI Nabil
"""
import numpy as np
import numpy.linalg as la

# Time         : s
# Mass         : kN.s2/cm
# Force        : kN
# Stiffness    : kN/cm
# Damping      : kN.s/cm
# Acceleration : gal
# Velocity     : kine
# Displacement : cm

#BiLinear Hysteretic Response
def hystBL(dr0,dr1,l):
    global State, D0
    k1, k2, dy = K1[l], K2[l], DY[l]
    if State[l] == 0:
        if dr1-dr0>=0 and dr1-D0[l]<dy:
            return k1*(dr1-D0[l])+k2*D0[l]
        elif dr1-dr0>=0 and dr1-D0[l]>=dy:
            State[l],D0[l] = 1, dr1-dy
            return k1*dy+k2*(dr1-dy)
        elif dr1-dr0<0 and dr1-D0[l]>-dy:
            return k1*(dr1-D0[l])+k2*D0[l]
        else:
            State[l],D0[l] = -1, dr1+dy
            return -k1*dy+k2*(dr1+dy)
    elif State[l] == 1:
        if dr1-dr0<0 and dr1-D0[l]>=-dy:
            State[l] = 0
            return k1*(dr1-D0[l])+k2*D0[l]
        elif dr1-dr0<0 and dr1-D0[l]<-dy:
            State[l],D0[l] = -1, dr1+dy
            return k2*(dr1+dy)-k1*dy
        else:
            D0[l] = D0[l]+dr1-dr0
            return k1*dy+k2*(D0[l]+dr1-dr0)
    else:
        if dr1-dr0>0 and dr1-D0[l]<=dy:
            State[l] = 0
            return k1*(dr1-D0[l])+k2*D0[l]
        elif dr1-dr0>0 and dr1-D0[l]>dy:
            State[l],D0[l] = 1, dr1-dy
            return k2*(dr1-dy)+k1*dy
        else:
            D0[l] = D0[l]+dr1-dr0
            return -k1*dy+k2*(D0[l]+dr1-dr0)

```

```
#Oil damper without elastic spring
def OilD(ddr):
    if -Vr<=ddr/dtt<=Vr:
        return C1*ddr/dtt
    elif ddr/dtt>Vr:
        return C2*ddr/dtt+Qc
    else:
        return C2*ddr/dtt-Qc

#Operator Splitting Integration
def ops(acc0,vel0,dis0,dr0,accg_1):
    Sh1, Force1   = np.zeros(n), np.zeros(n)
    dis1p         = dis0+vel0*dtt+1/4*acc0*(dtt**2)
    P1, dr_p[0,i] = -M@np.ones(n)*accg_1, dis1p[0]
    for j in range(1,n):
        dr_p[j,i] = dis1p[j]-dis1p[j-1]
    for l in range(n):
        Sh1[l]  = hystBL(dr0[l], dr_p[l,i],l)
        if l==0:
            vel_oil[i] = (dr_p[l,i]-dr0[l])/dtt
            Foil[i]    = OilD(dr_p[l,i]-dr0[l])
            Sh1[l]     = Sh1[l] + Foil[i]
    for l in range(n-1):
        Force1[l]  = Sh1[l] - Sh1[l+1]
    Force1[n-1]    = Sh1[n-1]
    F1   = -C@(vel0+1/2*acc0*dtt)-Force1+P1
    acc1 = invL@F1
    vel1 = vel0+1/2*(acc0+acc1)*dtt
    dis1 = dis0+vel0*dtt+1/4*(acc0+acc1)*(dtt**2)
    return acc1, vel1, dis1, Sh1

#Reading input wave
ndata, dt = 1151, 0.02
Accg      = np.genfromtxt('3.Ground Motions/Tohoku1978_NS.txt', skip_header=2, delimiter=',', max_rows=ndata)

#Input structure
n, h   = 16, 0.02
M      = np.diag([4500, 3000, 3000, 3000, 3000, 3000, 3000, 3000, 3000, 3000, 3000, 3000, 3000, 3000, 3000, 3000])/980
K1     = np.array([99, 644, 639, 628, 612, 590, 563, 531, 494, 451, 402, 349, 290, 225, 156, 80])*10
FY     = np.array([990, 20000, 20000, 20000, 20000, 20000, 20000, 20000, 20000, 20000, 20000, 20000, 20000, 20000, 20000, 20000])
K, K2  = np.diag(K1), np.array([0.031, 0.1, 0.1, 0.1, 0.1, 0.1, 0.1, 0.1, 0.1, 0.1, 0.1, 0.1, 0.1, 0.1, 0.1, 0.1])*K1
DY, D0 = FY/K1, np.zeros(n)
State  = np.zeros(n,int)
for i in range(0,n-1):
    K[i,i]   = K[i,i]+ K[i+1,i+1]
    K[i,i+1] = K[i+1,i] = -K[i+1,i+1]
Vr, C1 = 320/10, 1.237*10
C2     = 0.067*C1
Qc     = (C1-C2)*Vr

#Eigenvalue problem
invM           = la.inv(M)
OMEGA2,phi_rev = la.eig(invM@K)
OMEGA = np.sort(np.sqrt(OMEGA2))
T     = 2*np.pi/OMEGA

```

```
#Construction of damping Matrix
C = (2*h/OMEGA[0])*K

#Data pre-processing
tsub = 5
dtt  = dt/tsub
t    = np.arange(0,(ndata-1)*dt+dtt,dtt)
L    = M+1/2*C*dtt+1/4*K*(dtt**2)
invL = la.inv(L)
accg, accg[0]= np.zeros(len(t)), Accg[1]/tsub
acc,acc[:,0] = np.zeros((n,len(t))), -accg[0]
vel, dis, dr = np.zeros((n,len(t))), np.zeros((n,len(t))), np.zeros((n,len(t)))
Sh, dr_p     = np.zeros((n,len(t))), np.zeros((n,len(t)))
Foil, vel_oil= np.zeros(len(t)), np.zeros(len(t))
for i in range(0,ndata-1):
    for j in range(0,tsub+1):
        accg[i*tsub+j]=Accg[i]+j*((Accg[i+1]-Accg[i])/tsub)

for i in range(1,(ndata-1)*tsub+1):
    #Operator splitting integration
    acc[:,i],vel[:,i],dis[:,i],Sh[:,i] = ops(acc[:,i-1],vel[:,i-1],dis[:,i-1],dr[:,i-1],accg[i])
    #Corrector drift calculation
    dr[0,i] = dis[0,i]
    for j in range(1,n):
        dr[j,i] = dis[j,i]-dis[j-1,i]
```

APPENDIX B: Python script for hybrid seismic analysis of MDOF

```python
# -*- coding: utf-8 -*-
"""
Seismic Analysis of MDOF: Hybrid Integration Method (OpSML)

Created on Thu May 27 14:59:33 2021

@author: MEKAOUI Nabil
"""
import numpy            as np
import numpy.linalg     as la
from   keras.models     import load_model

# Time         : s
# Mass         : kN.s2/cm
# Force        : kN
# Stiffness    : kN/cm
# Damping      : kN.s/cm
# Acceleration : gal
# Velocity     : kine
# Displacement : cm

#BiLinear Hysteretic Response
def hystBL(dr0,dr1,l):
    global State, D0
    k1, k2, dy = K1[l], K2[l], DY[l]
    if State[l] == 0:
        if dr1-dr0>=0 and dr1-D0[l]<dy:
            return k1*(dr1-D0[l])+k2*D0[l]
        elif dr1-dr0>=0 and dr1-D0[l]>=dy:
            State[l],D0[l] = 1, dr1-dy
            return k1*dy+k2*(dr1-dy)
        elif dr1-dr0<0 and dr1-D0[l]>-dy:
            return k1*(dr1-D0[l])+k2*D0[l]
        else:
            State[l],D0[l] = -1, dr1+dy
            return -k1*dy+k2*(dr1+dy)
    elif State[l] == 1:
        if dr1-dr0<0 and dr1-D0[l]>=-dy:
            State[l] = 0
            return k1*(dr1-D0[l])+k2*D0[l]
        elif dr1-dr0<0 and dr1-D0[l]<-dy:
            State[l],D0[l] = -1, dr1+dy
            return k2*(dr1+dy)-k1*dy
        else:
            D0[l] = D0[l]+dr1-dr0
            return k1*dy+k2*(D0[l]+dr1-dr0)
    else:
        if dr1-dr0>0 and dr1-D0[l]<=dy:
            State[l] = 0
            return k1*(dr1-D0[l])+k2*D0[l]
        elif dr1-dr0>0 and dr1-D0[l]>dy:
            State[l],D0[l] = 1, dr1-dy
            return k2*(dr1-dy)+k1*dy
        else:
            D0[l] = D0[l]+dr1-dr0
            return -k1*dy+k2*(D0[l]+dr1-dr0)
```

```
57
58  #Operator Splitting Integration
59  def ops_ml(acc0,vel0,dis0,dr0,accg_1):
60      Sh1, Force1   = np.zeros(n), np.zeros(n)
61      dis1p         = dis0+vel0*dtt+1/4*acc0*(dtt**2)
62      P1, dr_p[0,i] = -M@np.ones(n)*accg_1, dis1p[0]
63      for j in range(1,n):
64          dr_p[j,i] = dis1p[j]-dis1p[j-1]
65      for l in range(n):
66          if l>0:
67              Sh1[l]= hystBL(dr0[l], dr_p[l,i],l)
68          else:
69              net_input  = norm(dr_p[l,0:i+1]).reshape((1,i+1,1))
70              Sh1[l]     = inv_norm(BLmodel.predict(net_input, verbose=0)[0,-1,0])
71      for l in range(n-1):
72          Force1[l] = Sh1[l] - Sh1[l+1]
73      Force1[n-1]   = Sh1[n-1]
74      F1   = -C@(vel0+1/2*acc0*dtt)-Force1+P1
75      acc1 = invL@F1
76      vel1 = vel0+1/2*(acc0+acc1)*dtt
77      dis1 = dis0+vel0*dtt+1/4*(acc0+acc1)*(dtt**2)
78      return acc1, vel1, dis1, Sh1
79
80  #Transformation of displacement
81  def norm(val):
82      val_norm = val/21.25915808188
83      return val_norm
84  #Inverse transformation of shear
85  def inv_norm(val_norm):
86      val = val_norm*1990.65038585148
87      return val
88
89  #Load ML module
90  BLmodel = load_model('5.ML models/MLM3.h5')
91
92  #Reading input wave
93  ndata, dt = 951, 0.02
94  Accg      = np.genfromtxt('3.Ground Motions/Taft 1952_EW.txt', skip_header=2, delimiter=',', max_rows=ndata)
95
96  #Input structure
97  n, h   = 16, 0.02
98  M      = np.diag([4500, 3000, 3000, 3000, 3000, 3000, 3000, 3000, 3000, 3000, 3000, 3000, 3000, 3000, 3000, 3000])/980
99  K1     = np.array([99, 644, 639, 628, 612, 590, 563, 531, 494, 451, 402, 349, 290, 225, 156, 80])*10
100 FY     = np.array([0, 20000, 20000, 20000, 20000, 20000, 20000, 20000, 20000, 20000, 20000, 20000, 20000, 20000, 20000, 20000])
101 K, K2  = np.diag(K1), np.array([0, 0.1, 0.1, 0.1, 0.1, 0.1, 0.1, 0.1, 0.1, 0.1, 0.1, 0.1, 0.1, 0.1, 0.1, 0.1])*K1
102 DY, D0 = FY/K1, np.zeros(n)
103 State  = np.zeros(n,int)
104 for i in range(0,n-1):
105     K[i,i]   = K[i,i]+ K[i+1,i+1]
106     K[i,i+1] = K[i+1,i] = -K[i+1,i+1]
107
```

```
#Eigenvalue problem
invM          = la.inv(M)
OMEGA2,phi_rev = la.eig(invM@K)
OMEGA = np.sort(np.sqrt(OMEGA2))
T     = 2*np.pi/OMEGA

#Construction of damping Matrix
C = (2*h/OMEGA[0])*K

#Numerical integration
tsub = 5
dtt  = dt/tsub
t    = np.arange(0,(ndata-1)*dt+dtt,dtt)
L    = M+1/2*C*dtt+1/4*K*(dtt**2)
invL = la.inv(L)
accg, accg[0]= np.zeros(len(t)), Accg[0]
for i in range(0,ndata-1):
    for j in range(0,tsub+1):
        accg[i*tsub+j]=Accg[i]+j*((Accg[i+1]-Accg[i])/tsub)
acc,acc[:,0] = np.zeros((n,len(t))), -accg[0]
vel, dis, dr = np.zeros((n,len(t))), np.zeros((n,len(t))), np.zeros((n,len(t)))
Sh, dr_p     = np.zeros((n,len(t))), np.zeros((n,len(t)))

for i in range(1,(ndata-1)*tsub+1):
    #Operator Splitting integration
    acc[:,i],vel[:,i],dis[:,i],Sh[:,i] = ops_ml(acc[:,i-1],vel[:,i-1],dis[:,i-1],dr[:,i-1],accg[i])
    dr[0,i] = dis[0,i]
    for j in range(1,n):
        dr[j,i] = dis[j,i]-dis[j-1,i]
```

APPENDIX C: TPB isolation layer hystereses-Experiment

C-1 TPB_Sin65

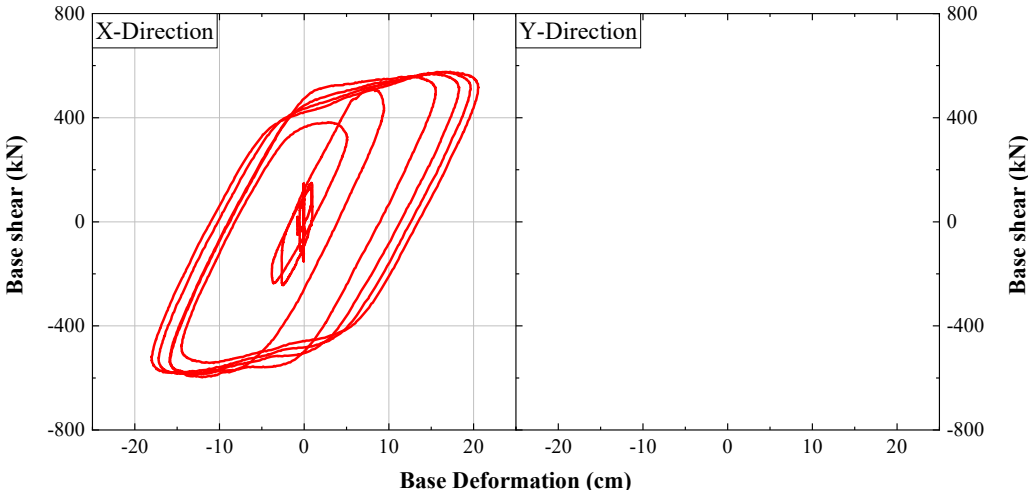

C-2 TPB_Sin100

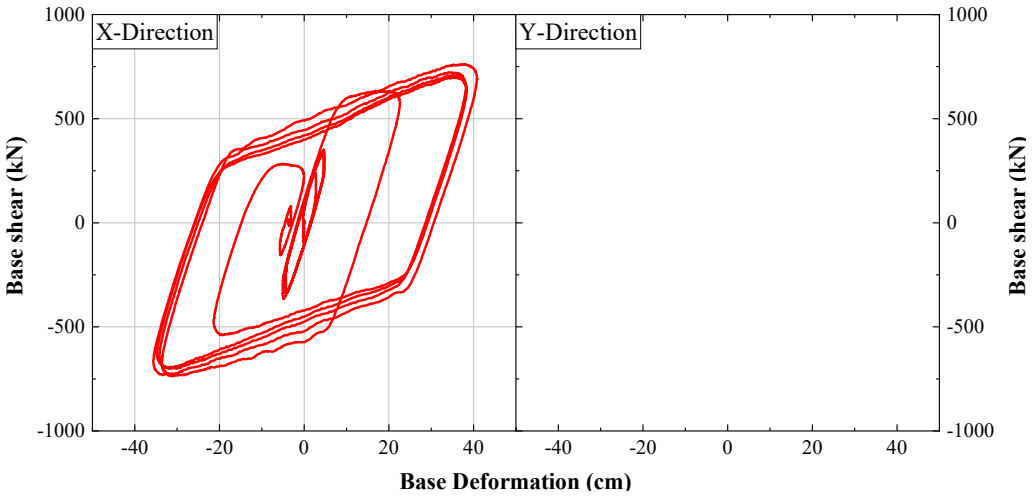

C-3 TPB_WSW80

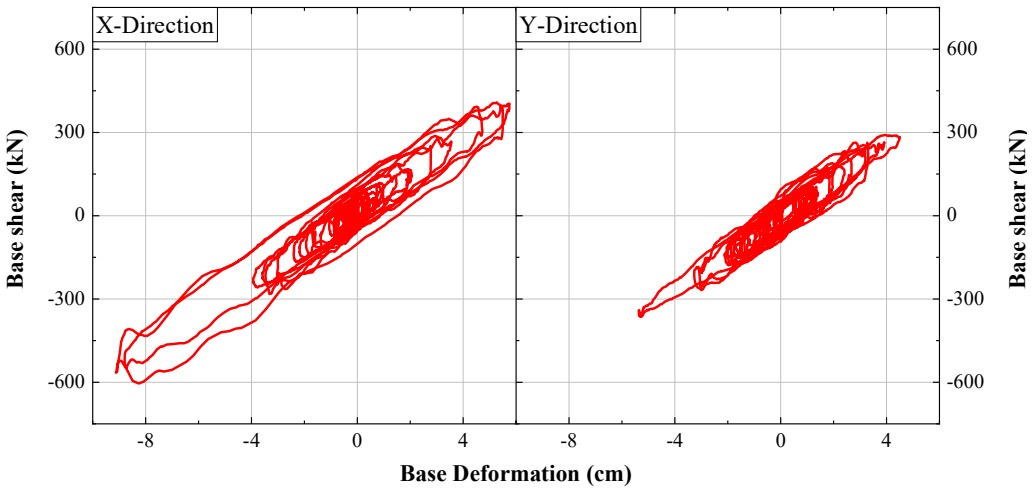

C-4 TPB_ELC130

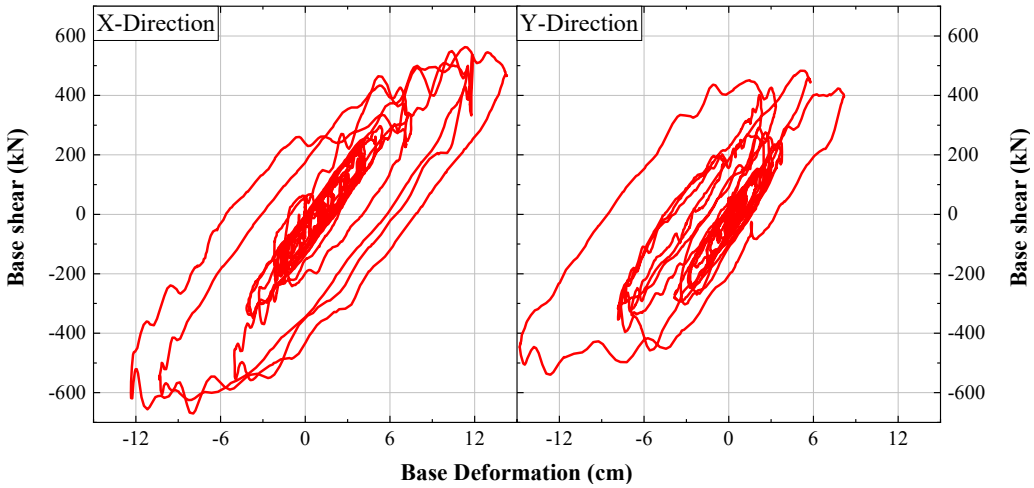

C-5 TPB_RRS-3D

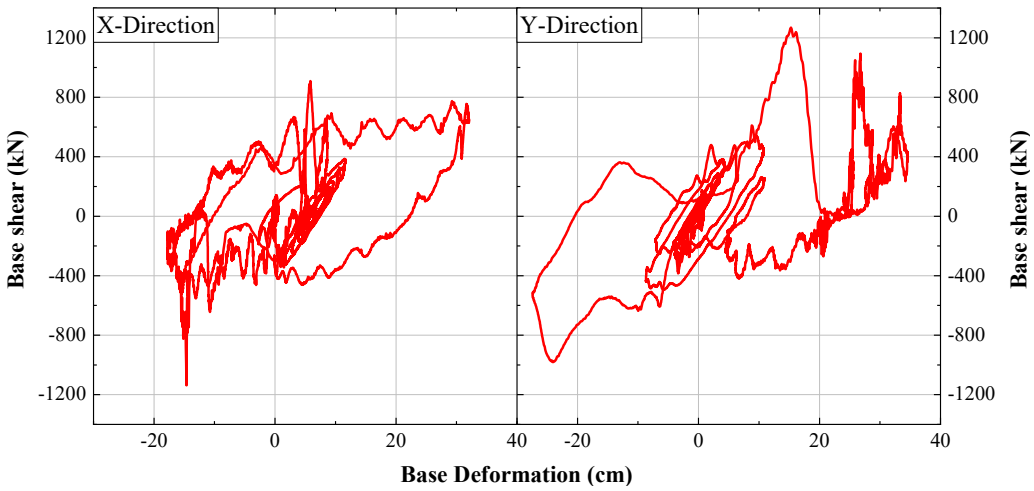

C-6 TPB_SYL100

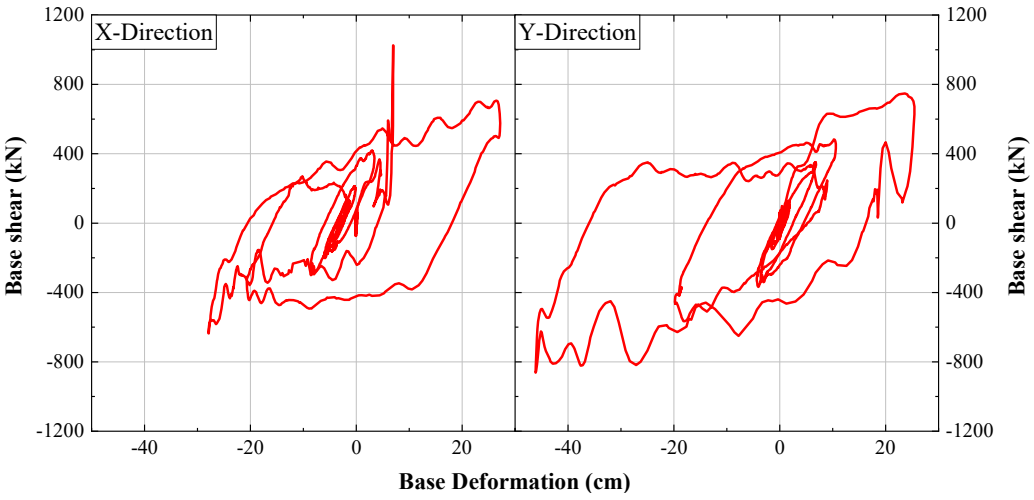

C-7 TPB_TAB50

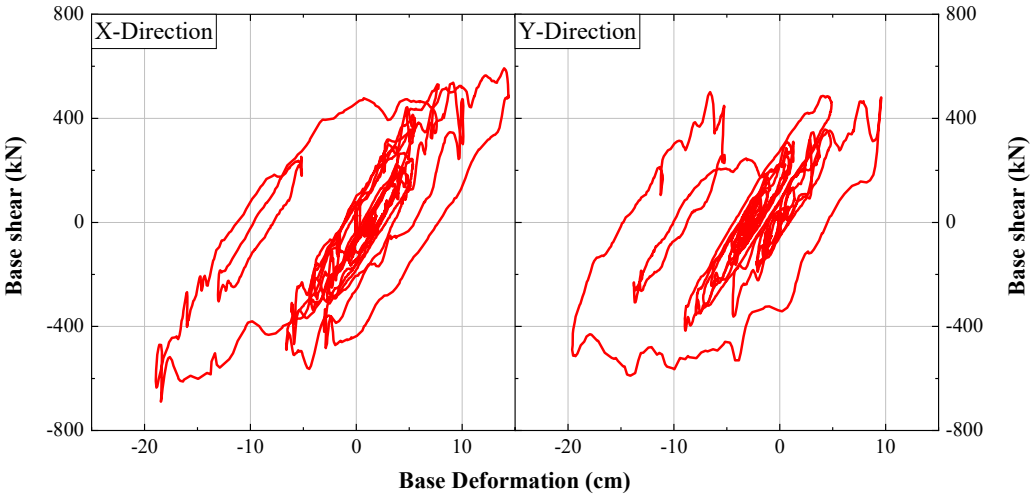

C-8 TPB_LGP70

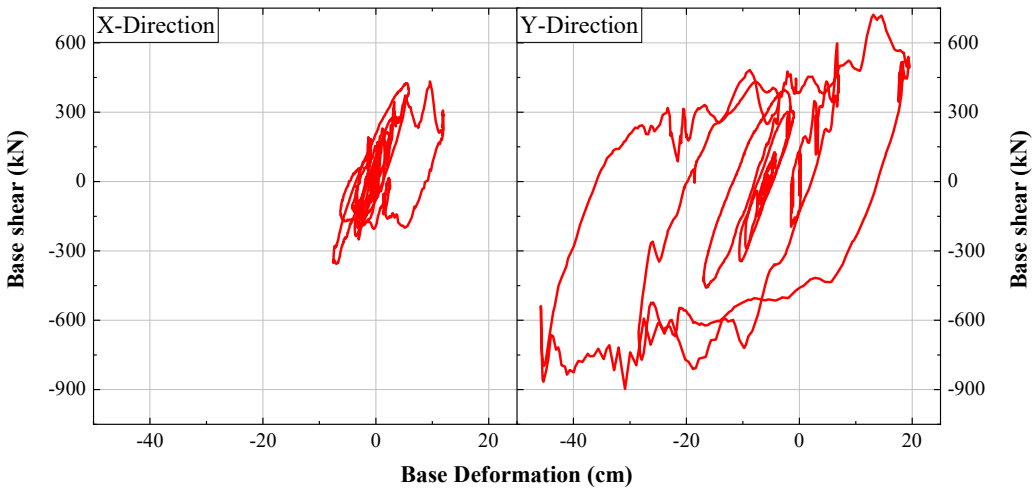

C-9 TPB_TCU50

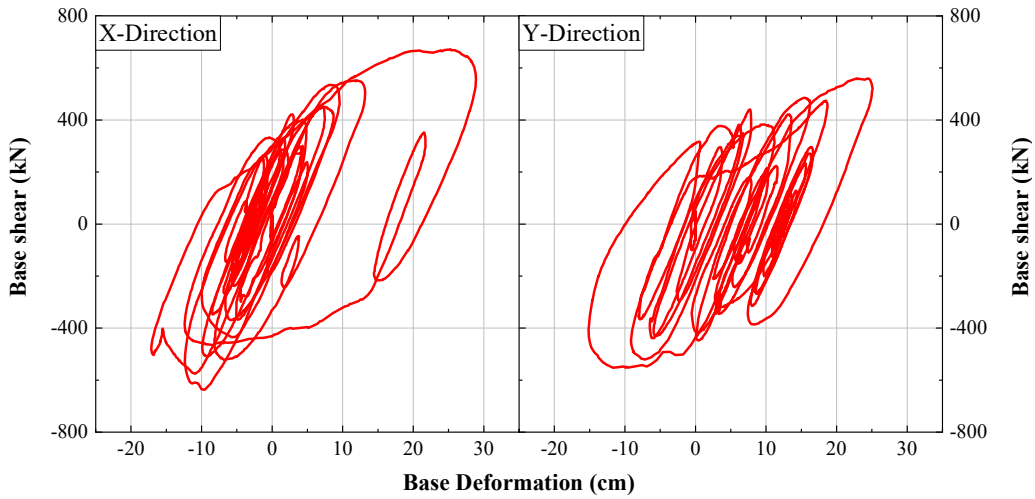

C-10 TPB_TCU70

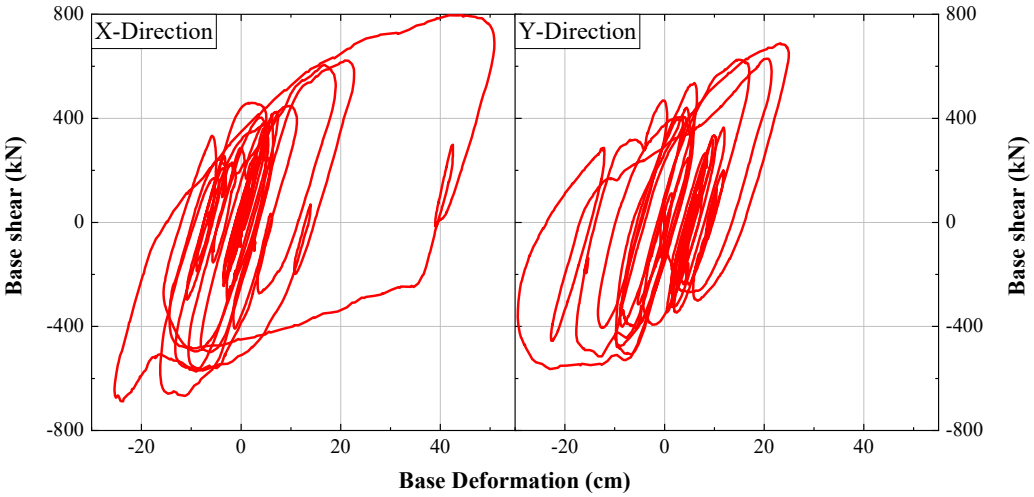

C-11 TPB_IWA100

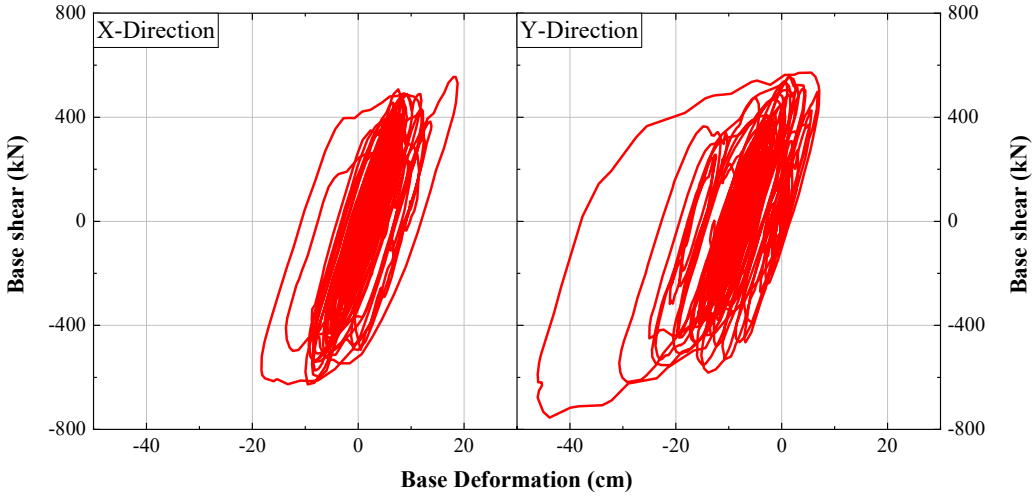

C-12 TPB_TAK100

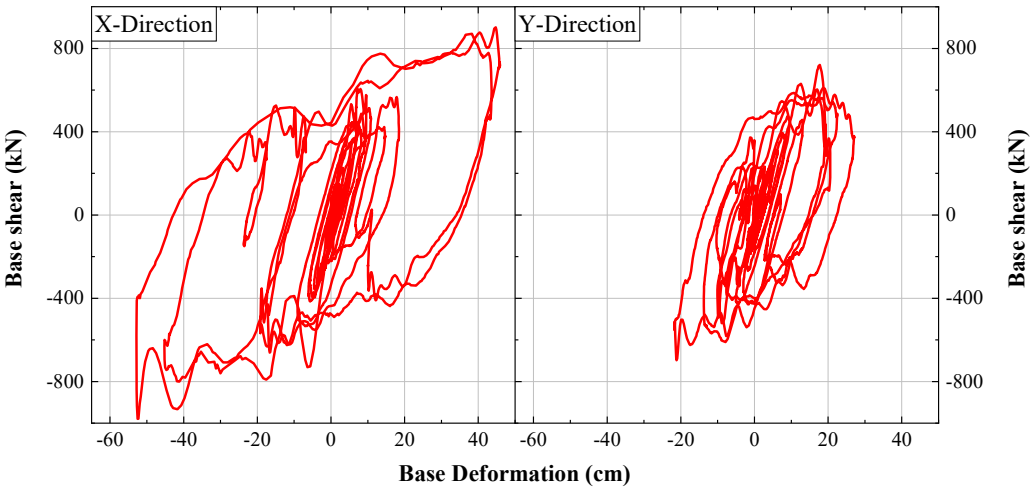

C-13 TPB_KJM100

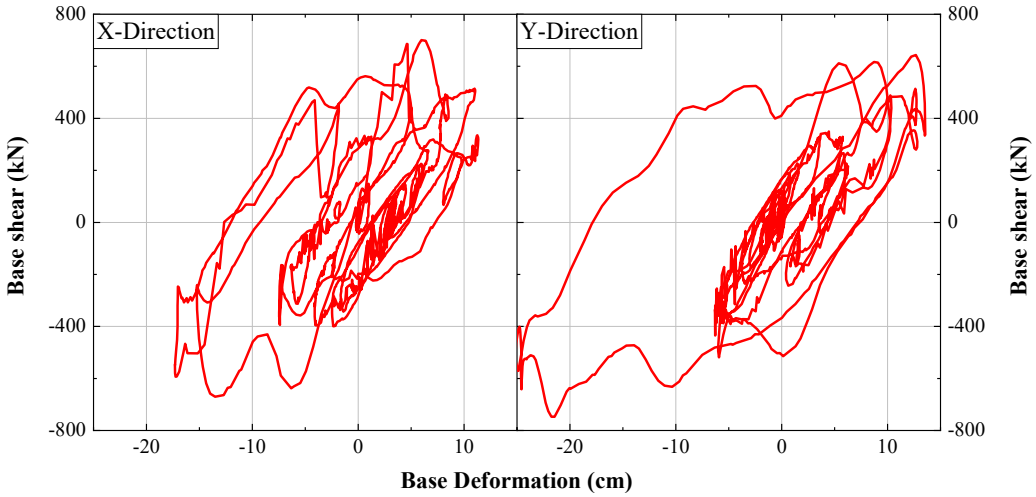

C-14 TPB_RRS-2D

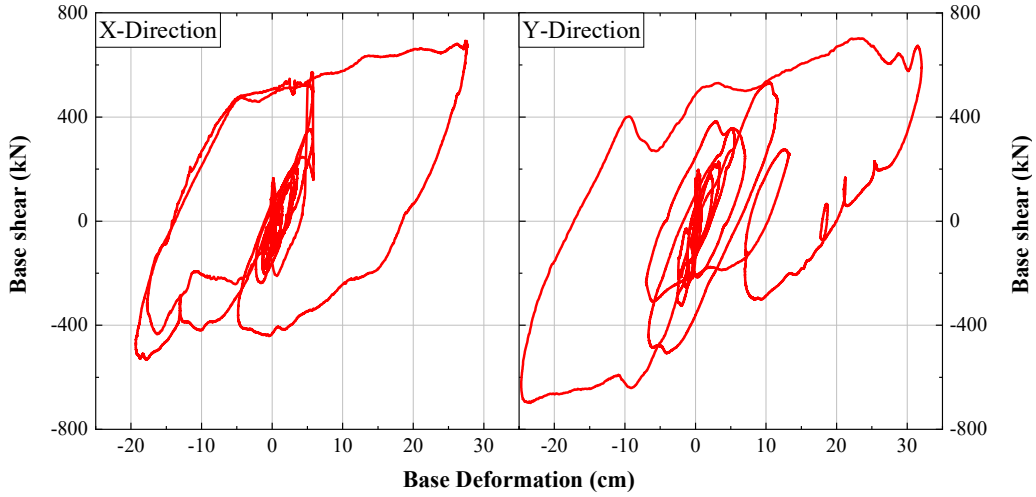

C-15 TPB_TCU80

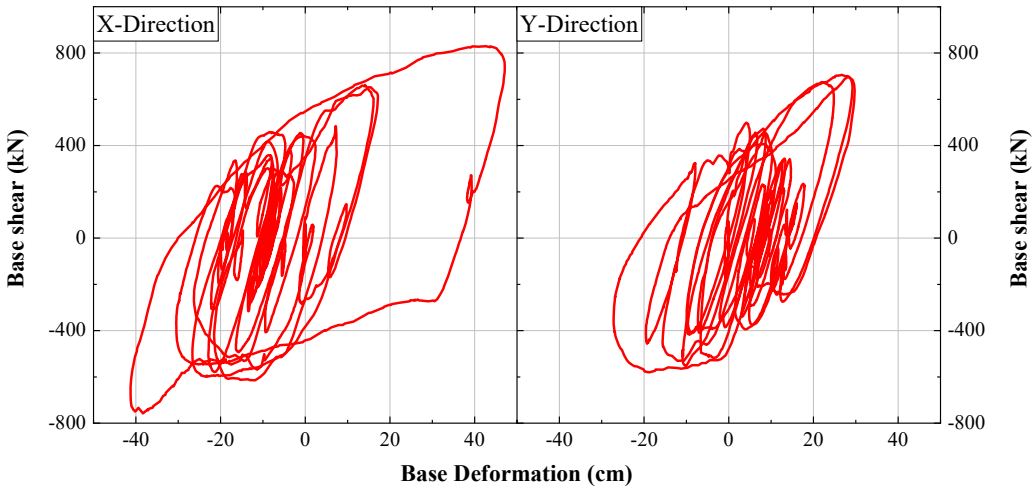

C-16 TPB_TAB80

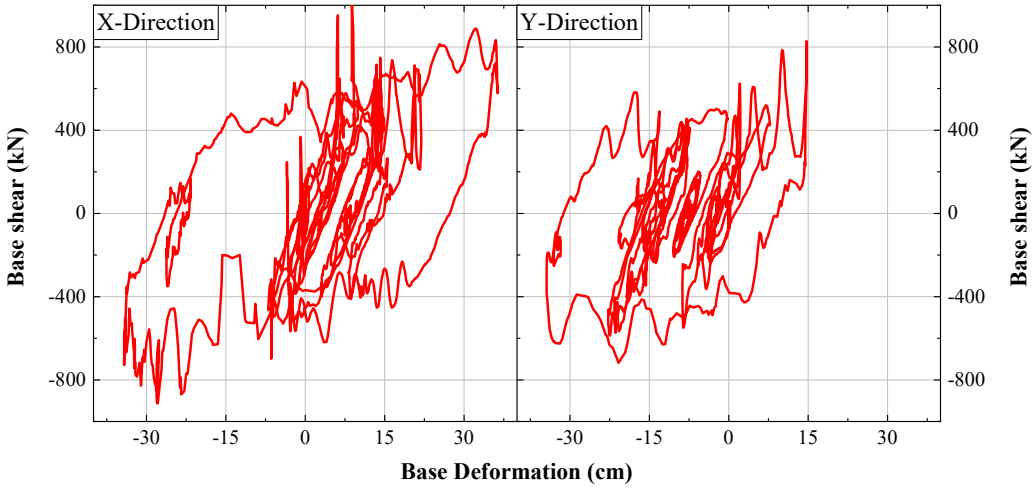

C-17 TPB_TAB90

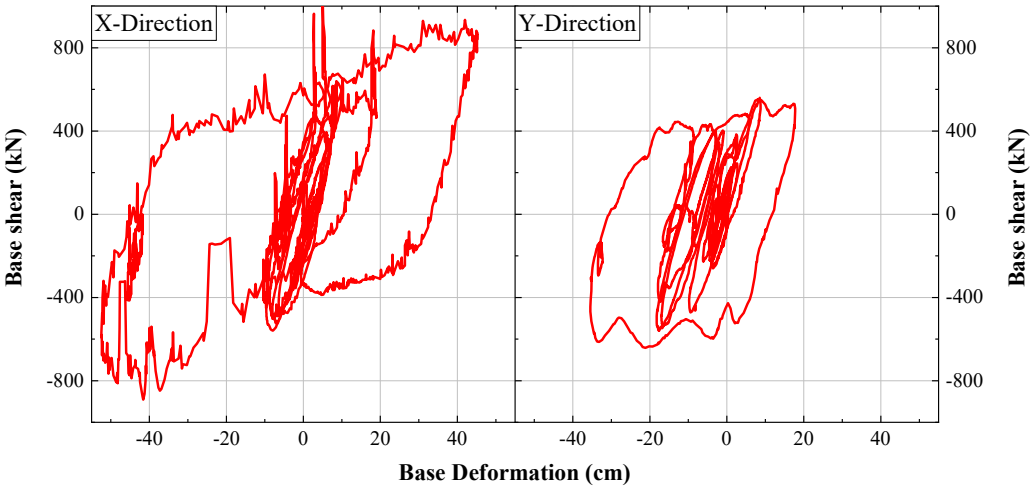

C-18 TPB_TAB100

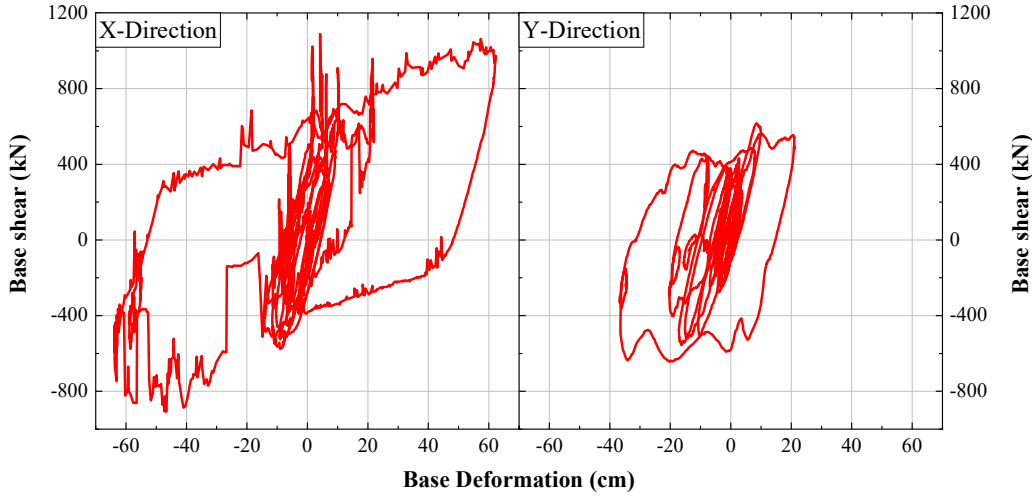

C-19 TPB_SCT100

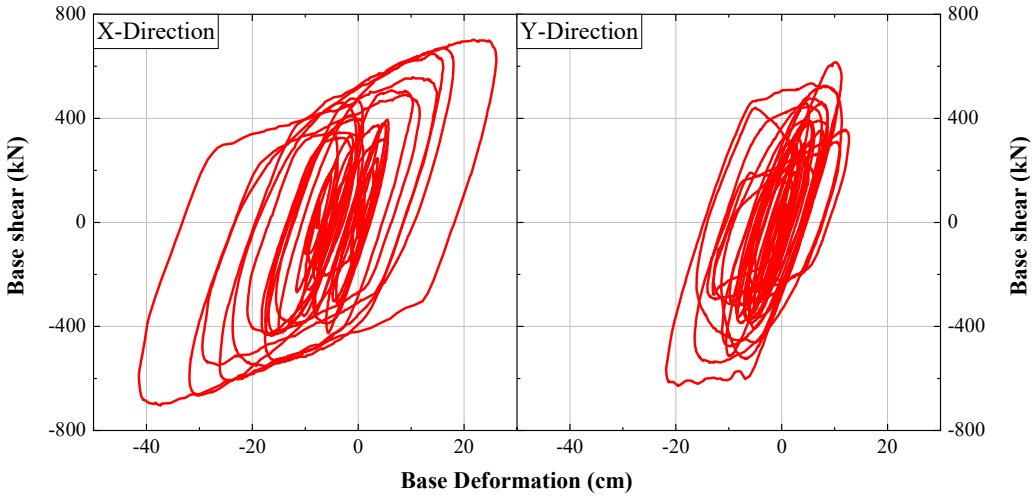

C-20 TPB_TAK115

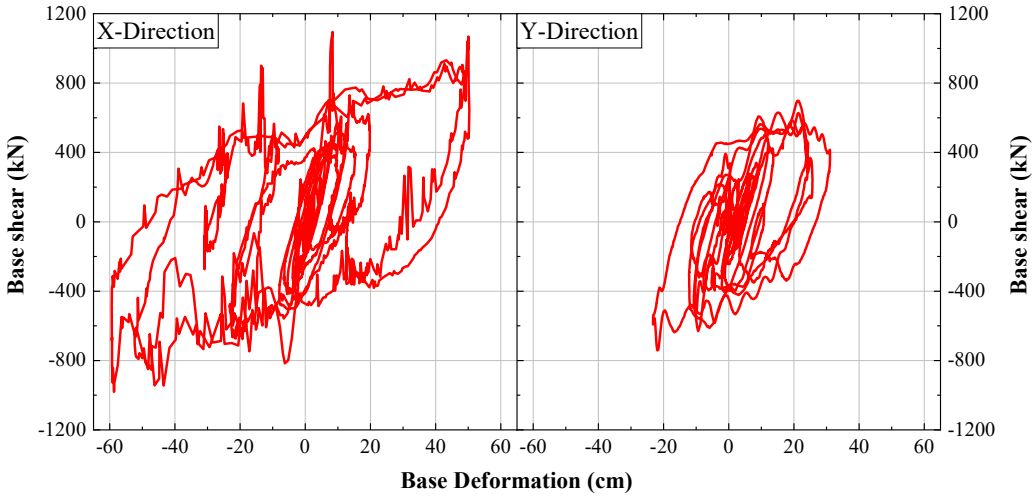

APPENDIX D: LRB Isolation layer hystereses-Experiment

D-1 LRB_Sin-1

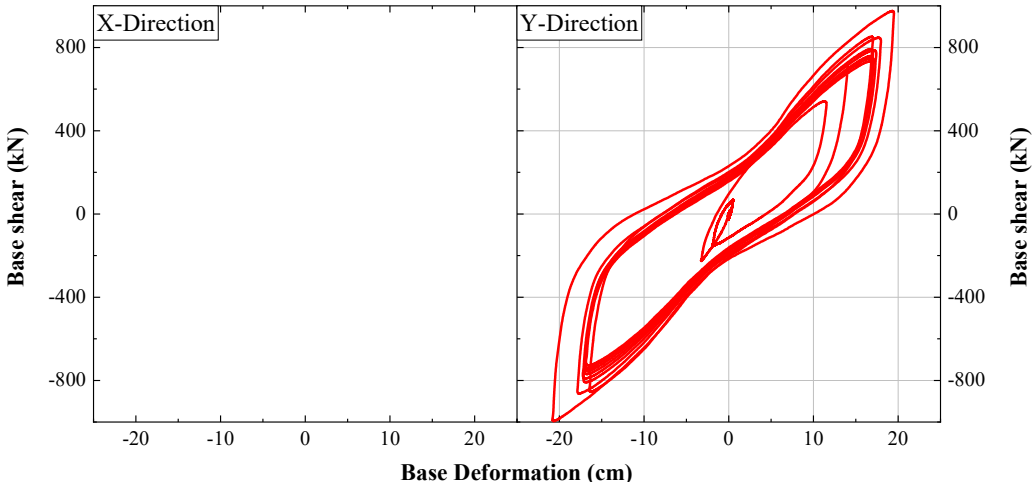

D-2 LRB_VOG75-1

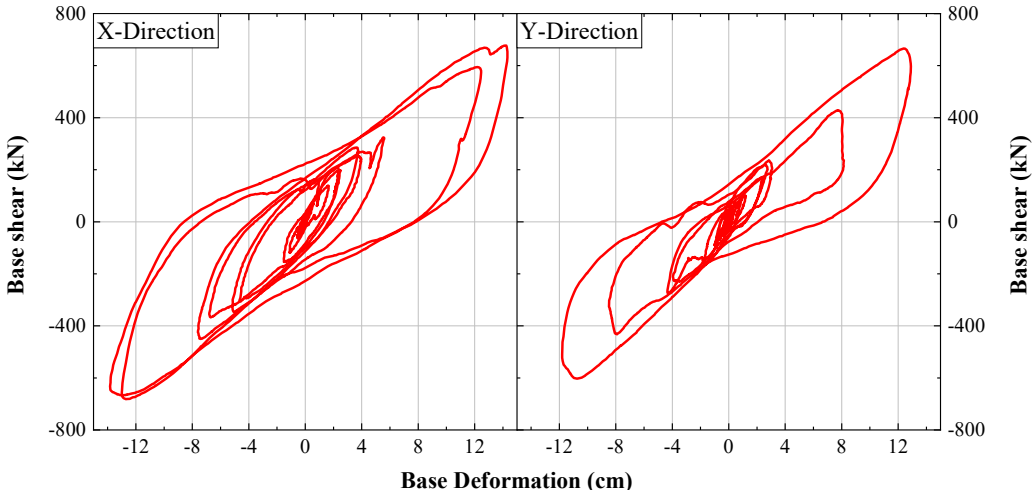

D-3 LRB_VOG100

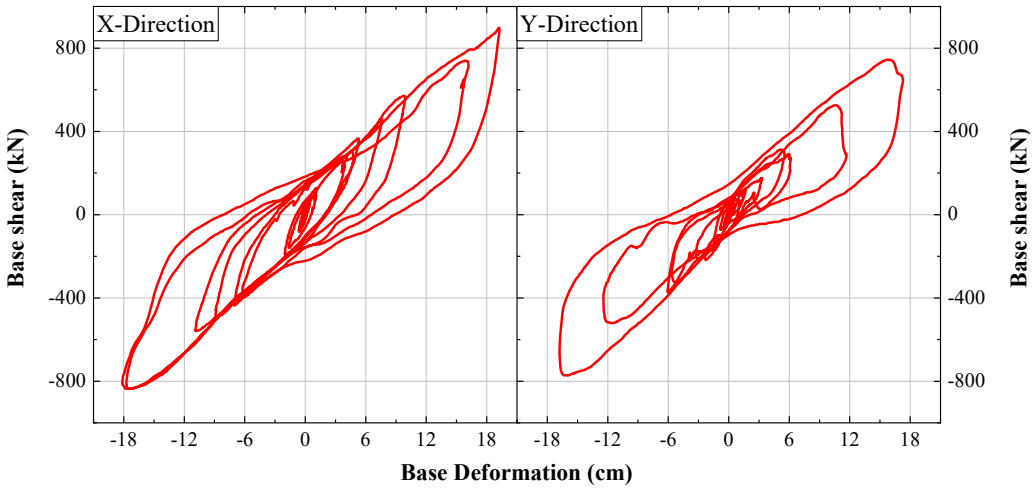

D-4 LRB_VOG125

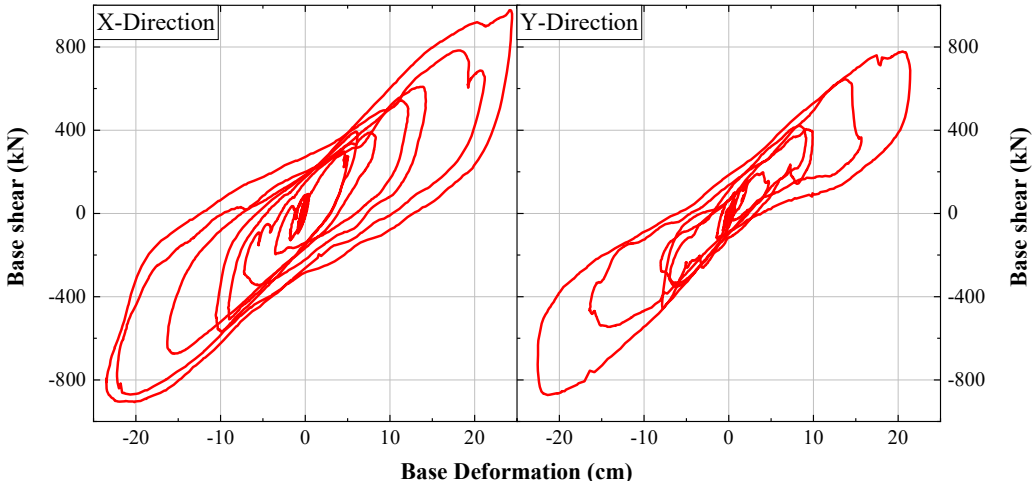

D-5 LRB_VOG150

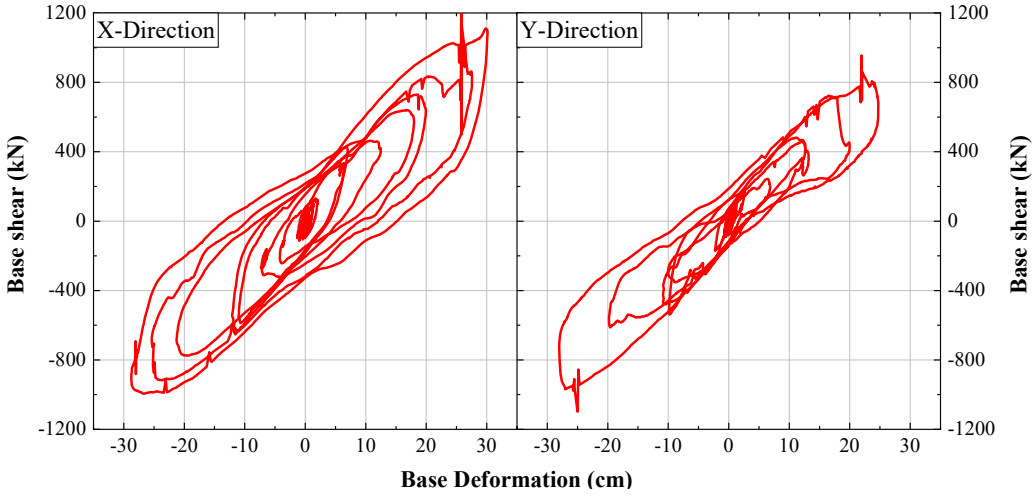

D-6 LRB_VOG175

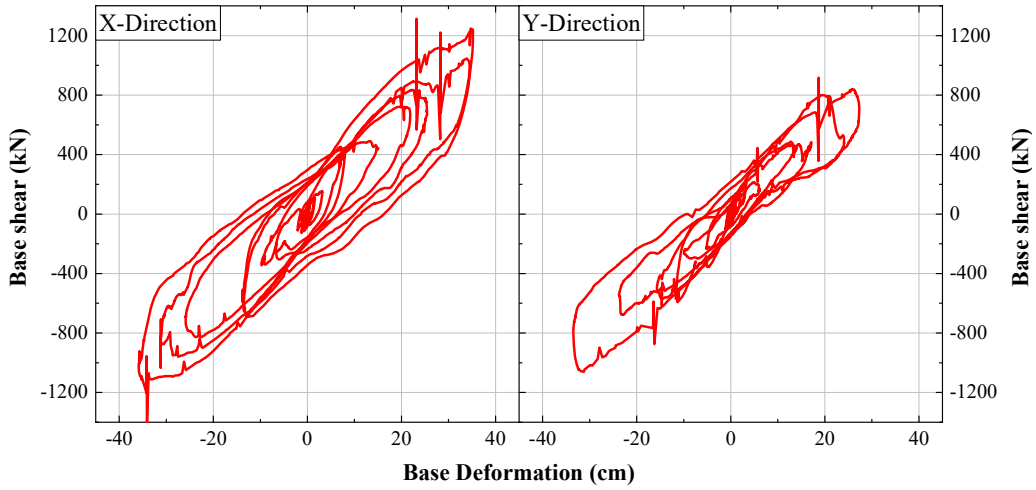

D-7 LRB_DIA80

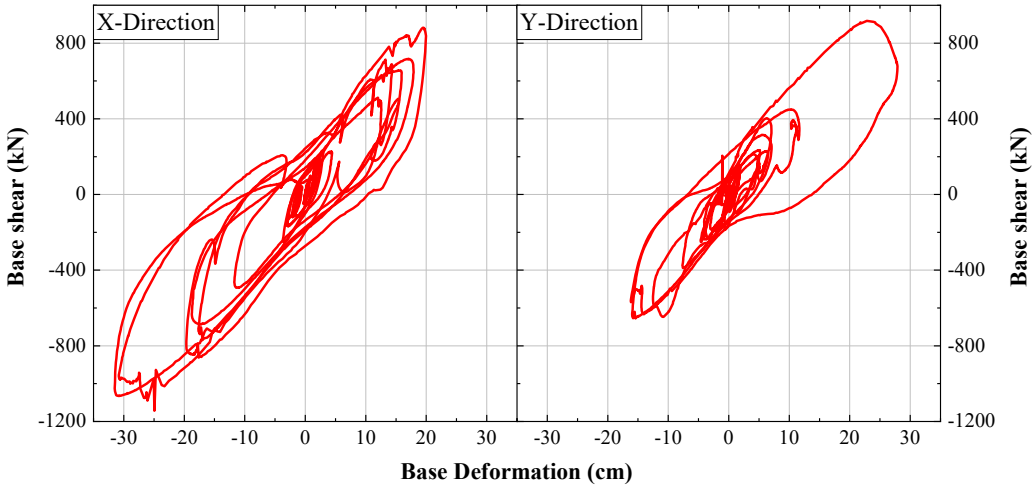

D-8 LRB_DIA95

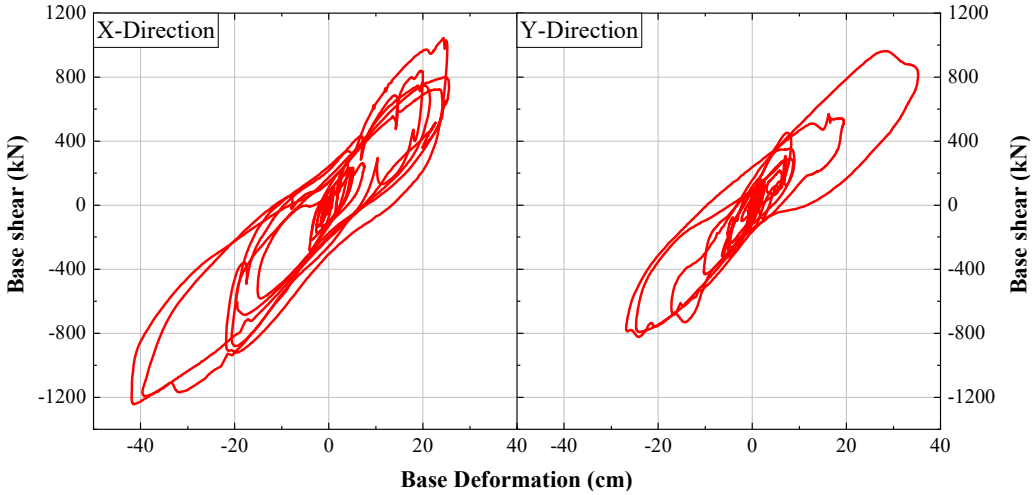

D-9 LRB_ELC130

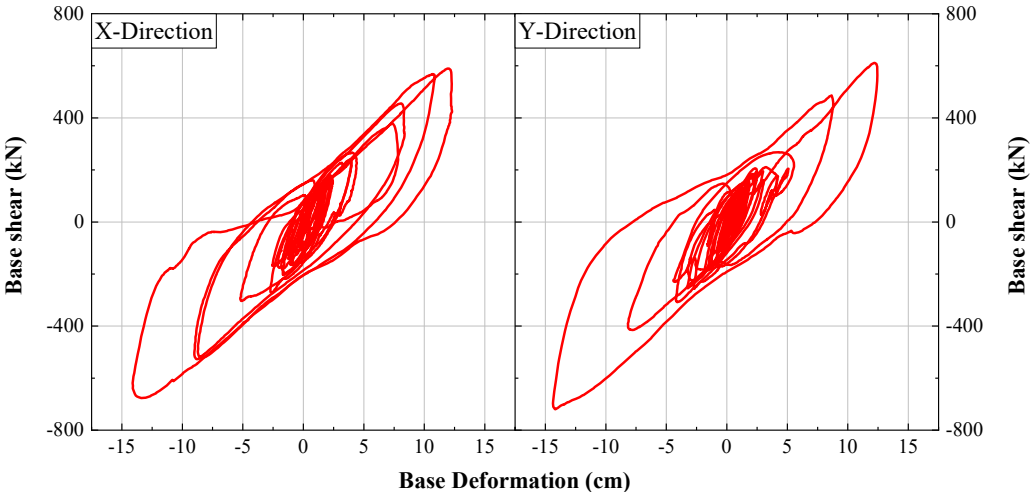

D-10 LRB_IWA100

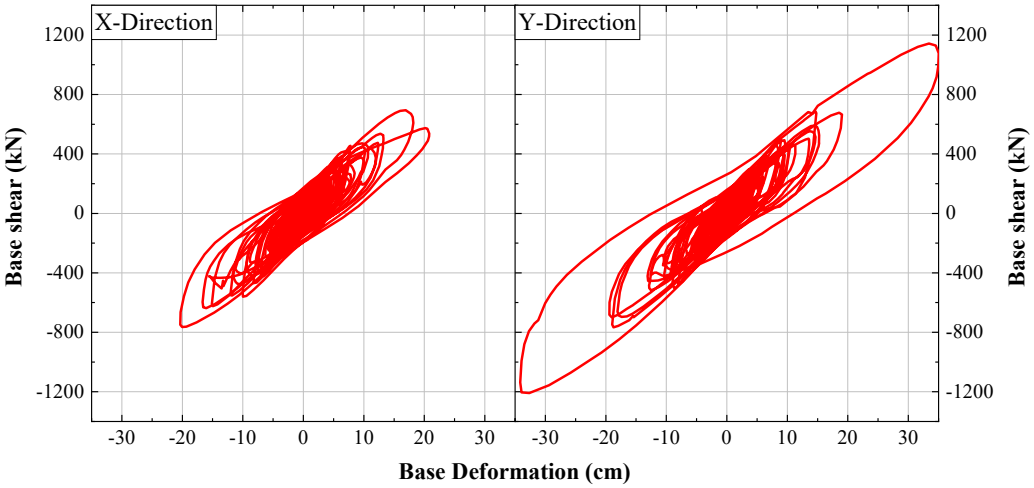

D-11 LRB_RRS-2D

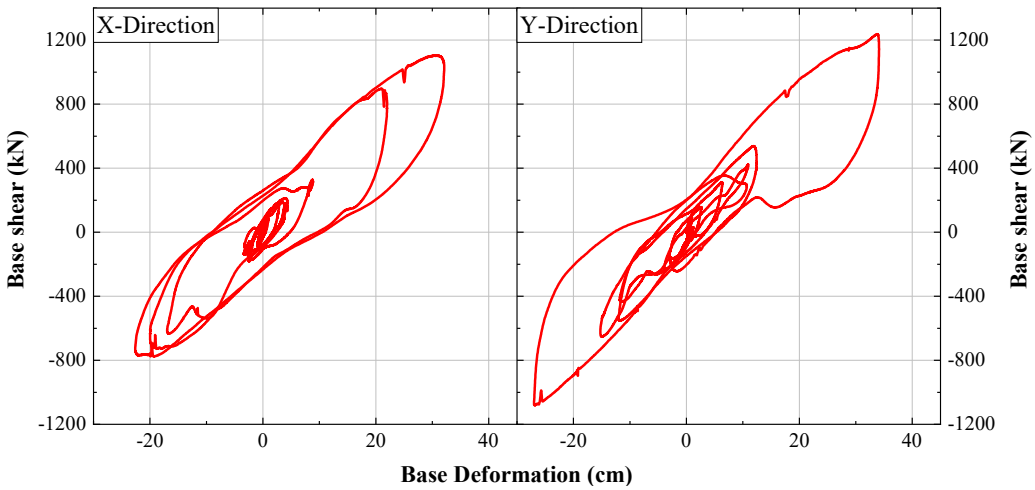

D-12 LRB_RRS-3D

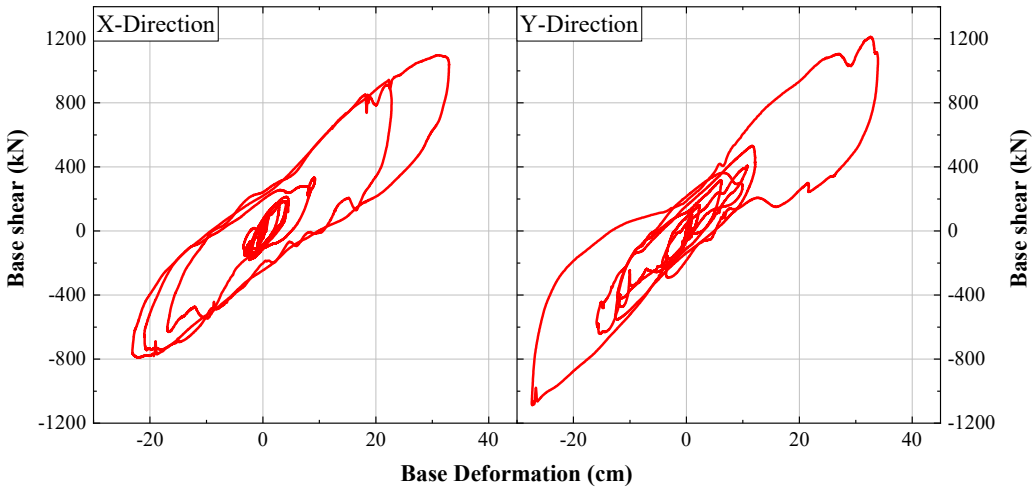

D-13 LRB_VOG75-2

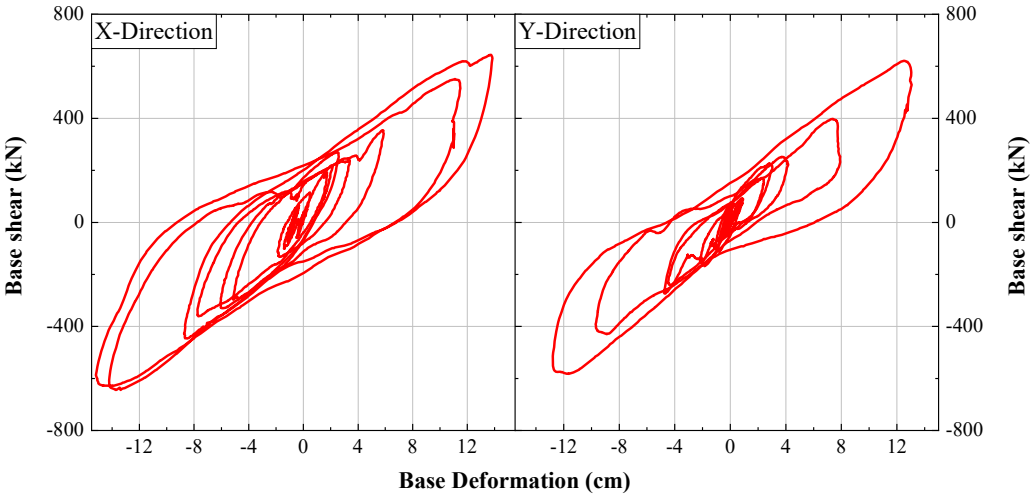

D-14 LRB_Sin-2